

NORTHWESTERN UNIVERSITY

**X-Ray Standing Wave Investigations of  
Group III and V Elements Adsorbed on the Si(001) Surface:  
Structure, Dynamics and Kinetics**

A DISSERTATION

SUBMITTED TO THE GRADUATE SCHOOL

IN PARTIAL FULFILLMENT OF THE REQUIREMENTS

for the degree of

DOCTOR OF PHILOSOPHY

Field of Materials Science and Engineering

By

Yonglin Qian

EVANSTON, ILLINOIS

December 1995

## **ABSTRACT**

### **X-Ray Standing Wave Investigations of Group III and V Elements Adsorbed on the Si(001) Surface: Structure, Dynamics and Kinetics**

Yonglin Qian

The surface structure and adsorption behavior of group III and V elements on the Si(001) surface are of great scientific and technological importance for their relevance to important issues such as III-V heteroepitaxy, surfactant-mediated epitaxy, delta-doping layers and surface passivation. Therefore, there is a great need to thoroughly characterize the structure in atomic scale for a better understanding of the adsorption behavior. The goal of this thesis is to establish a systematic method of characterizing the surface structure, dynamics, kinetics and adsorption behavior on crystalline semiconductor surfaces with the x-ray standing wave (XSW) technique.

In this thesis, a series of XSW measurements were carried out in an ultra-high vacuum environment on submonolayer Ga/Si(001), Sb/Si(001) and Bi/Si(001) surfaces prepared by molecular beam epitaxy. These XSW measurements precisely determine the ad-dimer locations, bond lengths and thermal vibrations for Ga, Sb and Bi adsorbates on Si(001). By combining these measurements with measurements made by other techniques and theoretical calculations, additional information about the ad-dimer orientation and geometry and substrate relaxations are obtained. These results provide

dependable information to confirm structural models predicted by theory and to solve certain controversies over the structure of these surfaces. The studies in this thesis also try to explore other capabilities of the XSW technique such as investigating surface stability, phase transition and surface kinetics.

---

Prof. M. J. Bedzyk

Department of Materials Science and Engineering

Northwestern University

Evanston, IL 60208

## ACKNOWLEDGMENTS

I would like to thank everyone who has been involved in this work and everyone who gave me support and encouragement. I want to share my joy and excitement with them.

First, let me express my deep gratitude to my thesis advisor Prof. Michael J. Bedzyk for introducing me into the wonderful world of x-ray standing waves. I am so fortunate to have his guidance, inspiration, patience and constant encouragement throughout the course of my thesis research.

I would also like to thank the people who were associated with NSLS beamline X15A. Dr. J. R. Patel, Dr. J. Zegenhagen and P. Freeland are owed my gratitudes for their efforts of designing the monochromator and UHV system. I am very grateful to Dr. Gregg E. Franklin and Dr. Paul F. Lyman, for things that they taught me about surface science and synchrotron radiation, and for fun and jokes that we shared.

My stay within the Materials Science Division at Argonne National Laboratory has always been enjoyable and memorable. I would like to thank the wonderful people in our group: Prof. Pedro A. Montano, Dr. Gordon S. Knapp, Dr. Mark A. Beno, Mark S. Engbretson, Dr. Guy Jennings, Dr. Mohan Ramanathan, Dr. Hyodoo You, Dr. Kazimierz Gofron, for their help and support.

Every member in our group at Northwestern University deserves my thanks. Among them I would like to give my special thank to Tienlin Lee for his help in many ways. Working with Tienlin has always been pleasant.

It has been a great pleasure for me to collaborate with Dr. Neil C. Sturchio and Dr. Ronald P. Chiarello of Argonne's Geoscience Group and Dr. Shaoping Tang and

Prof. A. J. Freeman of the Physics Department at Northwestern University. I consider that our fruitful collaborations benefited from their expertise and experience.

I also wish to thank Prof. D. Seidman, Prof. S. A. Barnett, Dr. Lonny E. Berman, Prof. J. Nogami, Dr. K. Huang and Dr. P. Lee for their help and encouragement.

This research is financially supported by the U. S. Department of Energy under contract No. W-31-109-ENG-38 to Argonne National Laboratory.

Finally, I would like to thank my family for their continuing encouragement and support. I am especially grateful to my wife Meijie for her understanding and patience, for the sacrifice that she made, and for the love and support that she gives me. I dedicate this thesis to her.

## TABLE OF CONTENTS

<b>ABSTRACT</b>	ii
<b>ACKNOWLEDGMENTS</b>	iv
<b>LIST OF FIGURES</b>	x
<b>LIST OF TABLES</b>	xv
<b>Chapter I Introduction</b>	1
1.1 Surface and adsorption on surfaces	1
1.2 Surface characterization	7
1.3 Silicon (001) clean and adsorbed surfaces	11
1.3.1 Silicon (001) clean surface	11
1.3.2 Adsorption on the silicon (001) surface	16
1.4 Proposed work	21
<b>Chapter II The X-Ray Standing Wave Technique</b>	24
2.1 Historical review	24
2.2 Dynamical theory of x-ray diffraction	27
2.3 The interaction of x-rays with solids	38
2.4 The photo-effect cross-sections: Dipole approximation	39
2.5 XSW structural analysis	42
2.6 XSW analysis of the dimerized surface	47
<b>Chapter III. Experimental</b>	53
3.1 Experimental Arrangement	53
3.1.1 The X-ray Sources	53
3.1.2 The X-ray Monochromator	55

3.1.3 UHV System	59
3.2 Measurement Control, Data Acquisition and reduction	64
<b>Chapter IV Sb/Si(001) Surface</b>	69
4.1 Sb adsorption on Si(001): Background information	69
4.2 Experimental	71
4.2.1 Sample preparation	71
4.2.2 XSW Measurements	73
4.3. Results and Discussion	76
4.3.1 Substrate Relaxation	76
4.3.2 Thermal vibrational amplitude and surface ordering	77
4.3.3 Dimer bond length and geometry	78
4.4 Summary	85
<b>Chapter V Bi/Si(001) Surface: (1x2) and (2x2) Phases</b>	86
5.1 (1x2) Bi/Si(001) Saturated Surface and Low Coverage (2x2)	
Bi/Si(001) Surface	86
5.2 Experimental	90
5.2.1 Surface preparation	90
5.2.2 XSW measurements	91
5.3 Results and Discussions	95
5.3.1 (1x2) phase saturated surface: structure and thermal vibration	95
5.3.2 The low coverage (2x2) phase	96
5.4 Summary	103
<b>Chapter VI The Ga/Si(001) Surface</b>	105
6.1 The Ga/Si(001) surface: Orthogonal or parallel ad-dimer?	105
6.2 Experimental	110

6.2.1	Surface Preparation	110
6.2.2	XSW measurements	111
6.3	Results and discussion	114
6.3.1	Dimer orientation	114
6.3.2	Ga growth mode and coverage dependency of the local structure	117
6.3.3	Thermal vibrational amplitudes	120
6.3.4	Dimer bond length	121
6.4	Summary	124
<b>Chapter VII Summary and Outlook</b>		125
7.1	Summary	125
7.1.1	Group V elements adsorption on Si(001)	125
7.1.2	Group III adsorption on Si(001)	126
7.1.3	Ad-atom Thermal vibrations on Si(001)	128
7.2	Future work	131
7.2.1	Adsorbate thermal vibrations	131
7.2.2	Surface kinetics: in situ study	132
7.2.3	Quadrupole effect	132
<b>Appendix A Experimental Procedure and Instrumentation</b>		134
A.1	Sample cleaning and mounting	134
A.1.1	Si Polishing	134
A.1.2	Si Etching	136
A.1.3	Mounting	136
A.1.4	Loading into the UHV system	137
A.2	Operation of the UHV system	139

A.2.1	General information	139
A.2.2	AES and LEED: Operation	142
A.2.3	Heating stage	147
A.3	Monochromator	151
A.3.1	Double-crystal monochromator at X15A	151
A.3.2	Instrumental Resolution	158
A.4	Procedure of XSW measurement	164
A.4.1	Monochromator setup	164
A.4.2	Sample alignment	165
A.4.3	XSW measurement	166
A.5	Coverage Calibration	166
A.5.1	By AES	166
A.5.2	By x-ray fluorescence yield	167
<b>Appendix B</b>	<b>XSW Data Analysis Software Package</b>	169
B.1	Raw data file	170
B.2	Data reduction: SUGO	171
B.2.1	Input of raw data	171
B.2.2	Data reduction	172
B.3	Data analysis: DARE	175
B.3.1	Data Manipulation	176
B.3.2	Rocking curve fit	179
B.3.3	Fluorescence fit	182
<b>References</b>		184

## LIST OF FIGURES

Figure 1.1	Three modes for thin film growth on surfaces.	6
Figure 1.2	Ball-and-stick models of the Si(001) surface.	13
Figure 1.3	A top view and a side view of the two-domain (2x1) Si(001) surface due to single atomic steps.	14
Figure 1.4	Various reconstructions on the Si(001) surface due to the dimer buckling.	17
Figure 1.5	Adsorption sites on the (2x1) Si(001) reconstructed surface and the (1x1) Si(001) unreconstructed surface.	18
Figure 2.1	X-ray standing waves generated within a perfect single crystal and above its surface by the Bragg diffraction.	25
Figure 2.2	A reciprocal vector diagram for Bragg diffraction (inside the crystal).	29
Figure 2.3	The Bragg case geometry for an asymmetrically cut crystal.	31
Figure 2.4	(a) The real and imaginary part and (b) the phase $\nu$ of the E-field ratio as a function of the relative Bragg angle. .	34
Figure 2.4	(c) A reflectivity curve (Darwin curve or rocking curve).	35
Figure 2.5	(a) The normalized effective absorption coefficient and (b) The penetration depth for the Si(004) reflection at 12 keV.	37

Figure 2.6	Examples illustrating the meaning of the geometrical factor $a_H$ and the coherent position $P_H$ .	46
Figure 2.7	A series of the hypothetical fluorescence yield curves for a surface adatom species with various coherent positions.	48
Figure 2.8	A side view of the group III and V metal/Si(001) surface ad-dimer model.	49
Figure 3.1	A schematic drawing of the experimental setup for UHV XSW measurements at NSLS X15A.	54
Figure 3.2	The photon flux from an NSLS bending magnet and from an APS A-undulator.	56
Figure 3.3	The simulated reflectivity and fluorescence yield curves convoluted with an ideal and a finite monochromator emittance.	60
Figure 3.4	A top view of the multi-chamber UHV system at NSLS X15A.	61
Figure 3.5	A flow chart illustrating the electronic control and data acquisition system for XSW measurements at NSLS X15A.	65
Figure 3.6	A fluorescence spectrum recorded by a Si(Li) detector from a 0.3 ML Ga/Si(001) surface.	67
Figure 4.1	The experimental and theoretical curves for the x-ray reflectivity and Sb L fluorescence yield for: (a) the Si (004) reflection and (b) the Si (022) reflection.	74

Figure 4.1	(c) The experimental and theoretical curves for the x-ray reflectivity and Sb L fluorescence yield for the Si (008) reflection.	75
Figure 4.2	A side view of the Sb/Si(001) surface ad-dimer models (symmetric and midpoint shifted).	81
Figure 4.3	The (044) experimental and theoretical curves for the x-ray reflectivity and Sb L fluorescence yield.	84
Figure 5.1	Top view and side view of the (2x2) (left side) and (1x2) (right side) Bi phases on the Si(001) surface.	88
Figure 5.2	The experimental and theoretical curves for the x-ray reflectivity and Bi L fluorescence yield for (a) the (004) reflection and (b) the (008) reflection.	93
Figure 5.3	A series of experimental and theoretical curves for the Si (004) reflectivity and normalized Bi L $\square$ fluorescence yield for RT (004) measurements after various annealing temperatures.	94
Figure 5.4	Measured XSW (004) coherent fraction and coherent position as a function of annealing temperatures.	99
Figure 5.5	The structural model for deriving phase compositions.	101
Figure 5.6	Derived phase compositions of Bi as a function of annealing temperatures.	102
Figure 6.1	Top view of the structural model (orthogonal ad-dimer) for (2x2), (2x3), (2x5) and (1x2) phases on the Ga/Si(001) surface.	107

Figure 6.2	A top view and a side view of the parallel and orthogonal ad-dimer models for the (2x2) Ga/Si(001) surface structure.	108
Figure 6.3	Experimental data and theoretical curves for the normalized Ga K $\alpha$ fluorescence yield and Si reflectivity for: (a) the Si(004) reflection and(b) the Si(008) reflection.	112
Figure 6.3	(c) Experimental data and theoretical curves for the normalized Ga K $\alpha$ fluorescence yield and Si reflectivity for the Si(022) reflection.	113
Figure 6.4	Experimental data and theoretical curves for the normalized Ga K $\alpha$ fluorescence yield and Si reflectivity for the Si(004) reflection.	116
Figure A.1	(a) The Si(001) sample and (b) The Mo sample holder used in X15A UHV system.	135
Figure A.2	The load-lock system for the UHV chamber at NSLS X15A.	138
Figure A.3	A schematic drawing of the front panel of the AES electronic control modules.	144
Figure A.4	A schematic drawing of the front panel of the LEED electronic control modules.	146
Figure A.5	The calibrated sample temperature vs. heating current curve for the heating stage in the deposition chamber.	148
Figure A.6	The calibrated curve of sample temperature vs. heating power for the heating stage in the x-ray chamber.	150

Figure A.7	Mechanical and electronic control system of the double-crystal monochromator at NSLS X15A.	152
Figure A.8	5 keV photons via the fundamental Si (004) reflection and 10 keV photons via the second-order harmonic (008) reflection can pass through the monochromator at the same time at synchrotron radiation.	154
Figure A.9	(a) A DuMond diagram illustrating the monochromator/sample arrangement for XSW measurement. (b) A DuMond diagram illustrating the angular width broadening due to the dispersion of the monochromator.	159
Figure A.10	A DuMond diagram illustrates the energy resolution of a monochromator followed by a slit at synchrotron radiation.	163

## LIST OF TABLES

Table 4.1.	Theoretical and experimental values of structural dimensions for the saturated (1x2) Sb/Si(001) surface.	80
Table 5.1	XSW measured parameters and estimated phase compositions for various annealing temperatures (T).	98
Table 6.1	A series of (004) XSW measurements on Ga/Si(001) with various Ga coverages.	115
Table 6.2	The (004) and (022) XSW measurements on the 1 ML Ga/Si(001) surface before and after the annealing.	119
Table 6.3	Theoretically calculated and experimentally measured structural parameters for the (2x2) Ga/Si(001) surface.	123
Table 7.1	The XSW measured and theoretically calculated dimer bond length and height as well as the covalent radius for group V elements adsorbed on Si(001).	127
Table 7.2	Measured and calculated thermal vibration amplitudes $\sqrt{\langle u_H^2 \rangle}$ at room temperature.	130
Table A.1	Part list for the multi-chamber UHV system. (Referring to Fig. 3.4)	140
Table A.2	Part list for the electronic and mechanical control of the XSW experimental setup. (Referring to Fig. 3.5 and Fig. A.7)	155

## **Chapter I Introduction**

### *1.1 Surface and adsorption on surfaces*

Surface science investigates the chemical composition, structure, dynamics and kinetics of surfaces and their relationship to surface chemical, electronic and mechanical properties. The growth in surface science and in the number of surface science techniques available has dramatically increased since the early 1960's. Although surface-related phenomena such as adsorption, catalysis and thin film growth have been investigated long before 1960, it was then that the achievements in vacuum technology provided the feasibility to obtain ultra-high vacuum (UHV) reliably and, thus, to conduct experiments with what are commonly called clean surfaces. Understanding surface structure and properties not only is of academic interest, but also and more importantly, can have major impact on specific applications in the "real world". Modern technology evolves towards the use of large surface-to-volume ratio devices (catalysts, integrated circuits, etc.). For example, understanding catalysis, corrosion of materials and certain kinds of mechanical failure due grain boundaries has been the motivation for modern surface science. It requires a thorough information about the surface composition and atomic structure to understand the passivation of the surfaces against corrosion or the elimination of surface sites where cracks are initiated.

More recently and more importantly, the rapid development in the semiconductor industry over the past two decades has been a constant driving force for modern

surface science. For example, the formation of metal - semiconductor junctions with desirable properties is strongly influenced by the tendency for chemical interactions to occur between the metals and the semiconductor and, therefore, demands a fundamental knowledge of metal adsorption on semiconductor surface. With the further shrinking of semiconductor device sizes far below the micron scale, one starts to deal with a significant fraction of atoms on surfaces or interfaces. These atoms can have electronic properties markedly different from those of the bulk, which can have dramatic effects on device performance. Furthermore, with the need of growing thicker, higher quality heteroepitaxial thin films in a precisely controlled way in order to explore exotic electronic properties of novel materials, a thorough understanding of heteroepitaxy, surface kinetics, growth mode and stoichiometry is highly demanded.

Fundamentally, surfaces are of great interest because they represent a special kind of planar defect in the solid state. Much of our understanding of solids is based on the fact that they are perfectly periodic in three dimensions; the electronic and mechanic properties can be described in great details using methods which rely on this periodicity. The introduction of a surface breaks this periodicity in one direction and can lead to structural changes as well as the introduction of localized electronic and vibrational states. For an ideal, semi-infinite crystal, the outermost layer of atoms would be the surface. However, the truncation of a bulk crystal leaves the outermost atoms exposed to vacuum and chemically/electronically unsaturated. The top several layers of atoms may undergo some relaxations/reconstructions to achieve the lowest total energy. Therefore, the structure of a clean surface is in general different from that due to a simple truncation of the bulk.

One of the requirements fundamental to surface studies is that one must be able to prepare a surface with well-defined structure and composition reproducibly. In

particular, one must be able to produce and maintain a clean surface for a sufficiently long time for experimental investigations. This is why most surface science studies have to be performed under vacuum. How good a vacuum is required? One can analyze this problem by describing the molecules impinging flux  $r$  to the surface from the environment by the expression:

$$r = p (2\pi mkT)^{-1/2}. \quad (1.1)$$

Here  $p$  is the pressure,  $m$  is the mass of the molecule,  $k$  is the Boltzmann constant, and  $T$  is the temperature. A typical solid surface has about  $10^{15}$  atoms /  $\text{cm}^2$ . Therefore, if one starts with an initially clean surface at  $10^{-6}$  torr nitrogen, the surface will be covered by a monolayer of gas molecules from the ambient in a few second, assuming that the sticking probability is equal to unity. Therefore, the "clean" time at  $10^{-6}$  torr is on the order of seconds. The "clean" time is about one hour at  $10^{-9}$  torr and ten hours at  $10^{-10}$  torr. The environment with a pressure at  $10^{-9}$  torr or better is normally defined as ultra-high vacuum (UHV). Most modern UHV surface research studies are performed at pressures between  $10^{-10}$  and  $10^{-11}$  torr to ensure that surfaces are not contaminated during experiments due to adsorption from the ambient. An UHV environment is generally achieved by having a stainless steel vacuum chamber pumped by turbomolecular pump, ion pump, cryopump or diffusion pump.

To obtain a clean surface in UHV, there are generally three methods which are commonly used: cleavage, sputtering and annealing. The cleavage method only works for brittle materials that have definite cleavage planes. Only surfaces along certain orientations are available through this method. The sputtering method utilizes the inert gas ions (usually  $\text{Ar}^+$ ) to sputter the surface to remove contaminated layers. However,

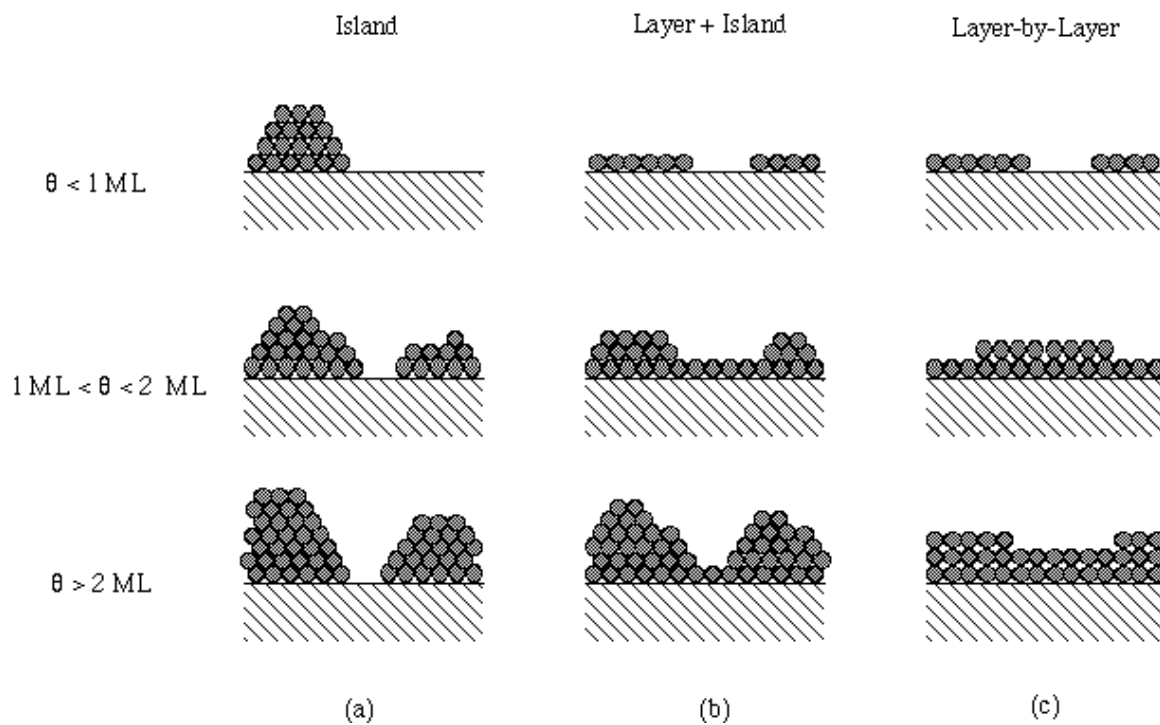
the side-effect of the ion sputtering is the disordering of the surface. The annealing method is the most general and effective method to clean the surface, especially for semiconductors. For example, annealing at 1200°C is conventionally used to evaporate the thin SiO<sub>2</sub> layer and to remove possible carbon contamination. Recently, by combining the annealing with the chemical pretreatment in which the clean thin oxide layer free from carbon contaminations, the temperature required to clean the Si surface has been reduced down to 800°C [59].

Once a clean surface is obtained, the deposition of an adsorbate can be conducted to form the desired surface phase. Most solid materials are deposited by a thermal evaporation method called molecular beam epitaxy (MBE) evaporation [56, 64]. The evaporated material is held within the crucible of an effusion cell which is heated by radiation from a resistance-heated source (*e.g.* tungsten wires). By adjusting the temperature of the effusion cell, the exposure time and the substrate temperature, one can control the evaporation flux, growth rate and mode to prepare desired surfaces. The surface density or coverage ( $\theta$ ) of the adsorbate is characterized by the coverage unit, monolayers (ML). One monolayer (ML) is defined as the adsorbate atoms areal density equivalent to that of the corresponding unreconstructed substrate surface layers. For example, one monolayer is equal to  $7.8 \times 10^{14}$  atoms/cm<sup>2</sup> for Si(111) and  $6.78 \times 10^{14}$  atoms/cm<sup>2</sup> for Si(001).

It is generally accepted that there are three possible modes of thin film growth on surface [125], which are illustrated schematically in Fig. 1.1. The first mode is called the island or Volmer-Weber (VW) mode (Fig. 1.1(a)), where small clusters are nucleated directly on the substrate surface and then grow into islands of the condensed phases. This happens when the adsorbate atoms are more strongly bound to each other than to the substrate. This mode occurs in many systems of metals growing on insulators. The

second growth mode is the layer-by-layer or Frank-van der Merwe (FM) mode (Fig. 1.1(c)). Because the adatoms are more strongly bound to the substrate than to each other, the first atoms to condense form a complete monolayer on the surface, which becomes covered by a second layer with a slightly weaker bond. Providing the decrease in binding is monotonic, toward the value for a bulk crystal of the adsorbate, the layer growth mode is obtained. This (FM) growth mode is observed in some metal - metal and semiconductor - semiconductor systems. The third growth mode is an intermediate case, called the layer plus island or Stranski-Krastanov mode (Fig. 1.1(b)). After forming the first monolayer or a few monolayers, subsequent layer growth is unfavorable and islands are formed on top of this "intermediate layer". This mode is observed in many metal - metal and metal - semiconductor systems.

Figure 1.1 Three modes for thin film growth on surfaces: (a) island or Volmer-Weber (VW) mode; (b) layer plus island or Stranski-Krastanov mode; (c) layer-by-layer or Frank-van der Merwe (FM) mode.



## *1.2 Surface characterization*

In general, to characterize a particular surface, one is interested in its atomic and electronic structure, its chemical composition, surface morphology, as well as its physical and chemical characteristics. To obtain this information a large variety of surface analysis techniques are used. In most cases, these techniques employ electron, photon or ion beams to probe the surface under investigation. Each one of the methods is specifically sensitive to one (or several) features of the surface. Therefore, the combination of several complementary methods is usually required for obtaining conclusive information about the structure and properties of the surface. The experimental methods of surface analysis are given a great attention in the literature (*e.g.* [132]). Here, only a brief summary of the main aspects of the commonly used surface analysis techniques is presented.

### *(1) Low-energy electron diffraction*

Low-energy electron diffraction (LEED) is a routine method for surface analysis [124]. It employs an electron beam with an energy of 20 - 300 eV which provides surface sensitivity. LEED is well suited to characterize the surface ordered structure by providing the symmetry and periodicity of the two-dimensional unit cell. However, the surface structure has to have long-range order and a large domain size. By comparing the LEED I-V (reflection intensity versus electron energy) curves with that calculated for a given model, some structural information is also possible to be obtained by LEED.

However, due to strong multiple scattering effects serious difficulties are found in the dynamical diffraction theory calculations.

*(2) Reflection high-energy electron diffraction*

Reflection high-energy electron diffraction (RHEED) [132] method employs an electron beam with an energy of 30 - 100 keV. The feature of glancing incidence makes RHEED sensitive to surface rather than to bulk structure. The usual geometry of RHEED makes it possible to observe the RHEED pattern during the growth processes. In the first approximation, the results of RHEED experiments can be considered by utilizing kinematical diffraction theory. However, the more accurate consideration of the surface atomic geometry requires the complicated dynamical diffraction theory.

*(3) UHV transmission electron diffraction*

In UHV transmission electron diffraction (TED) [112, 61, 81], these difficulties associated with LEED and RHEED can be avoided since the single-scattering approximation of diffraction can be more safely assumed in TED. TED can be successfully applied to the analysis of the surface in-plane atom positions. However, this technique has not been widely used. Also the sample preparation for TED makes it very difficult to get undamaged surfaces for investigation.

*(4) Auger electron spectroscopy*

Auger electron spectroscopy (AES) is one of the most used techniques for the analysis of surface chemical composition [132]. It provides the possibility to detect all elements (except H and He) of the periodic table present in the first few atomic layers. Thus, AES is widely used for quantitative estimation of adsorbate coverages.

#### *(5) Photoelectron and photoemission spectroscopy*

Photoelectron and photoemission spectroscopy have proven to be powerful techniques for the determination of the electron properties and surface structures [132]. Depending on the photon energy, one can distinguish between ultra-violet photoelectron spectroscopy (UPS) and x-ray photoelectron spectroscopy (XPS). UPS is used to study the occupied valence electron, state and XPS is used to study core states.

#### *(6) Ion scattering and channeling*

Impact-collision ion scattering spectroscopy (ICISS) [40] provides detailed structural information in real space rather than in reciprocal space as for diffraction or photoemission and does not require long-range order. However, it is strongly model dependent.

Another ion technique is MeV transmission ion channeling technique [48]. It uses transmission ion channeling to determine surface adsorbate sites with a precision of  $\pm 0.1 \text{ \AA}$ . It is model-dependent.

#### *(7) Scanning tunneling microscopy*

Scanning tunneling microscopy (STM) has a very short history of only 13 years but already has become a major technique for surface analysis [19, 122]. It provides high-resolution real-space images of the surface electronic and atomic structure. The intuitive information obtained by STM often serves as very useful initial stage for modeling very complicated surface structures. The large dynamic range of STM makes it a powerful tool to study different features of surfaces from atomic structure to surface kinetics. STM has certain limitations such as chemical insensitivity, tip-sample interaction, etc.

*(8) Surface extended x-ray absorption fine structure spectroscopy*

Surface extended x-ray absorption fine structure spectroscopy (SEXAFS) [35], which is employed at tunable synchrotron x-ray beamlines, has become a key tool for the determination of the local (nearest-neighbor) structure of the surface. SEXAFS does not need long-range order and has high accuracy ( $\pm 0.03 \text{ \AA}$ ) for nearest neighbor bond lengths determination.

*(9) Surface x-ray diffraction*

The availability of synchrotron radiation facilities makes it possible to use x-ray diffraction (XRD) to investigate surface structures [104]. When the x-ray is incident to the surface at glancing angles, thereby limiting the penetration of x-rays into the bulk, the surface sensitivity is considerably enhanced. XRD has the ability to solve the surface structure with high precision. However, it requires long-range order of the surface structure.

### *(10) X-ray standing wave*

The x-ray standing wave (XSW) [136] technique combines the advantages of x-ray diffraction, scattering, interferometry and spectroscopy. It determines the adsorbates' adsorption sites with very high precision (ultimately  $\pm 0.01 \text{ \AA}$ ) relative to the bulk diffraction lattice planes. It is element-specific and does not require long-range order. It is sensitive to both ordered structure and disordering. It has proven to be a very powerful surface analysis probe to study surface structures, surface thermal vibrations and surface kinetics. This technique has some limitations such as it is model dependent and requires high-quality crystalline substrates.

XSW is the principal technique used in the work of this thesis. Its basic principle, application and experimental implementation will be discussed in great details later in this thesis.

## *1.3 Silicon (001) clean and adsorbed surfaces*

### *1.3.1 Silicon (001) clean surface*

The surfaces of semiconductors play a crucial role in today's electronic and telecommunication industries. To date, Si has been the main material of semiconductor industry. This is true for many reasons. The attractive combination of its physical, electronic properties with the unique property of its native oxide layer was the original reason. Compared with other semiconductors, Si has a much higher availability, flexibility, reproducibility and is more economic. The Si-based semiconductor

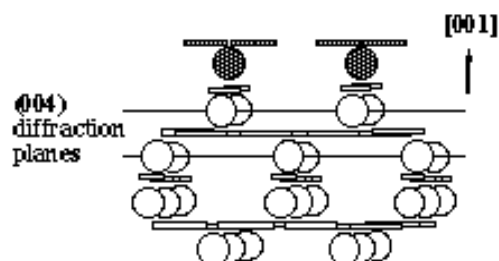
processing and device technology has been well-established over the past several decades. The dominant role of Si in semiconductor technology remains, despite intense efforts to develop alternative semiconductor systems.

Because of its practical importance and fundamental interest, an enormous amount of scientific and technical research efforts has been focused on Si, especially Si surfaces. Among the Si surfaces being studied, the three low index faces, namely (001), (011) and (111), have been given the most attention. In particular, the Si(001) surface has drawn the greatest scientific and technological interest because it is the surface used to manufacture most electronic devices.

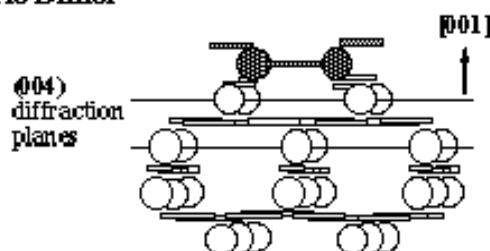
The first LEED study on the room temperature (RT) Si(001) surface observed half-order spots in two orthogonal ([100] and [010]) azimuths (a 2-domain 2x1 pattern) by Schlier and Farnsworth back in 1959 [109]. Their observation was easily explained by a (2x1) unit cell equally populated in two domains caused by single atomic steps on the Si(001) surface. Since the bulk truncated Si(001) surface has two single electron filled  $sp^3$  bonds ("dangling bond") per surface atom pointing out in a V shape from the surface (Fig. 1.2(a)), Schlier and Farnsworth reasonably proposed that two neighboring Si atoms were pulled together to form a dimer along the [110] direction (Fig. 1.2(b)). This reduces the number of dangling bonds on the surface by a factor of two and stabilizes the surface. These dimers are arranged in rows along the  $[\bar{1}10]$  direction and give a (2x1) surface unit cell as in Fig. 1.3. The change of domain due to single atomic steps rotates the Si dimer and the surface unit cell by  $90^\circ$  about the [001] direction (Fig. 1.3).

Figure 1.2 Ball-and-stick models of (a) the bulk truncated Si(001) surface, with each top layer Si atoms having two dangling bonds; (b) the Si(001) surface with symmetric dimers; (c) the Si(001) surface with buckled dimers due to the charge transfer, the Si atom with a filled lone-pair appears at a higher position.

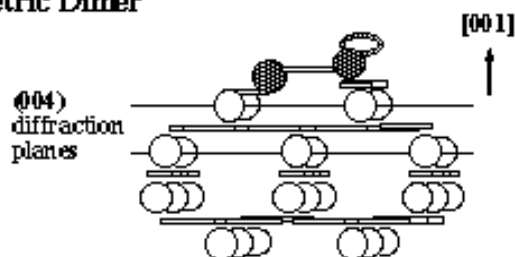
**(a) Bulk-terminated Si Surface**



**(b) Symmetric Dimer**

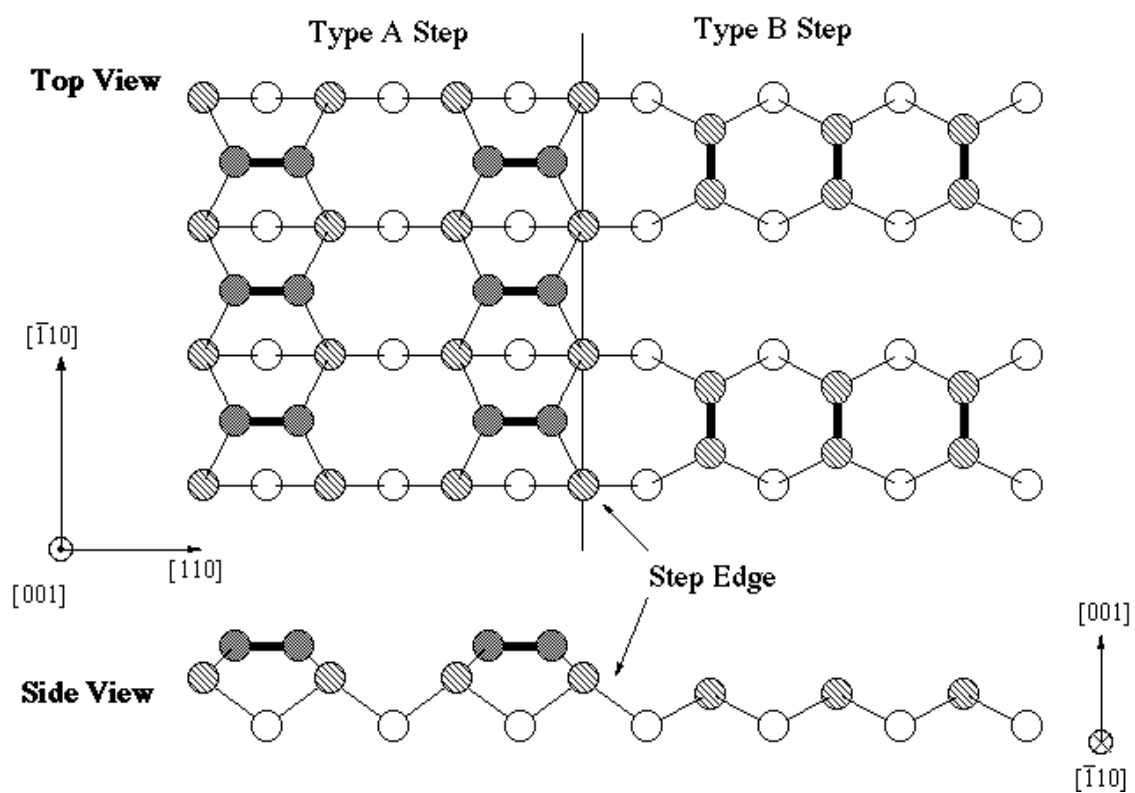


**(c) Asymmetric Dimer**



Top layer Si or adatoms
  Bulk Si
  Dangling bond
 
Filled Lone-pair

Figure 1.3 A top view and a side view of the two-domain (2x1) Si(001) surface due to single atomic steps. Si dimers are arranged in rows along the  $[110]$  and  $[\bar{1}10]$  orientations. There are two types of step: type A with dimer rows parallel to the step edge; type B with dimer rows perpendicular to the step edge.



Schlier and Farnsworth's finding was confirmed by later experiments (LEED [118, 133], photoemission [72], ICISS [1], Medium energy ion scattering [119], grazing incidence XRD [62], angle-resolved high-resolution electron-energy-loss spectroscopy (HREELS) [47], STM[53, 54, 120]) and theoretical calculations (pseudopotential total energy [8, 103, 134], tight-binding approximation [2, 33], first-principles molecular cluster (DMol) [113]). However, more questions were raised regarding the reconstruction of the Si(001) surface. Besides the (2x1) pattern which is the dominant phase, other LEED patterns (*e.g.* p(2x2) and c(4x4)) have been observed under certain circumstances [30, 31, 44]. More importantly, there has been a debate about whether the Si dimers are parallel to the surface (symmetric or non-buckled) (see Fig. 1.2(b)) or buckled (asymmetric) (see Fig. 1.2(c)). Using the tight-binding energy-minimization method, Chadi first predicted that buckled dimers are more stable than the symmetric dimers [33]. The reason behind the formation of buckled dimers is the charge transfer between the two Si atoms within an individual dimer. As illustrated in Fig. 1.2(c), the charge transfer leaves one Si atom with an empty lone-pair (no electron) and the other one with a filled lone-pair (two electrons). The empty lone-pair ends up at a lower position above the surface than the filled lone-pair [72]. Several calculations [103, 113] show that the energy difference between the symmetric and buckled dimers is very small (*e.g.* only 0.02 eV according to Ref. [113]). Is the Si dimer buckled?

In their pioneering STM study on the RT Si(001) surface, Tromp *et al.* showed that roughly equal numbers of symmetric and buckled dimers coexisted [120, 53, 54]. The symmetric dimers were mainly observed in defect-free areas while the buckled dimers existed near surface defects. However, the result of the first low-temperature STM experiment on Si(001) by Wolkow [130] indicated that the number of the buckled dimers increased drastically as the surface was cooled to 120 K and clearly revealed the

asymmetric character of the Si dimer. The real space STM image of the low temperature Si(001) surface provided an intuitive explanation to the p(2x2) (as buckled dimers in adjacent rows having the same buckling, see Fig. 1.4) and c(4x2) (as buckled dimers in adjacent rows having the opposite buckling, see Fig. 1.4) patterns observed by earlier LEED experiments. This was clearly confirmed by the most recent low temperature high quality STM images [63]. At RT, the 2x1 symmetric-looking dimers observed by these STM images are now explained to be the time-average result of flipping buckled dimers with a high frequency of  $10^{11}$  to  $10^{12}$  Hz (with a time scale much shorter than the STM imaging time). The idea that buckled dimers may rapidly interchange with symmetric dimers or simply flip found theoretical support in Refs [39, 129]. The buckled nature of Si dimers is now generally accepted.

### *1.3.2 Adsorption on the silicon (001) surface*

At the beginning of this section, it is convenient to introduce the notation that will be used in this thesis to describe the adsorbed phases and adsorption sites on Si(001). This notation is similar to that introduced by Wood [131]. If the adsorbate A induces a reconstruction on the Si(001) surface, with the basic translation vectors of  $|\mathbf{a}_s| = m|\mathbf{a}|$  and  $|\mathbf{b}_s| = n|\mathbf{b}|$ , where  $\mathbf{a}$  and  $\mathbf{b}$  are the translation vectors for unreconstructed Si (001) surface lattice, then this surface phase is labeled as (mxn) A/Si(001). The surface reconstruction lattice may be centered, in which case the notation would be c(mxn) A/Si(001).

In the ordered surface phases, adsorbates will only occupy certain adsorption sites on Si(001) based on simple symmetry arguments. These sites have commonly accepted labels. Illustrated in the left side of Fig. 1.5, the four adsorption sites on the (2x1) Si(001) reconstructed surface are "bridge", "valley bridge", "cave" and "pedestal". The

Figure 1.4 Various reconstructions on the Si(001) surface due to the dimer buckling: (a)  $c(4 \times 2)$  reconstructions with buckled dimers antiparallel both along and across the dimer rows; (b)  $p(2 \times 2)$  reconstructions with buckled dimers parallel across the dimer rows and antiparallel along the dimer rows.

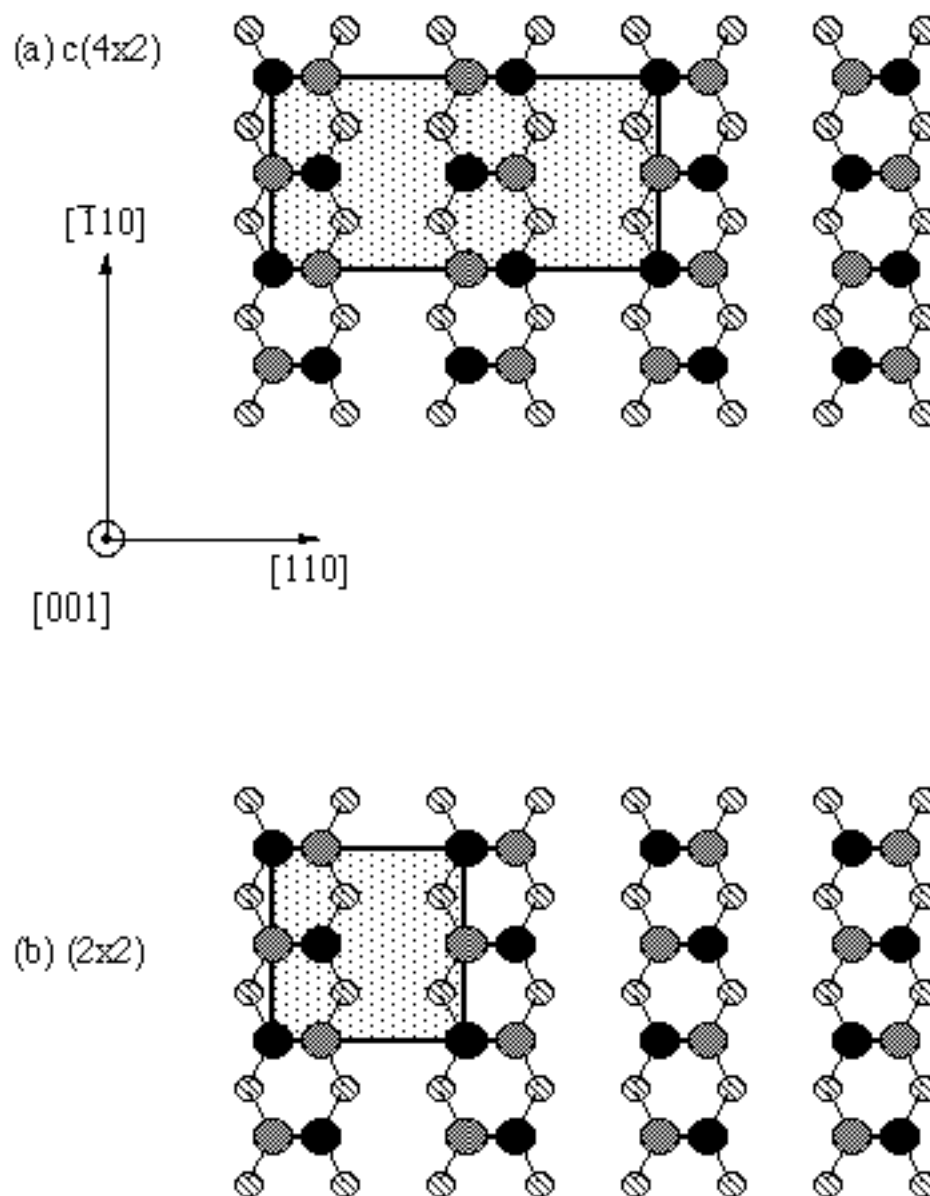
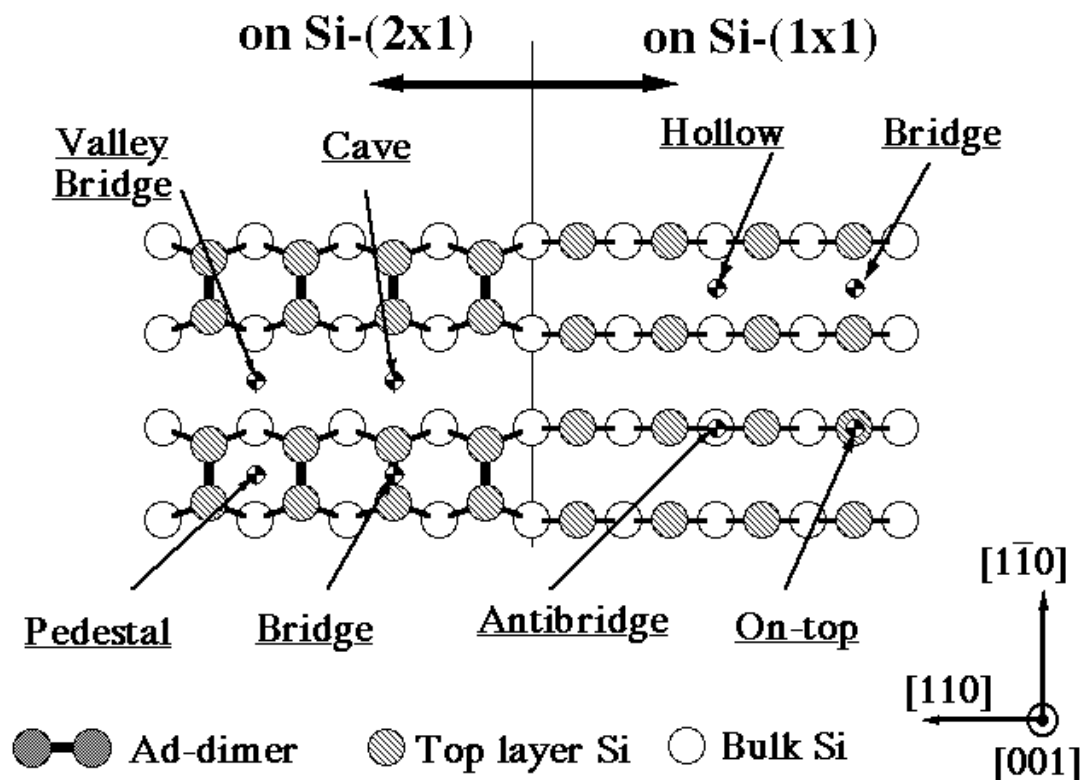


Figure 1.5 Adsorption sites on the (2x1) Si(001) reconstructed surface and the (1x1) Si(001) unreconstructed surface.



four adsorption sites on the (1x1) Si (001) unreconstructed surface are "bridge", "hollow", "antibrige" and "on-top" sites (right side of Fig. 1.5). All these adsorption sites have two-fold symmetry.

To date, more than 30 different elements have been shown to form more than 100 different surface phases on Si(001) at submonolayer coverages. Almost one quarter of these surface phases form (2x1) superstructures. Other common superstructures are (1x1) and (2xn) with n ranging from 2 to 13. Locally, most of these adsorbates form either monomers or dimers on the Si surface. The excellent handbook by Lifshits *et al.* contains very detailed information about these surface phases [76].

Among these surfaces, group III and V adsorbates induced surface phases have received much more attention for a number of reasons. From a surface science point of view, the adsorption of group III and V metals on Si (001) induces abundant and highly ordered superstructures with different substrate responses. Detailed information will be given in chapters IV, V and VI. These adsorbates all form ad-dimers on Si (001) and these ad-dimers have different orientations and adsorption sites under different conditions. These surfaces are of great interest and importance in terms of understanding fundamental surface science issues such as chemisorption, chemical bonding and adsorbate / substrate (adsorbate / adsorbate) interactions.

Technologically, Si(001) surfaces with group III and V adsorbates are of importance for many reasons. Historically, Si has been the major material in semiconductor industry. Recently, there is a tremendous effort to develop alternative systems such as III-V semiconductors (*e.g.* GaAs, InP) since III-V semiconductors are intrinsically high speed material and have direct band-gap which promises many electro-optical applications. However, technical difficulties in processing and manufacturing III-V materials hinders the development. The alternative way is to grow III-V

heteroepitaxial thin films on Si and therefore combine the advantageous properties of III-V semiconductors with the mature Si manufacturing technologies. Investigations of group III or V metals adsorbed on Si (001) surfaces will provide the necessary information for understanding the initial growth stage of III-V semiconductors on Si(001) [17, 18, 24, 25, 26, 27]. This may aid in eventually solving the technical difficulties associated with the III-V / Si heteroepitaxy such as the anti-phase domain problem [68].

The investigation of group V terminated Si(001) surfaces is also motivated by another important technological issue --- surfactant-mediated epitaxy (SME). Much effort has been put into the development of growing heteroepitaxial Ge thin films on Si. This runs parallel to the effort on III-V semiconductors and is similarly motivated. It has been found that preadsorption of a monolayer of certain foreign adsorbate (surfactant) species can to a certain extent change the growth mode of the Ge layer on Si from 3-dimensional growth to layer-by layer. Group V elements (As, Sb and Bi) have been found to be the most effective surfactants for the growth of Ge on Si (001) [29, 37, 42, 57, 74, 75, 107]. One widely accepted explanation of this surfactant effect is that a layer of surfactant atoms adsorbed and floating on the surface during growth can suppress island formation by reducing the surface energy and surface diffusion [36, 43]. However, the detailed mechanism regarding how the surfactant atoms remain on the surface during growth and how the growth kinetics are changed by the local structure is still unclear. Studying the submonolayer adsorption of group V elements on Si (001) may help in obtaining useful knowledge for fully understanding the initial growth stage of SME growth of Ge on Si(001). Other important issues associated with group III and V terminated Si(001) surfaces are surface passivations and delta doping layers [28, 86, 94].

With these scientific and technological importances, there is a great need to thoroughly understand atomic scale structures and adsorption behaviors of these group III

and V metal ad-dimers on the Si(001) surface. In the past, group III and V adsorbate terminated Si (001) surfaces have been studied intensively with a large variety of experimental techniques and theoretical approaches (detailed information will be presented in chapters IV, V and VI). Although these experiments and calculations yield their own pieces of information to the structure of these surfaces, these results are quantitatively far from agreement. There are still many unsolved problems and controversies that remain and a thorough picture of the group III and V adsorption geometry on Si(001) has yet to be established.

#### *1.4 Proposed work*

This thesis chooses to study group III and V adsorption on the Si(001) surface for the importance stated above. It is the aim of this thesis to set up a systematic method for obtaining atomic scale information about the structures, adsorption sites, bonding geometries, surface stabilities and thermal vibrations of these group III and V dimerized Si (001) surfaces. The XSW technique is chosen to be the primary experimental technique in the current study. This technique has proven to be a powerful probe for determining the microscopic structure, chemical composition, as well as dynamics and kinetics of the adsorbates on single crystal surfaces. It combines x-ray diffraction, interferometry and spectroscopy. Compared with other surface analysis techniques (*e.g.* LEED, Auger, STM, photoemission), it has superior spatial resolution. The adsorbate location relative to the substrate bulk lattice can be determined by XSW with an accuracy of 0.01 Å under favorable conditions. It is also chemically sensitive to the adsorbate / substrate chemical composition. At an unfocused synchrotron x-ray beamline like NSLS X15A, adsorbates with a concentration of  $10^{13}$  atoms / cm<sup>2</sup> at the surface or trace

elements with a concentration of  $10^2$  ppm in the bulk can be detected with XSW. Unlike conventional diffraction techniques such as LEED and x-ray diffraction, the XSW technique does not require the adsorbate to have long range order. It measures both the amplitude and phase of the Fourier component of the structure factor and therefore solves the phase ambiguity problem associated with conventional diffraction techniques.

In this thesis, a series of XSW measurements were carried out in UHV to precisely determine the ad-dimer locations, bond lengths and thermal vibrations for MBE grown submonolayer Ga/Si(001), Sb/Si(001) and Bi/Si(001) surfaces. By combining these measurements with measurements made by other techniques and theoretical calculations, additional information about the ad-dimer orientation and geometry and substrate relaxations are obtained. These results provide dependable information to confirm structural models predicted by theory and to solve certain controversies over the structure of these surfaces. Through these measurements, a methodology of determining the ad-dimer structure and thermal vibrations on the dimerized Si(001) surface is established. The current study in this thesis also tries to explore other capabilities of the XSW technique such as investigating surface kinetics.

This thesis is organized as follows: Chapter II offers a detailed introduction of the XSW technique. The experimental facilities and the general principle of XSW experimental procedure and data analysis are described in Chapter III. Chapter IV, V and VI are dedicated to the Sb/Si(001), Bi/Si(001) and Ga/Si(001) systems, respectively. Each of these three chapters is arranged in a similar way: It first provides a detailed introduction and background information about each individual surface system and then a description of surface preparation, experimental procedure; it then presents the results, followed by interpretations and discussions. The last chapter, Chapter VII, summarized the work and offers a few future outlooks. Readers can find detailed information about

the NSLS X15A beamline instrumentation and XSW data analysis procedures in the appendices.

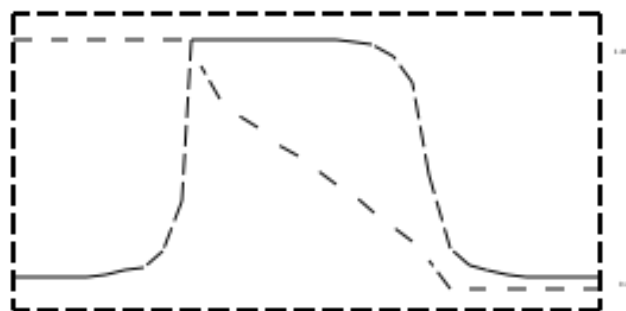
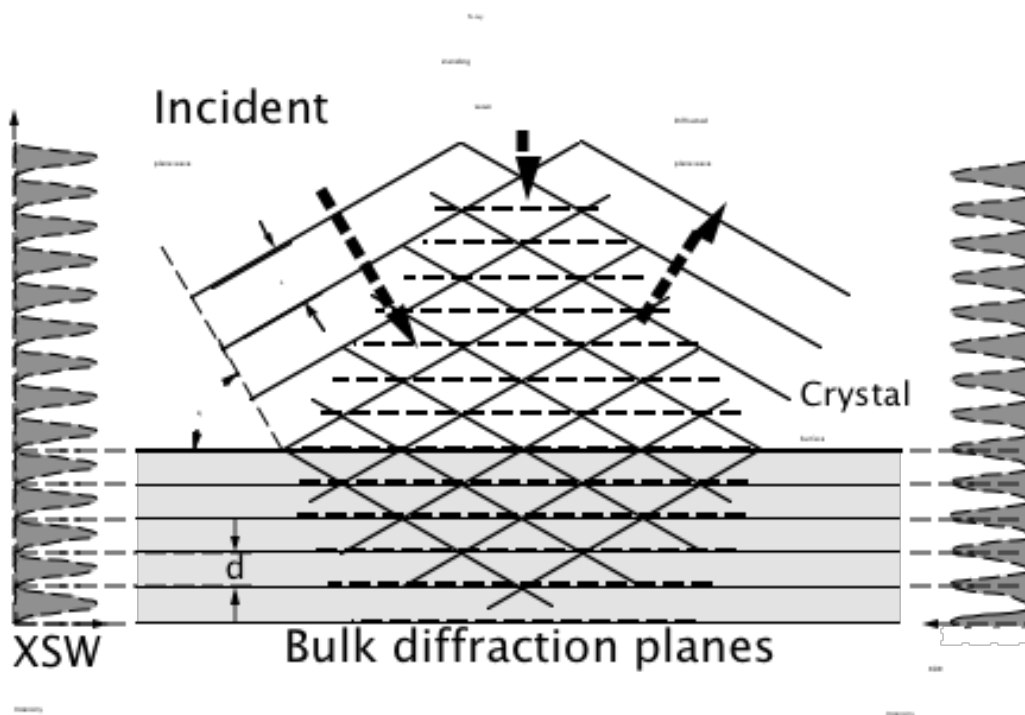
## Chapter II The X-Ray Standing Wave Technique

### 2.1 Historical review

Based on the dynamical theory of x-ray diffraction [9], an x-ray standing wave field is created by the interference of the incident and diffracted beams. The XSW exists not only in the crystal but also *above the crystal surface*. The nodes and antinodes of the XSW are parallel to and having the same periodicity as the responsible diffraction planes. As illustrated in Fig. 2.1, The phase of the standing wave with respect to the diffraction planes shifts by  $180^\circ$  as the Bragg angle  $\theta$  is scanned through the arc-second wide total reflection region of the Darwin curve. This inward sweep of the antinodal planes of the standing wave by one-half of the d-spacing ( $d_{hkl}$ ), results in a modulation in the photoelectron, Auger, and fluorescent yields from any atoms residing within the interference field. Hence, by monitoring the modulation of these yields as a function of the Bragg angle, the lattice locations of these atoms can determined.

Although the first observation of the x-ray interference during Bragg reflection was made by Borrmann in the case of the anomalous transmission of x-rays (the famous Borrmann effect) [21], it is now generally accepted that the x-ray standing wave (XSW) technique was first demonstrated by Batterman as he discovered a standing wave field occurring within a Ge single crystal during a Bragg reflection [10]. Later, by monitoring the As fluorescence yield from a doped Si(220) crystal, Batterman demonstrated that XSW can determine the location of a foreign atomic species within a bulk crystal [11].

Figure 2.1 X-ray standing waves generated within a perfect single crystal and above its surface by the Bragg diffraction. As the incident angle  $\theta$  is advanced through the rocking curve, the standing wave antinodes move inward by one half of d-spacing, from being lined up halfway between the diffraction planes (shown at left) to being lined up on the planes (shown at right) due to a  $180^\circ$  phase shift between the incident and diffracted beams.



It was later realized that the XSW also exists above the crystal surface. For the Br/Si(220) surface, Cowan, Golovchenko and Robbins made the first XSW experiment to determine the lattice location of an adsorbate in the normal direction above the surface [38]. Later, Golovchenko *et al.* demonstrated that the 3-dimensional adsorption site location can be determined by combining XSW measurements that use normal and off-normal Bragg reflections [51]. In the following 10 years, the XSW technique has been widely applied to study adsorbate structure on crystalline surfaces. Systems studied by XSW are: on Si(111): Ag, As, Au, Bi, Br, Cu, Ga, Ge, I, Pb, GaAs, CaF<sub>2</sub>; on Si(001): As, Bi, Br, Ga, Ge, Rb, Sb; on Ge(111): Br, Ga, I, Pb; on Ge(001): Sb; on Cu(111): Cl; on Cu(001): Cl; on Ni(111): S; on Ni(001): Cl (for references, see Ref. [136]). Besides the surface structure determination, the XSW technique has also been used to investigate surface thermal vibrations (Br/Ge(111) [13], Ga/Si(111) [82], As/Si(001) [49], Bi/Si(001) [80], Ga/Si(001) [98], Sb/Si(001) [99]), crystal polarity [12, 96], dispersion parameters and the phase problem [12, 14].

The XSW technique is not limited to applications on single crystals. An XSW field can also be generated by the total external reflection from a mirror surface or by Bragg reflection from a layered synthetic microstructures (LSM) such as amorphous multilayers of high-Z low-Z materials (*e.g.* Mo and Si) or Langmuir-Blodgett films [4, 15, 16, 128]. The XSW generated by a mirror or LSM has a longer standing wave period (from  $\sim 20$  Å to 2000 Å) in comparison to the very short period ( $\sim 1$  Å to 3 Å) for single crystal XSW. With this long length scale it is possible to study large molecules, long hydrocarbon chains and self-assembled-monolayers (SAM). It would be inappropriate to study these systems with the single crystal generated XSW. Since this long-period XSW was not used in the current study of this thesis, it will not be discussed further.

To understand interference phenomena related to Bragg reflection requires the dynamical theory of x-ray diffraction. This theory was developed by Darwin [41], Ewald [45] and von Laue [73] early in this century and its commonly accepted form is based on the formalism developed by von Laue. For a detailed description of the dynamical theory of x-ray diffraction, see Ref. [9].

## 2.2 Dynamical theory of x-ray diffraction

Considering x-ray plane waves as electromagnetic waves, the incident and diffracted waves can be characterized by their electric field (E-field) as:

$$\mathbf{E}_0 = E_0 \exp[2i(\omega t - \mathbf{K}_0 \cdot \mathbf{r})] , \quad (2.1)$$

and

$$\mathbf{E}_H = E_H \exp[2i(\omega t - \mathbf{K}_H \cdot \mathbf{r})] . \quad (2.2)$$

Here  $\omega$  is the photon frequency. Complex vectors  $\mathbf{K}_0$  and  $\mathbf{K}_H$  are the incident and diffracted beam wave vectors inside the crystal. Under the Bragg reflection condition, these two vectors are related by the following equation:

$$\mathbf{K}_H = \mathbf{K}_0 + \mathbf{H}, \quad (2.3)$$

where  $\mathbf{H}$  is the diffraction vector (real). (See Fig. 2.2.) Note that in the kinematical limit this reduces to a scalar equation corresponding to Bragg's law:

$$\lambda = 2 d \sin \theta_B . \quad (2.4)$$

$\lambda$  is the wavelength of the incident x-ray beam inside the crystal,  $d$  ( $= 1/|\mathbf{H}|$ ) is the d-spacing of the diffraction planes, and  $\theta_B$  is the Bragg angle.

The total electric field  $\mathbf{E}_T$  is the superposition of the incident and diffracted E-fields:

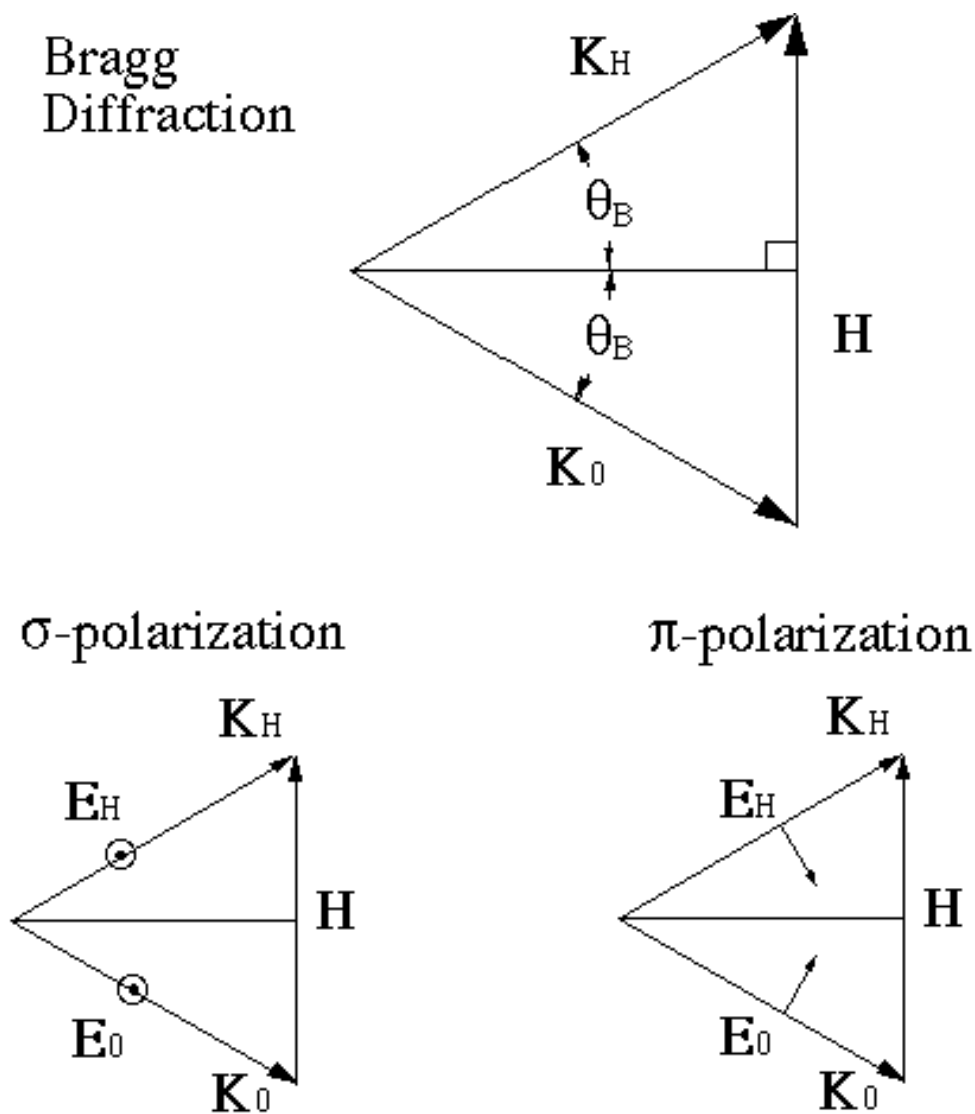
$$\mathbf{E}_T = \mathbf{E}_0 + \mathbf{E}_H = \lambda_b E_0 \exp[2\pi i(\lambda t - \mathbf{K}_0 \cdot \mathbf{r})] + \lambda_H E_H \exp[2\pi i(\lambda t - \mathbf{K}_H \cdot \mathbf{r})] . \quad (2.5)$$

**Error!**

$$\begin{aligned} \mathbf{E}_T &= \lambda_b \exp(2\pi i \lambda t) E_0 [ \exp(- 2\pi i \mathbf{K}_0 \cdot \mathbf{r}) + (E_H/E_0) \exp(- 2\pi i \mathbf{K}_H \cdot \mathbf{r}) ] \\ &= \lambda_b \exp(2\pi i \lambda t) \exp(- 2\pi i \mathbf{K}_0 \cdot \mathbf{r}) E_0 [ 1 + (E_H/E_0) \exp(- 2\pi i \mathbf{H} \cdot \mathbf{r}) ] . \end{aligned} \quad (2.6)$$

The complex ratio of the E-field amplitudes  $E_0$  and  $E_H$  of the incident and reflected waves is determined by the dynamical theory of x-ray diffraction [9]:

Figure 2.2 A reciprocal space vector diagram for Bragg diffraction (inside the crystal). For the  $\pi$ -polarization case, the incident and diffracted E-field vectors are collinear and normal to the scattering plane (this page). For the  $\sigma$ -polarization case, the incident and diffracted E-field vectors are in the scattering plane.



$$E_H / E_0 = -|b|^{1/2} \left( \frac{F_H \Delta}{F_{\bar{H}}} \right)^{1/2} \left[ \Delta \pm (\Delta^2 - 1)^{1/2} \right], \quad (2.7)$$

where the "reduced angle" parameter is a function of  $\Delta$  via

$$\Delta = \frac{b \Delta \sin(2\theta_B) F_H / 2(1-b) F_0}{|b|^{1/2} (F_H F_{\bar{H}})^{1/2}}. \quad (2.8)$$

$\Delta$  is defined as  $(\theta - \theta_B)$ . The asymmetry factor  $b$  is defined by

$$b = -\sin(\theta_B - \theta) / \sin(\theta_B + \theta), \quad (2.9)$$

where  $\theta$  is the "miscut angle", the angle between the diffraction planes and the surface of the crystal (Fig. 2.3). For the symmetric reflection,  $|b| = 1$ .  $\Delta$  is defined by

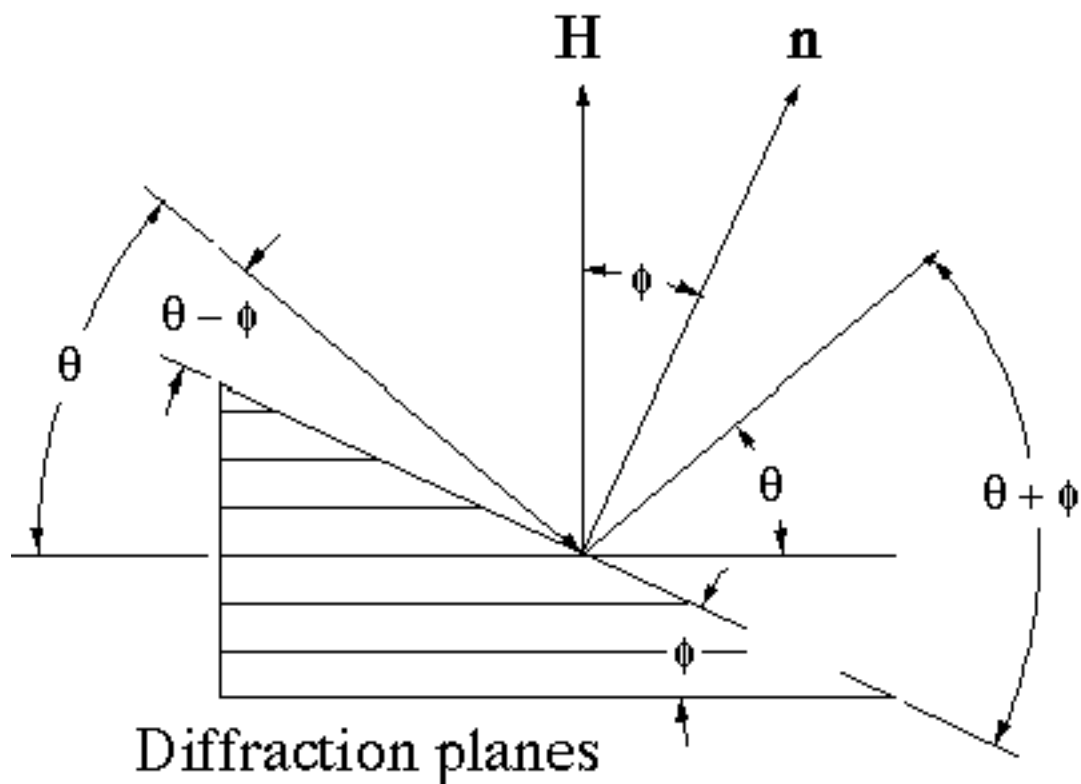
$$\Delta = r_e \lambda^2 / V_c, \quad (2.10)$$

where  $r_e = e^2 / mc^2 = 2.82 \times 10^{-5} \text{ \AA}$  is the classical electron radius and  $V_c$  is the unit cell volume.

$F_H$  is the structure factor for the  $\mathbf{H}$  Bragg reflection ( $d = 1/|\mathbf{H}|$ ). It is the  $H$ th Fourier component of the electron density  $\rho(\mathbf{r})$ ,

$$F_H = \int_V \rho(\mathbf{r}) \exp(2\pi i \mathbf{H} \cdot \mathbf{r}) dV. \quad (2.11)$$

Figure 2.3 The Bragg case geometry for an asymmetrically cut crystal.  $\mathbf{H}$  is the diffraction vector,  $\mathbf{n}$  is the surface normal vector,  $\phi$  is the miscut angle and  $\theta$  is the Bragg angle. (Glancing incidence is shown in the figure.)



It can further be described as the superimposed effect of the individual atomic scattering factors from within the unit cell,

$$F_H = \sum_{n=1}^N (f_0 + \Delta f' + i\Delta f'')_{n,H} \exp(2\pi i \mathbf{H} \cdot \mathbf{r}_n), \quad (2.12)$$

where the summation is over the  $N$  atoms of the unit cell. For the  $n^{\text{th}}$  atom at fractional unit cell position  $\mathbf{r}_n$ ,  $f_0$  is the atomic form factor, which accounts for elastic scattering (scattering from "free" electrons), and  $\Delta f'$  and  $\Delta f''$  are the anomalous dispersion corrections, which accounts for resonant scattering and absorption, respectively. Therefore, the structure factor is in general complex,

$$F_H = F'_H + i F''_H. \quad (2.13)$$

Where  $F'_H = \text{Re}[F_H]$  and  $F''_H = \text{Im}[F_H]$ . For a centrosymmetric crystal (such as Si), a suitable origin can be chosen such that  $F_H$  is equal to  $F_{\bar{H}}$ . This can simplify equations 2.7 and 2.8.

The complex ratio of the E-field amplitudes of Eq. 2.7 can be described in polar coordinates as:

$$E_H / E_0 = |E_H / E_0| \exp(iv), \quad (2.14)$$

The modulus  $|E_H / E_0|$  and phase  $v$  are plotted in Fig. 2.4 (a) and (b). Note that at the low angle side (where  $\theta > 0$ ) the incident and reflected plane waves are  $180^\circ$  out of phase and at the high angle side (where  $\theta < 0$ ) they are perfectly in phase.

The intensity of the reflected beam relative to the incident (*i.e.*, reflectivity  $R$ ) is :

$$R = |E_H / E_0|^2 . \quad (2.15)$$

Fig. 2.4 (c) plots a reflectivity curve for the case of a symmetric reflection ( $|b| = 1$ ). This curve is often referred to as the Darwin-Prins reflectivity curve (or rocking curve). The width for the rocking curve is defined by the angular range  $\Delta\theta = +1 \theta - 1 \theta$  where the rocking curve has a height close to unity. In  $\theta$  angular unit, this "Darwin width" is given by

$$\theta = 2 \theta F_H / [\sqrt{|b|} \sin(2\theta_B)] . \quad (2.16)$$

The center of the rocking curve (at  $\theta = 0$ ) is offset by an angle  $\Delta\theta = \theta F_0 / \sin(2\theta_B)$  relative to the Bragg angle  $\theta_B$ . This shift is due to the refraction index inside of the crystal.

For an asymmetric reflection ( $b \neq 1$ ), the angular width of acceptance  $\theta_{in}$  for the incident beam and the angular width of emergence  $\theta_{out}$  for the diffracted beam are

$$\theta_{in} = \theta / \sqrt{|b|} , \quad (2.17a)$$

$$\theta_{out} = \theta \sqrt{|b|} , \quad (2.17b)$$

and  $\theta_{out} = \theta_{in} |b| . \quad (2.17c)$

By substituting Eq. 2.14, Eq. 2.6 can be rewritten as:

$$E_T =$$

**Error!**

Figure 2.4 (a) The real and imaginary part of the E-field ratio  $\frac{E_H}{E_0}$  as a function of the relative Bragg angle. (b) The phase  $\nu$  of the E-field ratio. (For the symmetric Si(004) reflection at the photon energy of 12 keV).

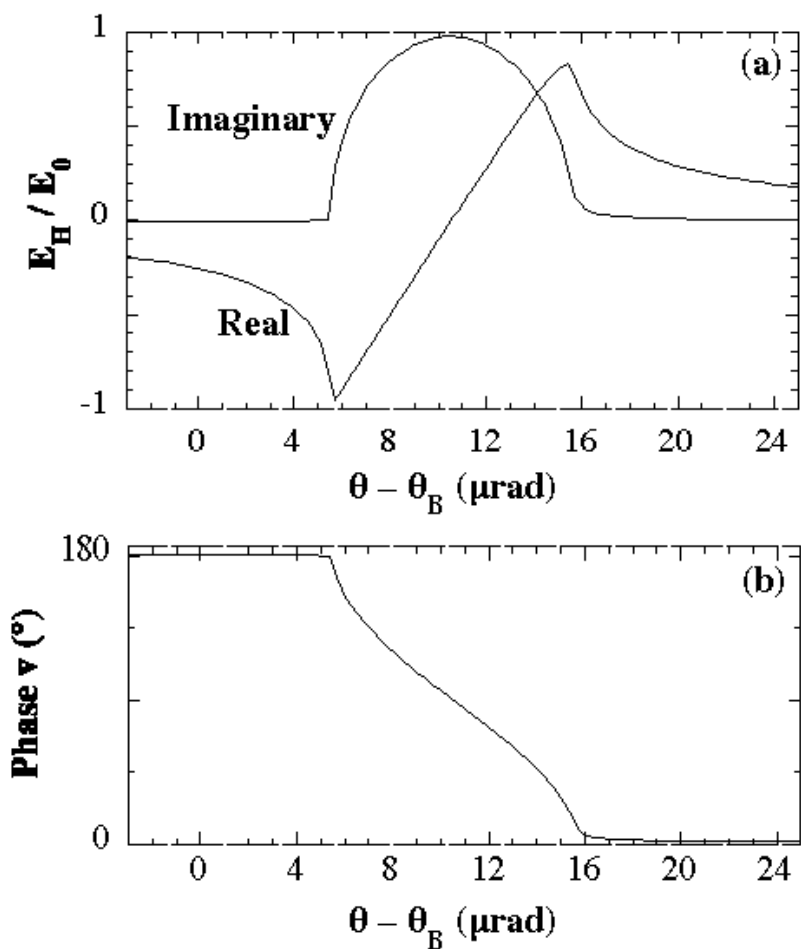
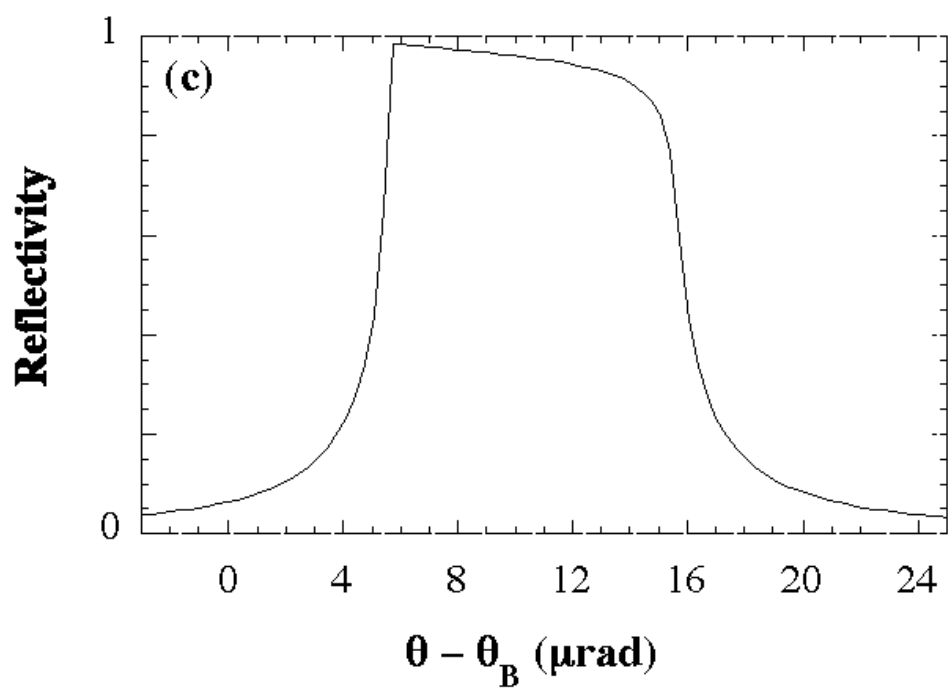


Figure 2.4 (c) A reflectivity curve (Darwin curve or rocking curve). For the symmetric Si(004) reflection at the photon energy of 12 keV.



Therefore, the E-field intensity is:

$$I = \mathbf{E}_T \cdot \mathbf{E}_T^* = |E_0|^2 [ 1 + R + 2\sqrt{R} \cos(\nu - 2\mathbf{H} \cdot \mathbf{r}) ] Z_{\text{abs}}, \quad (2.19)$$

where the term  $Z_{\text{abs}}$  accounts for the absorption. Inside the crystal, the absorption is accounted for by the exponential damping term as  $Z_{\text{abs}} = \exp(-\mu_z z)$ , where  $z$  is the depth below the surface and  $\mu_z$  is the effective linear absorption coefficient in terms of the linear absorption coefficient  $\mu_0 = \frac{2\mu_0 F''_0}{F''_0}$  :

$$\begin{aligned} \mu_z &= 4\mu_0 K''_0 \\ &= \mu_0 \left[ 1 + \frac{F''_H}{F''_0} \operatorname{Re}(E_H / E_0) + \frac{F'_H}{F''_0} \operatorname{Im}(E_H / E_0) \right] / \sin(\mu - \mu_0). \end{aligned} \quad (2.20)$$

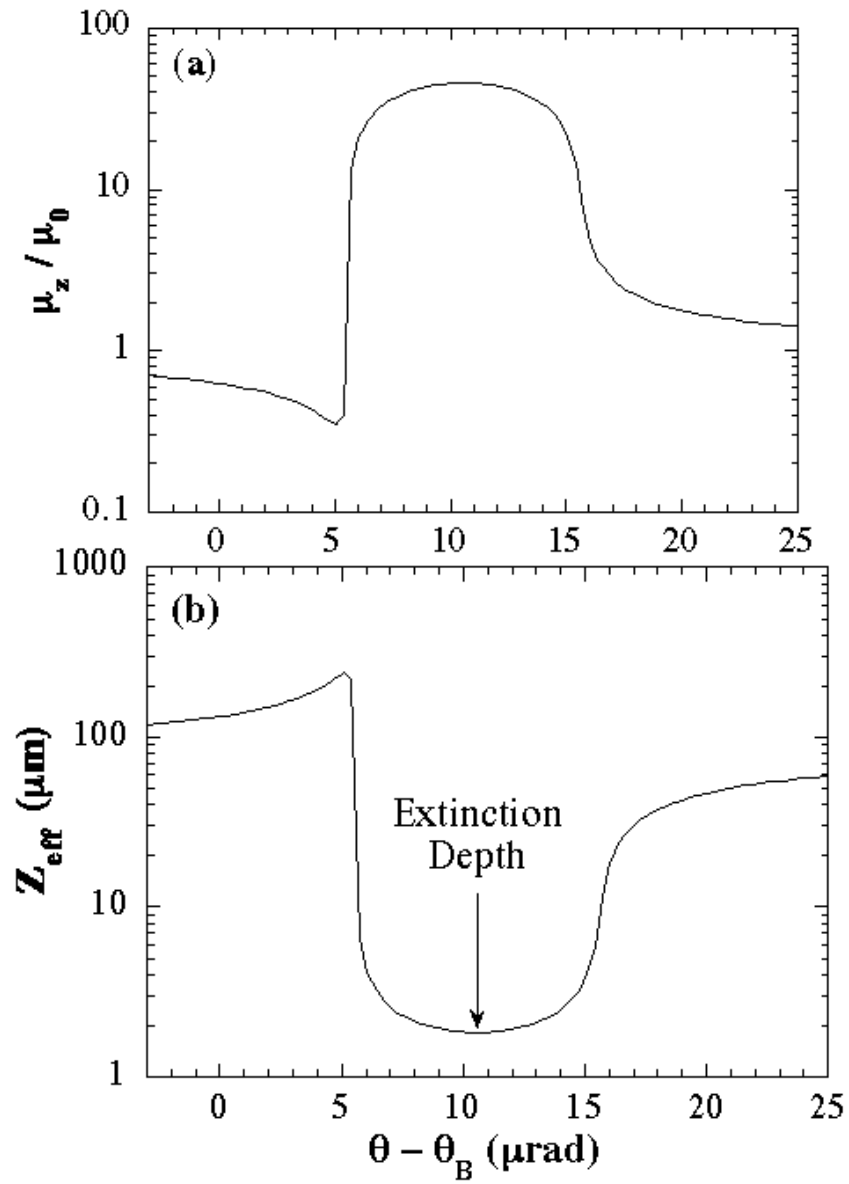
The first term in Eq. 2.20 corresponds to normal absorption, the second term corresponds to anomalous absorption, and the third term corresponds to primary extinction. The angular dependence of the effective linear absorption coefficient, normalized to unity off-Bragg, is depicted in Fig. 2.5(a). Fig. 2.5(b) illustrates the penetration depth, which is defined as:

$$Z = \mu_z^{-1}. \quad (2.21)$$

At the surface of the crystal (where  $z = 0$ ), there is no absorption to the x-ray where  $Z_{\text{abs}} = 1$ .

As pointed out before, the x-ray standing wave is created by the superposition of the incident and reflected plane waves. Thus, the E-field intensity  $I$  given by Eq. 2.19 is

Figure 2.5 (a) The normalized effective absorption coefficient and (b) The penetration depth for the Si(004) reflection at 12 keV. ( $\square$  polarization). The minimum penetration depth (or the extinction depth) is about 2  $\mu\text{m}$ .



that of the standing wave with constant intensity for a fixed  $\mathbf{H}\cdot\mathbf{r}$  or constant relative position  $\Delta d/d$  with respect to the diffraction planes. Therefore, the XSW period is equivalent to the d-spacing of the diffraction planes generated the XSW.

The phase  $\nu$  defined by Eq. 2.14 also represents the phase of the XSW relative to the plane which contains the unit cell origin (where  $\mathbf{r} = 0$ ). The choice of unit cell is arbitrary, but it has become customary to reference the standing wave phase with respect to the diffraction planes. If the unit cell origin is chosen to lay in the diffraction planes, then on the low angle side,  $\nu = 180^\circ$ , and the antinodes of the XSW are lined up halfway between the diffraction planes (at a relative position of  $\Delta d/d = 1/2$ ). On the high angle side,  $\nu = 0^\circ$ , and the antinodes of the XSW are on the diffraction planes. As the rocking curve is scanned in angle from the low-angle side to the high-angle side, the standing wave nodes and antinodes move inward by one half of a d-spacing due to this phase shift of  $180^\circ$  (Fig. 2.1).

### *2.3 The interaction of x-rays with solids*

X-ray waves interact with electrons in solids in the following ways: elastic scattering, thermal diffuse scattering, Compton scattering and photoelectric effect. Elastic (or coherent) scattering is characterized by the initial and final state of the x-ray waves having the same energy while the direction of propagation vector can change. Bragg diffraction is a special case of elastic scattering that takes place in crystals.

The thermal diffuse scattering (TDS) peak corresponds to incident x-rays scattering from phonons in the solid. Due to the relatively large effective mass of a phonon, a TDS scattered photon will only lose  $10^{-3}$  eV. This energy loss is insignificant

compared to the resolution of the Si(Li) detector. Hence, for energy calibration, the TDS peak is assigned the incident x-ray energy value.

Compton scattering is inelastic scattering. When an x-ray photon is scattered by an electron, it loses part of its energy. For an electron at rest, the Compton energy loss is:

$$\Delta E = \frac{E_0^2(1 - \cos\theta)}{m_e c^2 + m_e E_0(1 - \cos\theta)}, \quad (2.22)$$

where  $\theta$  is the angle between the incident and Compton scattering directions.

In the photoelectric effect, the energy of a photon is absorbed and a bound electron (photoelectron) is ejected from the atom with a kinetic energy:

$$E_K = h\nu - E_B, \quad (2.23)$$

where  $E_B$  is the binding energy of the electron. When an electron in a higher energy level drops down to fill the hole created by the photoelectron, a characteristic fluorescence photon or an Auger electron is emitted.

#### 2.4 The photo-effect cross-sections: Dipole approximation

The XSW technique uses the E-field intensity as a probe for inducing fluorescence from impurity atoms. The position sensitivity of this technique is based on the dipole approximation, which assumes that the fluorescence yield is proportional to the x-ray standing wave intensity at the center of the impurity atom.

In the photoelectric effect, a photon of energy  $E_\gamma = h\nu$  is absorbed. The energy  $E_\gamma$  is transferred to an electron which is excited from the ground state  $|i\rangle$  to a final state  $|f\rangle$ .

The transition probability for  $|i\rangle \rightarrow |f\rangle$  is proportional to the transition matrix element  $M_{fi}$ . The wave functions of the initial and final state are denoted as  $\psi_i$  and  $\psi_f$ , respectively. Applying first-order perturbation theory, the transition matrix element for the photoelectric transition induced by the electric field  $\mathbf{A}$  is

$$M_{fi} \propto \int d^3\mathbf{r}_e \psi_f^* \mathbf{A} \cdot \nabla \psi_i. \quad (2.24)$$

In this case,  $\mathbf{A}$  is the total E-field  $\mathbf{E}_T$  described by Eq. 2.5:

$$\mathbf{A} = \mathbf{E}_T =$$

**Error!**

The two position vectors  $\mathbf{r}_e$  and  $\mathbf{R}$  are related via

$$\mathbf{R} = \mathbf{r} + \mathbf{r}_e. \quad (2.26)$$

Here  $\mathbf{r}$  is the position vector of the center of the atom and  $\mathbf{r}_e$  is the position of the absorbing electron relative to the center of the atom. Thus Eq. 2.25 can be written as

$$\begin{aligned} \mathbf{A} = \mathbf{E}_T = & \frac{1}{2} \exp(2i\omega t) E_0 [ \exp(-2i\mathbf{K}_0 \cdot \mathbf{r}) \exp(-2i\mathbf{K}_0 \cdot \mathbf{r}_e) \\ & + (E_H/E_0) \exp(-2i\mathbf{K}_H \cdot \mathbf{r}) \exp(-2i\mathbf{K}_H \cdot \mathbf{r}_e) ] . \end{aligned} \quad (2.27)$$

The exponential function of  $\mathbf{r}_e$  can be expanded in a series as

$$\exp(-2i\mathbf{K}_0 \cdot \mathbf{r}_e) = 1 - 2i\mathbf{K}_0 \cdot \mathbf{r}_e + 2^2(\mathbf{K}_0 \cdot \mathbf{r}_e)^2 - \dots, \quad (2.28a)$$

$$\exp(-2i\mathbf{K}_H \cdot \mathbf{r}_e) = 1 - 2i\mathbf{K}_H \cdot \mathbf{r}_e + 2^2(\mathbf{K}_H \cdot \mathbf{r}_e)^2 - \dots \quad (2.28b)$$

In the dipole approximation, which assuming  $\mathbf{K}_0 \cdot \mathbf{r}_e \ll 1$  and  $\mathbf{K}_H \cdot \mathbf{r}_e \ll 1$ , only the first-order term is considered. Therefore, with  $\exp(-2i\mathbf{K}_0 \cdot \mathbf{r}_e) = \exp(-2i\mathbf{K}_H \cdot \mathbf{r}_e) = 1$ , Eq. 2.27 simplifies to

$$\begin{aligned} \mathbf{A} = \mathbf{E}_T &= \int d^3\mathbf{r}_e \exp(2i\mathbf{r}_e \cdot \mathbf{k}) E_0 [ \exp(-2i\mathbf{K}_0 \cdot \mathbf{r}_e) + (E_H/E_0) \exp(-2i\mathbf{K}_H \cdot \mathbf{r}_e) ] \\ &= \end{aligned}$$

**Error!**

and is no longer a function of  $\mathbf{r}_e$ . Thus Eq. 2.24 can be rewritten as:

$$\begin{aligned} M_{fi} &\propto \int d^3\mathbf{r}_e \exp(2i\mathbf{r}_e \cdot \mathbf{k}) E_0 \exp(-2i\mathbf{K}_0 \cdot \mathbf{r}_e) [ 1 + (E_H/E_0) \exp(-2i\mathbf{K}_H \cdot \mathbf{r}_e) ] \\ &\quad \cdot \mathbf{r}_e \cdot \mathbf{e}_i. \end{aligned} \quad (2.30)$$

Therefore, the fluorescence yield  $Y$  from a fluorescent atomic species, which is proportional to the photo-effect cross section, can be expressed as

$$\begin{aligned} Y &\propto |M_{fi}|^2 \propto \int d^3\mathbf{r}_e \exp(2i\mathbf{r}_e \cdot \mathbf{k}) E_0 \exp(-2i\mathbf{K}_0 \cdot \mathbf{r}_e) [ 1 + (E_H/E_0) \exp(-2i\mathbf{K}_H \cdot \mathbf{r}_e) ]^2 \\ &= |E_0|^2 [ 1 + R + 2\sqrt{R} \cos(\nu - 2\mathbf{K}_H \cdot \mathbf{r}_e) ] . \end{aligned} \quad (2.31)$$

Eq. 2.31 is only a function of  $\mathbf{r}$ , the position vector of the center of the fluorescent atom.

The influence of the quadrupole and higher order terms can become appreciable for very high x-ray energy or very small d-spacing. However, in most cases the

quadrupole cross section does not exceed the order of 1% of the dipole contribution [126] and therefore the dipole approximation is justified. The present XSW structural analysis methodology discussed in this thesis is based on the dipole approximation. If the quadrupole cross section is sizable in comparison to the dipole cross section, the XSW structural analysis would not be correct without taking the quadrupole effect into account.

## 2.5 XSW structural analysis

This section will discuss how the surface structure is determined by XSW analysis. If a particular fluorescent species has a spatial distribution function  $\rho(\mathbf{r})$ , where  $\mathbf{r}$  is a projected position into a unit cell and  $\int_{u.c.} \rho(\mathbf{r}) d\mathbf{r} = 1$ , then the total fluorescence yield  $Y$  from this species is:

$$\begin{aligned} Y &= \int_{u.c.} Y_{OB} [ 1 + R + 2\sqrt{R} \cos(\nu - 2\mathbf{H}\cdot\mathbf{r}) ] \rho(\mathbf{r}) d\mathbf{r} \\ &= Y_{OB} [ 1 + R + 2\sqrt{R} \int_{u.c.} \rho(\mathbf{r}) \cos(\nu - 2\mathbf{H}\cdot\mathbf{r}) d\mathbf{r} ] , \end{aligned} \quad (2.32)$$

where the off-Bragg fluorescence yield  $Y_{OB}$  is a normalization factor. The integral can be rewritten as following:

$$\begin{aligned} \int_{u.c.} \rho(\mathbf{r}) \cos(\nu - 2\mathbf{H}\cdot\mathbf{r}) d\mathbf{r} &= \frac{1}{2} \int_{u.c.} \rho(\mathbf{r}) \exp(i\nu) \exp(-2i\mathbf{H}\cdot\mathbf{r}) d\mathbf{r} + \\ &\quad \frac{1}{2} \int_{u.c.} \rho(\mathbf{r}) \exp(-i\nu) \exp(2i\mathbf{H}\cdot\mathbf{r}) d\mathbf{r} \\ &= \frac{1}{2} \exp(i\nu) \left[ \int_{u.c.} \rho(\mathbf{r}) \exp(2i\mathbf{H}\cdot\mathbf{r}) d\mathbf{r} \right]^* + \\ &\quad \frac{1}{2} \exp(-i\nu) \int_{u.c.} \rho(\mathbf{r}) \exp(2i\mathbf{H}\cdot\mathbf{r}) d\mathbf{r} . \end{aligned} \quad (2.33)$$

The Hth Fourier component  $F[\rho(\mathbf{r})]$  can be expressed by its amplitude  $f_H$  and phase  $P_H$  via:

$$F[\rho(\mathbf{r})] = \int_{u.c.} \rho(\mathbf{r}) \exp(2\pi i \mathbf{H} \cdot \mathbf{r}) d\mathbf{r} = f_H \exp(2\pi i P_H) , \quad (2.34)$$

then Eq. 2.33 can be simplified as:

$$\begin{aligned} \int_{u.c.} \rho(\mathbf{r}) \cos(\nu - 2\pi i \mathbf{H} \cdot \mathbf{r}) d\mathbf{r} &= \frac{1}{2} \exp(i\nu) [f_H \exp(2\pi i P_H)]^* + \\ &\quad \frac{1}{2} \exp(-i\nu) f_H \exp(2\pi i P_H) \\ &= \frac{1}{2} f_H \exp(i\nu) \exp(-2\pi i P_H) + \frac{1}{2} \exp(-i\nu) f_H \exp(2\pi i P_H) \\ &= f_H \cos(\nu - 2\pi P_H) . \end{aligned} \quad (2.35)$$

Thus, the total fluorescence yield for a distribution of atoms at the surface of a single crystal is:

$$Y = Y_{OB} [ 1 + R + 2\sqrt{R} f_H \cos(\nu - 2\pi P_H) ] . \quad (2.36)$$

The data from each XSW measurement of a surface adsorbate has the functional form of Eq. 2.36 with three fitting parameters  $Y_{OB}$ ,  $f_H$  and  $P_H$ . The off-Bragg fluorescence yield  $Y_{OB}$  is a normalization factor and is directly proportional to the adsorbate coverage. This constitutes the zeroth Fourier component of the adsorbate distribution.

The two parameters  $f_H$  and  $P_H$  are commonly known as coherent fraction and coherent position. They are the amplitude and phase, respectively, of the Hth Fourier component of the time-averaged spatial distribution of the nuclei of the atoms (projected into a unit cell). In general, it is expressed as

$$f_H = |F[\mathbf{r}]|, \quad (2.37a)$$

$$P_H = \frac{1}{2} \tan^{-1} \left( \frac{\text{Im}(F[\mathbf{r}])}{\text{Re}(F[\mathbf{r}])} \right) + \begin{cases} 1/2, & \text{if } \text{Re}(F[\mathbf{r}]) < 0 \\ 0, & \text{otherwise} \end{cases}. \quad (2.37b)$$

The coherent fraction  $f_H$  measures the adsorbate's ordering and geometric arrangement. Since XSW measurements are sampling a huge ensemble of atoms (typically  $10^{14}$ ) and averaging over time, not only the static distribution but also the thermal vibration of the adsorbate have to be taken into account. Approximating the thermal vibration time-average distribution with a Gaussian and based on the convolution theorem for Fourier transform, the coherent fraction can be written as the product of three factors [13]:

$$f_H = C a_H D_H. \quad (2.38)$$

The ordered fraction  $C$  is the fraction of atoms at ordered positions and has a value from zero to unity, where unity stands for complete ordering and zero corresponds to a completely random distribution. The geometrical factor  $a_H$  measures the adsorbate's atomic arrangement. The Debye-Waller factor  $D_H$  accounts for the adsorbates thermal vibration.

Let us consider the situation where  $N$  inequivalent ordered adsorption sites denoted by  $\mathbf{r}_1, \mathbf{r}_2, \dots, \mathbf{r}_N$  are occupied by a certain adatom species with occupation fractions of  $C_1, C_2, \dots, C_N$ , respectively. Then the ordered fraction is:

$$C = \sum_{n=1}^N C_n. \quad (2.39)$$

In reality, the ordered fraction  $C$  may not be 100% and there will be a certain fraction of adatoms which are randomly distributed when projected onto a one-dimensional scale with a length equivalent to the  $d$ -spacing. Based on Eq. 2.37a and 2.37b, the geometrical factor and coherent position can be expressed as:

$$a_H = \frac{1}{N} \left| \sum_{n=1}^N \frac{C_n}{C} \exp(2\pi i \mathbf{H} \cdot \mathbf{r}_n) \right|, \quad (2.40)$$

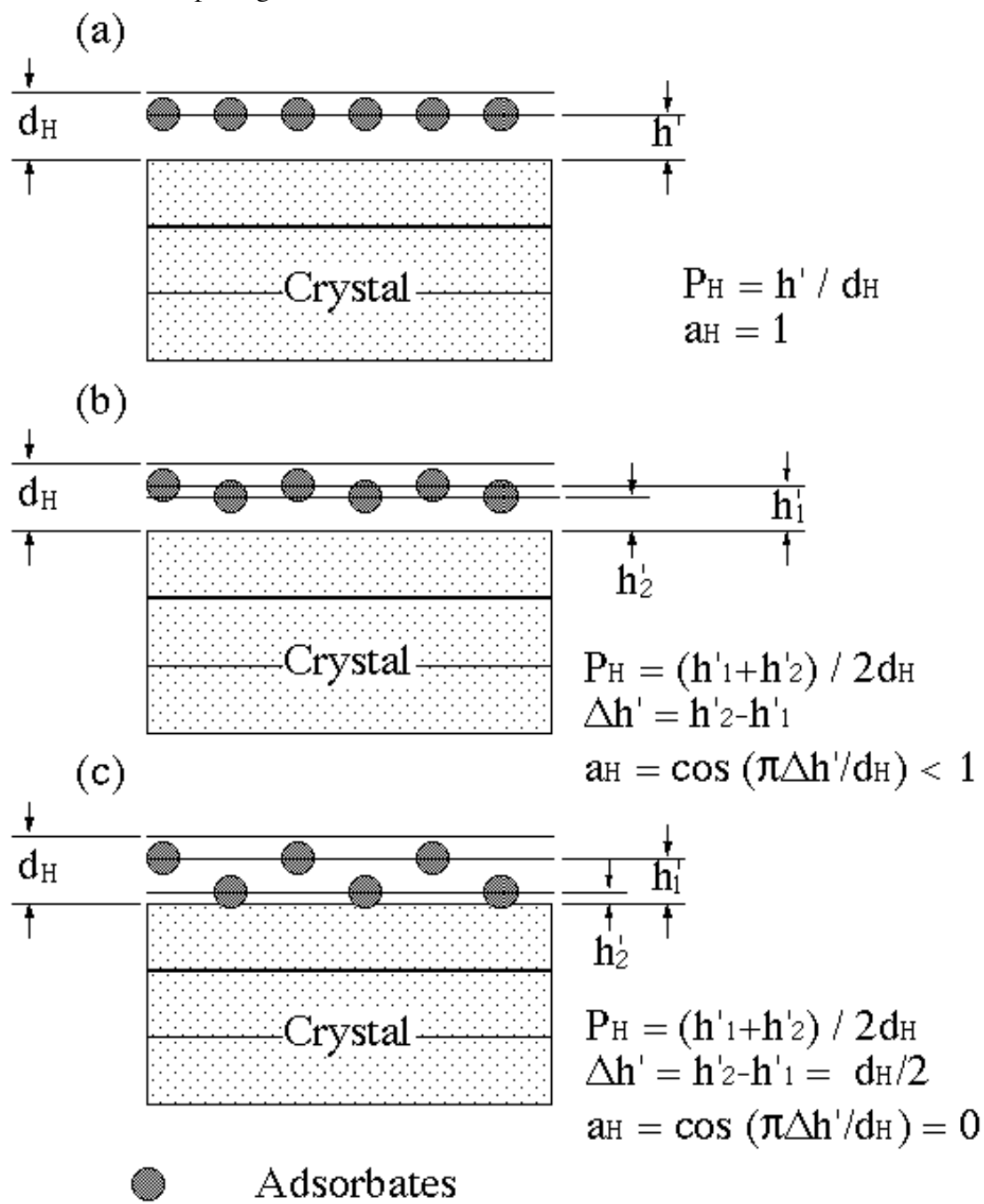
and

$$P_H = \frac{1}{2\pi} \text{Arg} \left[ \sum_{n=1}^N C_n \exp(2\pi i \mathbf{H} \cdot \mathbf{r}_n) \right]. \quad (2.41)$$

In simple terms, the coherent position  $P_H$  is a  $\Delta d/d$  fractional position (mod 1) relative to the bulk diffraction planes. The coherent position has a value range from zero to unity. The coherent position of zero or unity correspond to the case which the average adsorbate position is on the diffraction planes (where the origin is usually chosen) and the coherent position of one half corresponds to the position half-way between the diffraction planes. The geometrical factor  $a_H$  ranges also from zero to unity. Figure 2.6 illustrates a few examples to demonstrate the meaning of  $a_H$ . It is unity if there is only one ordered site (Fig. 2.6(a)). If there are multiple sites, the geometrical factor  $a_H$  will be less than unity (Fig. 2.6(b)). For example, if there were two equally occupied sites separated by one half of a  $d$ -spacing, the geometrical factor  $a_H$  is equal to zero (Fig. 2.6(c)). This is analogous to the structure factor for a forbidden reflection.

The XSW technique is extremely sensitive to the change of the coherent position, or the lattice location of the adatom relative to the bulk diffraction planes. To

Figure 2.6 Examples illustrating the meaning of the geometrical factor  $a_H$  and the coherent position  $P_H$ . (a) Adsorbates have only one ordered site; (b) Adsorbates have two equally occupied sites; (c) Adsorbates have two equally occupied sites separated by one half of a d-spacing.



demonstrate the sensitivity, Fig. 2.7 plots a series of hypothetical fluorescence yield curves corresponding to ten different coherent positions varying from 0.0 to 1.0. Although the coherent positions only differ by 0.1 (corresponding to a 10% d-spacing difference in real space) between the two neighboring curves, the difference in their modulations can be easily identified by eye. Typically, the adatom location can be measured by XSW with a precision of 1~2% of the d-spacing. For XSW measurements using the Si(004) reflection, the uncertainty is  $\pm 0.02 \text{ \AA}$ .

## 2.6 XSW analysis of the dimerized surface

The structure and adatom's thermal vibration for the group III(V) metal/Si(001) dimerized surface can be resolved by employing XSW measurements using the Si (004), (022) and (008) reflections. As shown in Fig. 2.8, group III (or V) adsorbates are expected to form symmetric (non-buckled) ad-dimers on Si(001) and have two equally occupied unit cell positions. Although there are (1x2) and (2x1) domains on the Si(001) surface due to single atomic steps in which ad-dimers are rotated  $90^\circ$  to each other, ad-dimers in these two domains give identical positions when projected along the [004] or [022] directions. Therefore, the problem can be analyzed in terms of a one-domain (1x2) structure.

Along the [004] direction, every adatom resides at the same height  $h'$  above the Si (004) bulk-like diffraction planes (Fig. 2.8). Therefore, the geometrical factors for the (004) and (008) reflections are unity ( $a_{004} = a_{008} = 1$ ). The ad-dimer height  $h'$  above the

Figure 2.7 A series of the hypothetical fluorescence yield curves for a surface adatom species with the coherent position  $P_H = 0.0, 0.1, 0.2, 0.3, \dots, 1.0$ . For simplicity, the coherent fraction is set to be unity. All the curves are calculated for the Si(004) reflection at 12 keV.

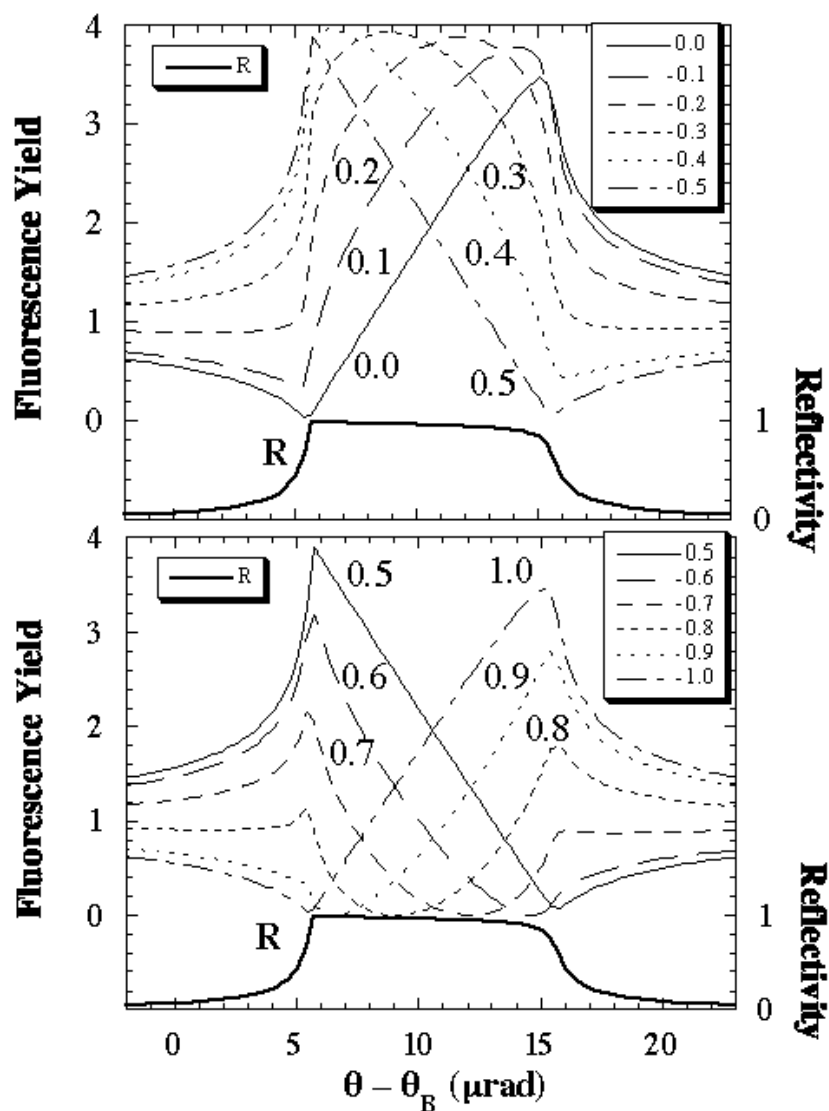
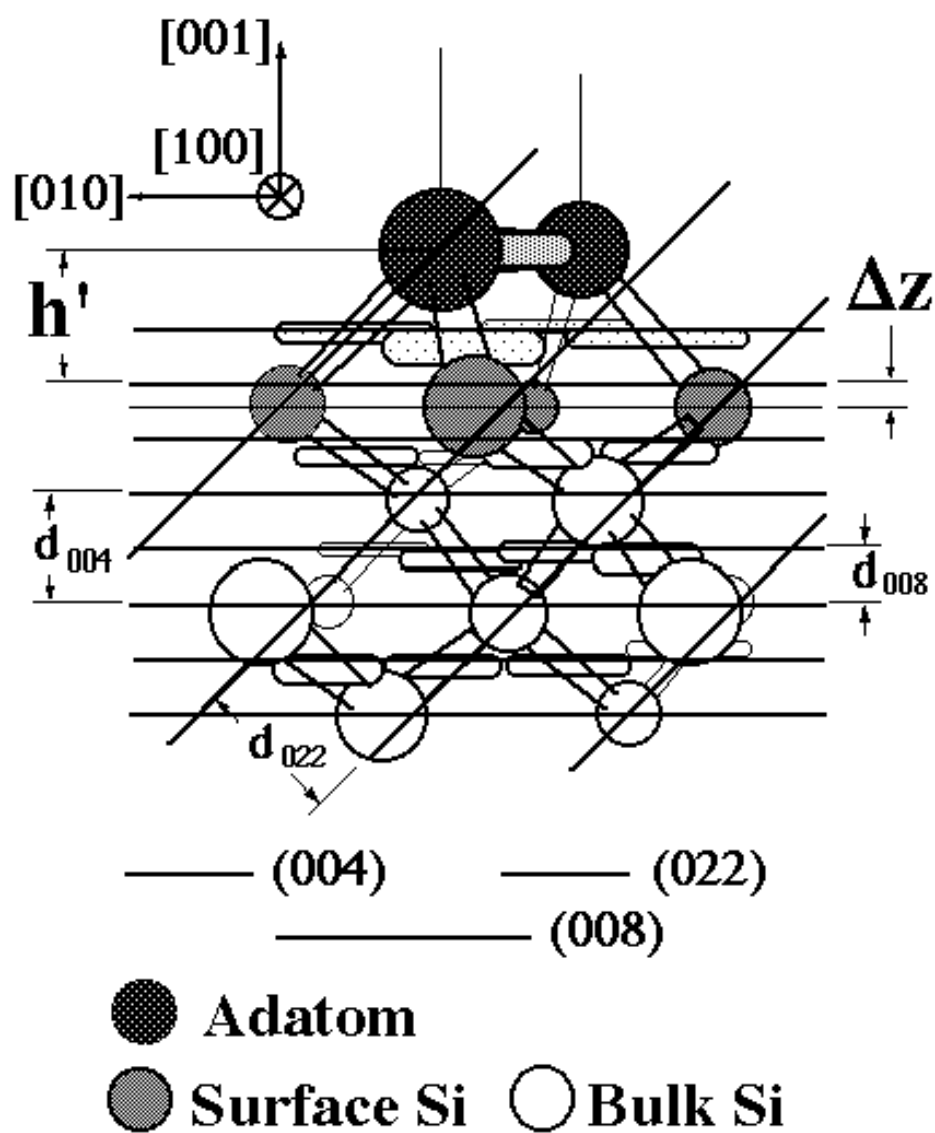


Figure 2.8 A side view of the group III and V metal/Si(001) surface ad-dimer model. The Si (004), (022) and (008) diffraction planes are represented by different sets of dashed lines. The solid line represents the height of the relaxed Si(001) surface.  $h'$  is the ad-dimer height above the bulk-like Si(001) surface atomic layer,  $\Delta z$  is the inward relaxation of the top Si layer, and  $L$  is the ad-dimer bond length. Note that the ad-dimer bond does not lie in the plane of the figure.



bulk extrapolated (004) lattice planes can be determined by the (004) XSW measurement:

$$h' = P_{004} d_{004}. \quad (2.42)$$

In terms of nearest neighbor distances, the adatom's height  $h$  above the real (relaxed) surface can be measured by SEXAFS. Therefore, the relaxation of the top Si surface layer can be determined by the combination of XSW measurements with SEXAFS measurements:

$$\Delta z = h - h'. \quad (2.43)$$

In the [022] direction the two adatom positions have inequivalent projections (Fig. 2.8), so that the geometrical factor (Eq. 2.40) is:

$$a_{022} = |\cos(\pi L/2d_{022})|, \quad (2.44)$$

where  $L$  is the ad-dimer bond length. Therefore, the ad-dimer bond length  $L$  can be determined by a combined (004) and (022) measurements based on Eqs. 2.38 and 2.44:

$$L = \frac{2d_{022}}{\pi} \cos^{-1} \left( \frac{f_{022} D_{004}}{f_{004} D_{022}} \right). \quad (2.45)$$

$f_{004}$  and  $f_{022}$  are the XSW measured coherent fractions.  $D_{004}$  and  $D_{022}$  are the Debye-Waller factors which account for thermal vibrations and their determination will be described later.

If the ad-dimer distribution is centered above any one of the two-fold symmetry sites (illustrated in Fig. 1.5), the (022) measured coherent position  $P_{022}$  would have a relationship with  $P_{004}$  as:

$$P_{022} = (1 + P_{004})/2 . \quad (2.46)$$

The XSW experiment can also measure thermal vibrational amplitudes of adatoms relative to the bulk lattice by employing higher order harmonic measurements [13]. Thermal vibrations smear the time-averaged spatial distribution of adatoms so that the distribution function is no longer a  $\delta$ -function. Assuming the adatom's thermal vibration as a Gaussian distribution, the Debye-Waller factor can be expressed in terms of the ad-atom's thermal vibrational amplitude  $\sqrt{\langle u_H^2 \rangle}$  as:

$$D_H = \exp(-2\pi^2 \langle u_H^2 \rangle / d_H^2) . \quad (2.47)$$

For the group III(V) metal / Si (001) dimerized surface, the adatom's thermal vibration amplitude along the [001] direction can be determined by the combined (004) and (008) XSW measurements. As pointed out earlier, the geometrical factors  $a_{004}$  and  $a_{008}$  are unity for unbuckled dimers. Based on Eqs. 2.38 and 2.47, if the ordered fraction ( $C$ ) remains constant during the combined (004) and (008) XSW measurements, the thermal vibrational amplitude along the [001] direction can be determined from the measured (004) and (008) coherent fractions as:

$$\sqrt{\langle u_{001}^2 \rangle} = \frac{d_{004}}{\sqrt{6} \pi} \sqrt{\ln \frac{f_{004}}{f_{008}}} . \quad (2.48)$$

If individual atoms have a symmetrical time-averaged distribution about their mean position(s) (*i.e.* the thermal vibration mode is harmonic), the relation between the (008) and (004) coherent position is simply:

$$P_{008} = h/d_{008} = 2P_{004}. \quad (2.49)$$

If the adatom's thermal vibration is anharmonic, which is probably true at the surface due to the asymmetry of the bonding geometry, this relation does not hold.

The (004)-(008) XSW combination also determines the surface ordered fraction (C) by the following equation:

$$C = f_{004} \left[ \frac{f_{004}}{f_{008}} \right]^{1/3}. \quad (2.50)$$

## Chapter IV Sb/Si(001) Surface

### *4.1 Sb adsorption on Si(001): Background information*

The Sb/Si(001) system has attracted considerable attention in recent years for its implications to technologically important issues. The adsorption of Sb on Si(001) is the first step in the fabrication of Sb delta-doping layers [123]. A proper choice of adsorption parameters such as substrate temperature and Sb coverage is important for obtaining narrow delta-doping layers. Recently, Sb has been found as a good surfactant in Ge/Si(001) epitaxy [29, 37, 43]. Understanding the growth behavior of Sb on Si(001) is the basis of understanding the mechanism and better controlling the process of surfactant-mediated epitaxy. The submonolayer Sb growth on Si is also important in terms of improving the quality of III-V epitaxy on Si, since it represents the initial stage of III-V semiconductors on Si. Academically, the Sb/Si(001) surface also serves as a prototype to study the group V metal adsorption on the Si(001) dimerized surface.

Experimentally, this system has been studied by a variety of techniques such as LEED [52, 91, 102, 110], RHEED [100, 101], core level spectroscopy [100, 101], STM [91, 101, 102], SEXAFS [102], medium energy ion scattering [110] and transmission MeV ion channeling [52]. STM results [91, 102], revealed that a Sb/Si(001) surface prepared at 375° C is disordered. To obtain a ordered layer of Sb, it is necessary to deposit Sb at 550°C or to anneal the surface to 550°C after deposition. A two-domain (1x2) LEED pattern with diffused half order spots was observed on the annealed Sb/Si(001) surface. STM images [102] show that Sb forms ad-dimers on the Si surface

and the Sb ad-dimers are centered at the hollow site and arranged in rows, resulting in the (1x2) symmetry. Photoemission results [100, 101] suggested that the Si(001) (2x1) reconstruction is removed by the Sb adsorption and the Sb dimers are on top of nearly bulk-like Si, similar to the behavior of As atoms on Si(001) [121]. As the pentavalent Sb atoms can form three bonds (and one lone-pair orbital), and the tetravalent, top-layer Si atoms can form four bonds, there are no dangling bonds, and the surface is rather passive [28]. The saturation coverage of Sb is somewhat less than a full monolayer, ranging from 0.7 to 0.9 ML [110]. STM [91] often observed broken Sb dimer rows on the surface due to defects and the surface strain caused by the Sb / Si size mismatch. These broken dimer rows are often shifted laterally to form anti-phase domains with short coherence lengths. This explains the diffuseness and weakness of the half-order spots observed with electron diffraction. Quantitatively, the structure of the Sb/Si(001)-(1x2) system has been measured by SEXAFS [102] and transmission MeV ion channeling [52].

In addition to these experiments, several calculations have been performed to investigate the stability and structure of the Sb/Si(001) surface using the first-principles molecular cluster approach (DMol) [114] and a total energy calculation within the local-density approximation (LDA) [135]. These calculations confirmed the fact that the Sb adsorption as dimers passivates the Si(001) surface. These calculations [114, 135] also predicted values for the surface structure.

Although these experiments and calculations provided their own pieces of information to the structure of the Si(001)/Sb-(1x2) surface, these results are quantitatively far from agreement. Besides static structure, there is no information about the surface thermal vibration. A thorough picture of the Sb adsorption geometry on Si(001) has yet to be established.

To investigate the structure and adsorbate thermal vibration, a series of XSW measurements employing both fundamental and high-order harmonic reflections have been undertaken on MBE grown saturated Sb/Si(001) surfaces as a part of work in this thesis. Structural parameters such as Sb dimer bond length, Sb dimer height above the bulk extrapolated Si(001) surface, Sb adsorbate thermal vibration amplitude and surface ordering have been obtained with a high precision from these XSW experiments. By combining SEXAFS results [102], the Si(001) surface relaxation upon Sb adsorption is also estimated. These high-resolution XSW measurements provide quantitative details about the surface that can be used as a stringent test for theoretical models. The following section 4.2 will present details of surface preparation and procedures of XSW experiments. The experimental results and the interpretation of these results are discussed in the section 4.3. The section 4.4 summarizes the results.

## *4.2 Experimental*

### *4.2.1 Sample preparation*

The Si (001) samples used in this thesis work are specially cut and polished from high-purity float-zone Si (001) boules. Each sample is 4 mm thick and has a 10 mm x 10 mm square surface and two wings for mounting. (For details about the sample and sample mounting, see Appendix A.1) Before introduction into the UHV system, each Si(001) sample was Syton™ polished to obtain a smooth surface. To remove contaminants from the sample surface and to form a protective oxide layer, a chemical etching process called the Shiraki etch [59] was performed. The sample was then mounted on a molybdenum (Mo) sample holder and held in place by tantalum (Ta)

springs to avoid possible permanent strain induced during annealing. (See Appendix A.1) The sample and holder was loaded into the UHV system through the load-lock port and transported into the sample preparation chamber for further *in situ* cleaning and deposition. First, the sample was annealed to 600°C to degas water vapors and other gases absorbed on the sample and the holder. Usually, the degassing procedure lasts from 6 hours to a full day. The next procedure was to flash the sample to 900°C for 10 minutes to remove the oxide layer. After flashing, the sample was slowly cooled to RT (initial cooling rate  $\approx 2.0^\circ \text{C}/\text{sec}$ ). During the flashing, the pressure would go up to as high as  $10^{-9}$  torr but would drop back to  $10^{-10}$  torr immediately after the flashing. Usually, it takes two to three flash anneals to completely remove the oxide layer.

The sample was then transported to the analysis chamber to check with the LEED and AES. A characteristic sharp two-domain (2x1) LEED pattern was observed for the Si(001) clean surface. AES could detect no O and only a small amount of C contamination ( $\sim 0.03 \text{ ML}$ ).

The Si(001) sample was then transported back to the preparation chamber for MBE evaporations. The Sb was evaporated onto the Si sample from a Knudsen cell held at 400°C. At this temperature, the Sb vapor (consists of Sb tetramers [5]) flux near the sample surface was detected to be  $\sim 0.3 \text{ ML}/\text{min}$  by the thickness monitor. To prepare the saturated Sb/Si(001) surface,  $\approx 3 \text{ ML}$  of Sb was deposited from the Knudsen cell over 10 min with the Si substrate held at 550° C. Since the sticking coefficient for Sb adsorption goes to zero at coverages greater than 1 ML [110], approximately 1 ML Sb was adsorbed on the surface. The Sb-saturated surface was further annealed for 5 minutes at 550°C to reach equilibrium on the surface. After cooling to RT, a two domain (1x2) LEED pattern with slightly diffuse half-order spots was observed. This is consistent with previous LEED studies [52, 91, 102, 110].

#### 4.2.2 XSW Measurements

The "as-deposited" sample was then transported to the x-ray chamber for XSW measurements. To investigate the structure, bonding geometry and adatom's thermal vibration for the saturated (1x2) Sb/Si(001) dimerized surface, XSW measurements using the Si (004), (022) and (008) Bragg reflections were performed. The energy of the incident photon from the monochromator was tuned to 6.23 keV for the (004) measurement, 6.77 keV for the (022) measurement and 9.60 keV for the (008) measurement. These energies were above the Sb L absorption edges, therefore, Sb L fluorescence were excited from the surface. For the (022) measurement, the angle  $\theta$  of the sample was tilted 45° from the [001] direction (which is the surface normal) towards the [010] direction (along one of the sample edges). During the (008) measurement, an Al foil was placed between the monochromator and the sample to attenuate the coexisting 4.8 keV incident photons from the (004) reflection to less than 1%. To double check the stability of the surface, another (004) XSW measurement was then taken immediately after the (008) measurement. Fig. 4.1 (a), (b) and (c) illustrate experimental data for the Si reflectivity and Sb L fluorescence yield as well as best fits of the dynamical diffraction theory (Eq. 2.36) for the Si (004), (022) and (008) reflections on that surface, respectively. For the saturated Sb/Si(001) surface, the measured coherent fractions and coherent positions are:  $f_{004} = 0.73 \pm 0.02$ ,  $P_{004} = 1.21 \pm 0.01$ ,  $f_{022} = 0.52 \pm 0.01$ ,  $P_{022} = 1.10 \pm 0.01$ ,  $f_{008} = 0.33 \pm 0.03$ ,  $P_{008} = 0.42 \pm 0.01$ .

Figure 4.1 The experimental and theoretical curves for the x-ray reflectivity and Sb L fluorescence yield for: (a) the Si (004) reflection at  $E_{\square} = 6.23$  keV and (b) the Si (022) reflection at  $E_{\square} = 6.77$  keV.

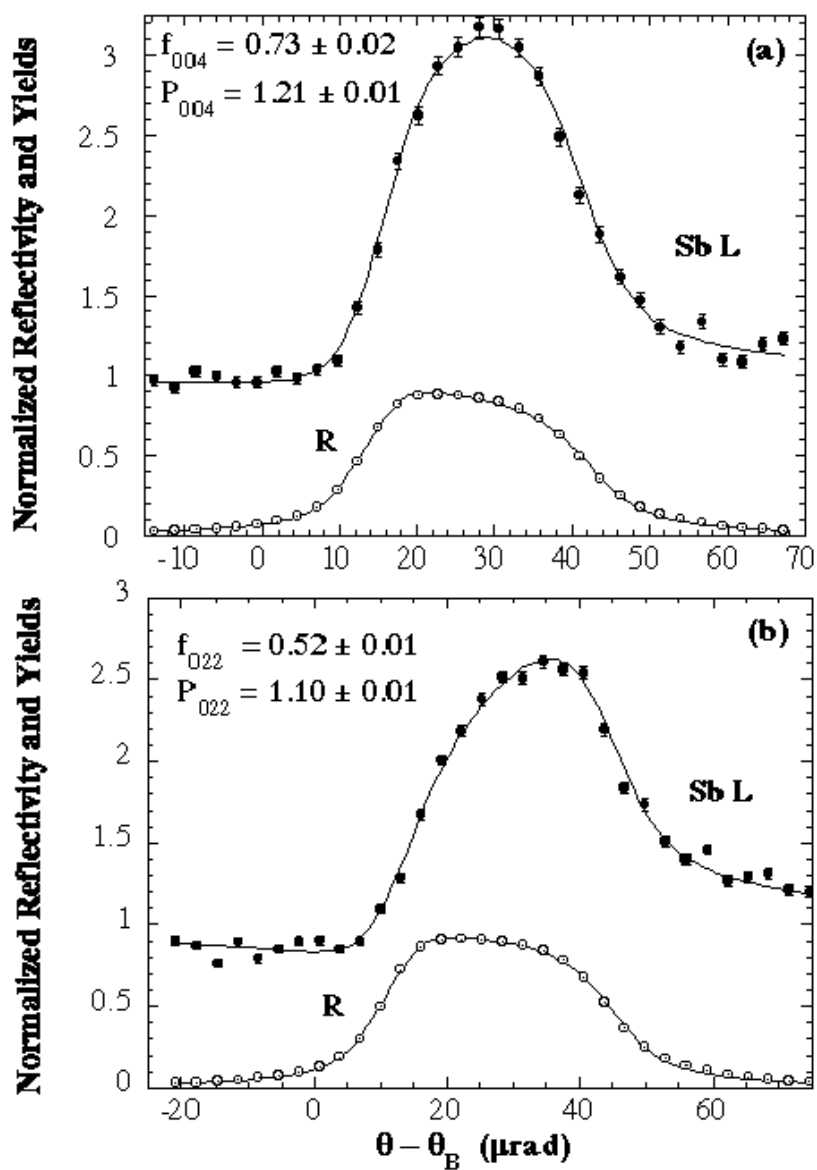
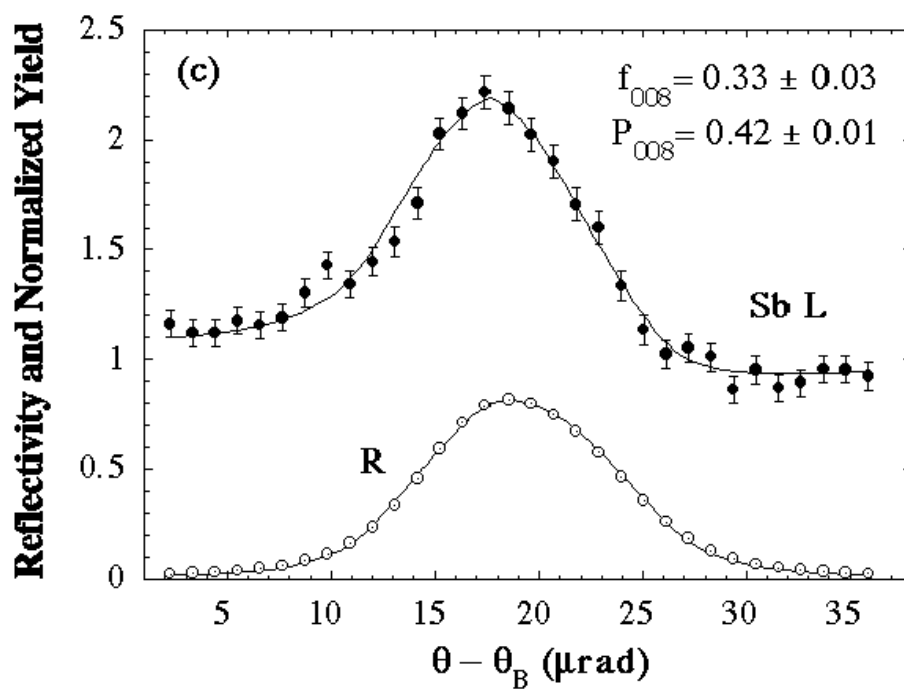


Figure 4.1 (c) The experimental and theoretical curves for the x-ray reflectivity and Sb L fluorescence yield for the Si (008) reflection at  $E_{\square} = 9.6$  keV



### 4.3. Results and Discussion

#### 4.3.1 Substrate Relaxation

The measured value of  $P_{004} = 1.21 \pm 0.01$  indicates that the Sb ad-dimer is located at a height  $h' = P_{004} d_{004} = 1.64 \pm 0.02 \text{ \AA}$  above the Si(004) bulk-like atomic planes (by Eq. 2.42). The measured value of  $P_{022}$  is  $1.10 \pm 0.01$ ; the fact that this value is equivalent to  $(1+P_{004})/2$  (see Eq. 2.46) confirms that the local Sb structure is symmetrically centered about one of the two-fold symmetry sites of the surface (Fig. 1.5). By chemical bonding symmetry consideration, this site has to be the hollow site.

In a SEXAFS experiment, Richter *et al.* [102] measured the bond lengths for this surface system, finding a Sb-Si bond length of  $2.63 \pm 0.04 \text{ \AA}$  and a Sb-Sb bond length of  $2.88 \pm 0.03 \text{ \AA}$ . Assuming a symmetric dimer geometry, the SEXAFS values imply that the Sb ad-dimer resides  $h = 1.74 \pm 0.05 \text{ \AA}$  above the surface Si plane. Therefore, as shown in Chapter II by Eq. 2.43, the combination the XSW and SEXAFS results indicates that the top layer Si atoms on the saturated (1x2) Sb/Si(001) surface are relaxed inward by  $0.10 \pm 0.05 \text{ \AA}$  at room temperature.

Transmission MeV ion channeling has also been applied to this surface system [52]. This technique bears many similarities to XSW, as well as some important differences. A principal advantage of XSW compared to transmission MeV ion channeling is its superior precision ( $0.02 \text{ \AA}$  for XSW vs. about  $0.1 \text{ \AA}$  for ion channeling [48]). Grant *et al.* [52] made a determination of the position of the Sb dimer above the bulk-like surface planes using transmission MeV ion channeling, and inferred the value of the Si surface plane relaxation. They reported a Si surface relaxation of  $0.09 \pm 0.07 \text{ \AA}$ ,

which was based on a symmetric dimer geometry, an assumed Sb-Si bond length of 2.63 Å, a measured Sb-Sb dimer length of  $2.8 \pm 0.1$  Å and a measured height of the Sb atoms above the bulk-like surface plane of  $1.63 \pm 0.07$  Å [52]; note, however, that the cited uncertainty in the relaxation does not include any contribution from uncertainty in the assumed Sb-Si bond length. The ion channeling results are consistent with our measurements within cited experimental error. However, XSW measurements in this thesis provide a much more precise and more direct determination of these structural parameters, and furthermore are based entirely on experimentally determined quantities.

The XSW results for the Si relaxation in this thesis also compare favorably to theoretical calculations of Group V/Si(001) adsorption systems. In a first-principles cluster calculation, Tang *et al.* [114] calculated the inward relaxation of the top layer Si atoms on the 1 ML Sb/Si(001) surface to be  $0.05 \pm 0.05$  Å. Result of the current study is also consistent with the pseudopotential calculation [121] of the relaxation of the As-terminated Si(001) surface (0.09 Å), which should exhibit a relaxation comparable to the present case.

#### 4.3.2 Thermal vibrational amplitude and surface ordering

As shown in Chapter II by Eq. 2.48, the thermal vibrational amplitude can be determined from  $f_{004}$  and  $f_{008}$  if the ordered fraction  $C$  is constant. For the saturated Sb/Si(001) surface, the same  $f_{004}$  and  $P_{004}$  values for the (004) scans taken before and after the (008) measurement were obtained. This indicates that the surface structure and the ordering are very stable over a long period of time ( $\sim 30$  hours) taken by the combined (004) and (008) measurements. With measured coherent fractions  $f_{004} = 0.73 \pm 0.02$  and  $f_{008} = 0.33 \pm 0.03$  and using Eq. 2.48, the thermal vibrational amplitude of the

Sb adatom in the [001] direction at room temperature is found to be  $0.156 \pm 0.01$  Å. From Eq. 2.50 the corresponding Sb ordered fraction is determined to be  $C = 0.95$  for this surface preparation. This indicates that 95% of the Sb adsorbed on the Si surface is forming ordered ad-dimers. This does not conflict with the STM findings that Sb dimers form anti-phase dimers which contribute incoherently to the LEED pattern. In fact, these anti-phase Sb ad-dimers are identical when projected into bulk [004] and [022] unit cells and therefore contribute coherently to XSW fluorescence yields. This is one of the advantages of the XSW technique over the conventional diffraction-based techniques (LEED, RHEED and XRD) since it does not require a long-range order. The measured Sb  $\sqrt{\langle u_{001}^2 \rangle}$  will be compared with other measured and calculated values of  $\sqrt{\langle u_H^2 \rangle}$  for related systems in Chapter VII.

The measured value of  $P_{008}$  is  $0.42 \pm 0.01$ . This value is exactly equal to twice the  $P_{004}$  value (mod. 1). This indicates that the Sb time-averaged distribution about their mean position is symmetric (*i.e.* the thermal vibration mode of Sb ad-atoms at RT is harmonic).

### 4.3.3 Dimer bond length and geometry

To describe the geometry of symmetric Sb dimers, another piece of information needed to be specified is the Sb-Sb bond length  $L$ . As shown before, this quantity can be determined by using Eqs. 2.44 and 2.45, if the Debye-Waller factor for the Sb adatoms along both [001] and [011] direction are known. In the current study, the Sb  $\sqrt{\langle u_H^2 \rangle}$  along the [001] direction were directly measured, as shown in the previous subsection. However, there is a lack of any direct measurement for the thermal vibrational amplitude along the [011] direction. Therefore, an assumption is made that the thermal vibrational

amplitude of Sb on the (1x2) Sb/Si(001) surface at room temperature to be isotropic, which is consistent with calculations for the clean Si(001) surface [85], and XSW measurements of the As/Si(001) surface [49]. Using the XSW measured  $\sqrt{\langle u_H^2 \rangle}$  value, the Debye-Waller factors are  $D_{004} = 0.77 \pm 0.03$  and  $D_{022} = 0.88 \pm 0.02$ . Eq. 2.45 then lead directly to a value of the Sb-Sb bond length  $L$  of  $2.75 \pm 0.06$  Å.

Table 4.1 compares the structural parameters derived in this study under the assumption of symmetric dimers with previous theoretical and experimental studies of the saturated Sb/Si(001) surface system. Both experiments and calculations agree with each other on the Sb ad-dimer height and the top Si layer relaxation but disagree on the Sb dimer bond length. The XSW measured Sb dimer bond length value is in good agreement with that determined by ion channeling ( $2.8 \pm 0.1$  Å) [52] and is also consistent with the Sb-Sb covalent bond length of 2.76 Å. However, the bond length value measured by SEXAFS ( $2.88 \pm 0.04$  Å) [102] and predicted by the DMol calculation ( $2.93 \pm 0.05$  Å) [114] and LDA calculation (2.96 Å) [135] are longer than the XSW measured value by 5% to 7%.

The above calculation of the Sb dimer bond length from the XSW measured values is based on the structural model which assumes that the Sb dimers are centered with respect to the underlying substrate and parallel to the surface. However, it was recently reported that on the Sb/Ge(001) surface the mid-point of the Sb dimer was shifted along the bond direction by 0.16 Å [77] (see Fig. 4.2). This interesting structure of midpoint shift has never before been reported for any (1x2) Group V/Si(001) surface system. For a midpoint shifted dimer, the (022) geometrical factor  $a_{022}$  is then a function of the bond length  $L$  and the shift as:

$$a_{022} = |\cos(\pi L/2d_{022})\cos(\pi \delta/d_{022})|, \quad (4.1)$$

Table 4.1. Theoretical and experimental values of structural dimensions for the saturated (1x2) Sb/Si(001) surface.  $L$  is the Sb ad-dimer bond length.  $h$  and  $h'$  are the height of the Sb ad-dimer relative to the relaxed and unrelaxed Si(001) surface atomic planes, respectively.  $\Delta z$  represents the inward relaxation of the top layer Si(001) atoms. (For the (1x2) Sb/Si(001) surface model, See section 2.5 Fig. 2.7.)

	Theory			Experiment	
	DMol <sup>a</sup>	LDA <sup>b</sup>	Ion Chanl. <sup>c</sup>	SEXAFS <sup>d</sup>	Present XSW
$L$ (Å)	$2.93 \pm 0.05$	2.96	$2.8 \pm 0.1$	$2.88 \pm 0.03$	$2.75 \pm 0.06$
$h$ (Å)	1.73	1.70		$1.74 \pm 0.05$	
$h'$ (Å)	1.68		$1.63 \pm 0.07$		$1.64 \pm 0.02$
$\Delta z = h-h'$ (Å)	$0.05 \pm 0.05$		$0.09 \pm 0.07$	$0.10 \pm 0.05$	

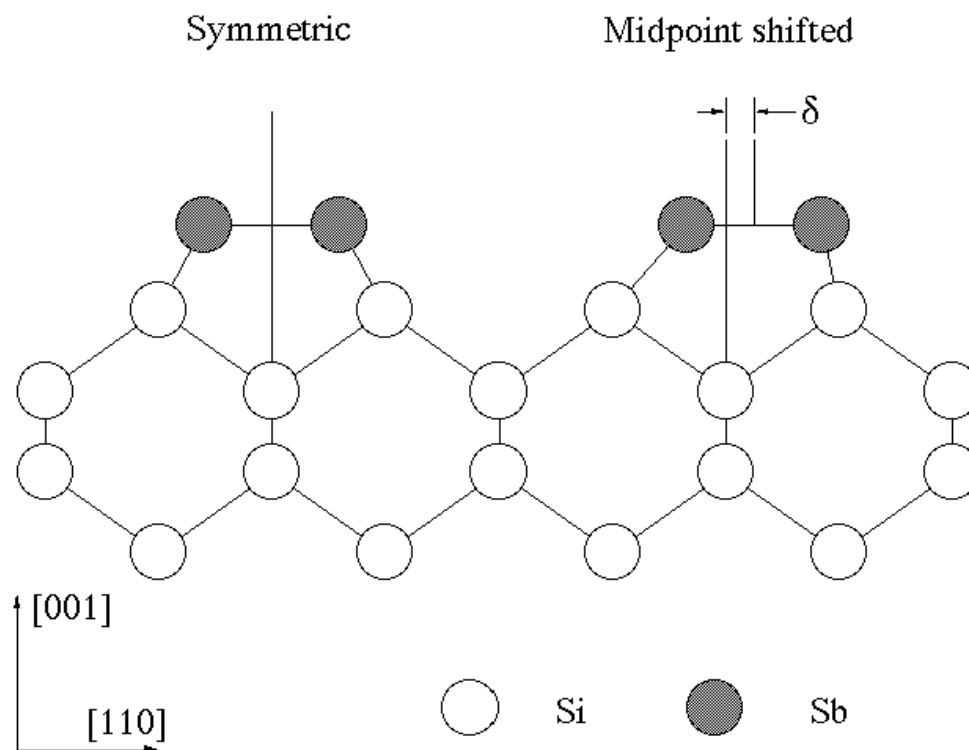
<sup>a</sup> Ref. [114].

<sup>b</sup> Ref. [135].

<sup>c</sup> Ref. [52].

<sup>d</sup> Ref. [102].

Figure 4.2 A side view of the Sb/Si(001) surface ad-dimer models (symmetric and midpoint shifted).

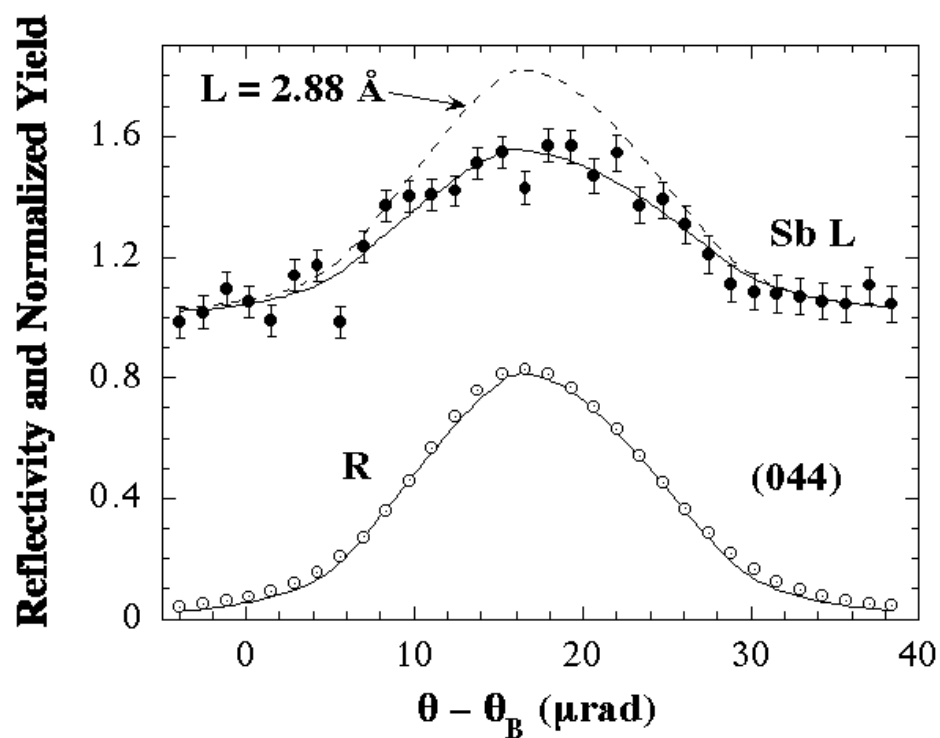


Comparing to Eq. 2.44, Eq. 4.1 has a second cosine term. Therefore, there two unknowns ( $L$  and  $\Delta$ ) in one equation. Without additional in-plane Fourier components, it is impossible to uniquely determine the correct values of these parameters. However, there is a family of solutions which all satisfy Eq. 4.1. One special case is just that reported above, with zero shift and a bond length  $L$  of  $2.75 \pm 0.06 \text{ \AA}$ . If, however, the SEXAFS value of  $L$  ( $2.88 \text{ \AA}$ ) is assumed to be correct, then results of the current study will imply that the Sb dimers must have a midpoint shift of  $0.28 \pm 0.10 \text{ \AA}$ . Additional Fourier components (*e.g.* both (044) and (066)) are needed to uniquely determine whether the Sb ad-dimer is laterally shifted or not. Although it is not possible to conclude on the basis of the present data alone, the symmetric-dimers model (*i.e.*, no shift) is favored in the current study, based on its simplicity and on chemical reasoning.

The discrepancy between our XSW measured Sb-Sb bond length and results from SEXAFS measurement and calculations does not fall into the range of the experimental uncertainty. In the current study, the Sb dimer bond length is determined from the  $f_{022}$  measured value by assuming the Sb thermal vibration is isotropic. Although there is some evidence that the surface thermal vibration amplitudes for both Si clean surface [85] and the relevant As/Si(001) system [49] are isotropic, there is no direct evidence of isotropic thermal vibration on the Sb/Si(001) surface. In fact, if the Sb bond length of  $2.88 \pm 0.04 \text{ \AA}$  measured by SEXAFS is assumed to be the correct value, this would imply an Sb thermal vibrational amplitude of  $0.22 \pm 0.04 \text{ \AA}$  along the [011] direction at room temperature based on our XSW measurements. This is 40% larger than the XSW measured value along the [001] direction. Whether or not there exists such a large anisotropy for the Sb thermal motion at RT will be the focus of future and off-normal higher-order harmonic XSW measurements (*e.g.* using Si (044) and (066) reflections) may resolve this issue.

One more comment on the Sb dimer bond length issue: It is interesting to note that based on Eq. 2.40 the geometrical factor  $a_{044}$  is zero if the Sb dimer bond length is exactly 2.88 Å as measured by SEXAFS. Then the coherent fraction of zero should be measured by the (044) XSW measurement. To test this, a XSW (044) scan was taken on the same surface and the reflectivity and fluorescence curves are shown in Fig. 4.3. It is obvious from Fig. 4.3 that the fluorescence yield curve (dash line) of zero coherent fraction (for Sb dimer bond length of 2.88 Å) does not match the experimental data. The result of a  $\chi^2$  fitting revealed a rather low (0.18) but non-zero coherent fraction. This result, although preliminary, may provide direct evidence for a Sb bond length shorter than 2.88 Å. Also notice that the (044) coherent position of  $P_{044} = 0.27$  does not equal to the twice of the (022) value (0.2) but has a significant discrepancy ( $\sim 0.07$  Å). This could be evidence for the anharmonic thermal vibration mode in the [011] direction. Since the thermal vibration in the [001] direction has not been found to be noticeably anharmonic, this could imply a different behavior for the vibrations along these two orientations. It needs to be pointed out that uncertainties of the high-order harmonic ((008) and (044)) measurements are larger than that of the fundamental ((004) and (022)) XSW measurements. With brighter photon sources such as Advanced Photon Source (APS) and European Synchrotron Radiation Facilities (ESRF), one should be able to perform better quality high-order harmonic XSW measurements and therefore to obtain more thorough information about static surface structures and thermal vibrations.

Figure 4.3 The experimental (dots) and theoretical curves (solid lines) for the x-ray reflectivity and Sb L fluorescence yield for the Si (044) reflection at  $E_{\square} = 8.0$  keV. The coherent fraction and coherent position are determined from a best fit to be  $f_{044} = 0.18 \pm 0.03$  and  $P_{044} = 0.27 \pm 0.04$ . A hypothetical fluorescence yield curve of zero coherent fraction (corresponding to  $L = 2.88$  Å predicted by SEXAFS [102]) is also plotted as a dash line. It can be seen clearly that the zero coherent fraction curve does not agree with the experimental data.



#### 4.4 Summary

On MBE grown saturated (1x2) Sb/Si(001) surfaces, a series of XSW measurements were performed to investigate the adsorption of Sb on Si(001). These studies show that the adsorption of Sb on Si(001) annealed to 550°C results in a highly ordered (ordered fraction  $C = 0.95$ ) and stable dimerized surface which leads to the passivation of the Si(001) surface. This confirms quantitatively the qualitative observations by LEED and STM [91, 101, 102]. The Sb dimer is found to be centered above the hollow site and is  $1.64 \pm 0.02 \text{ \AA}$  above the bulk-extrapolated Si(001) surface. Upon Sb adsorption, the Si(001) (2x1) reconstruction is lifted and the top layer Si atoms is found to be relaxed inward by  $0.10 \pm 0.05 \text{ \AA}$  when combining the XSW results with Richter *et al.*'s SEXAFS results [102]. These results of Sb dimer height and substrate response are in good agreement with other quantitative measurements and theoretical calculations [52, 114].

The Sb dimer bond length is determined to be  $2.75 \pm 0.06 \text{ \AA}$ . This result agrees favorably with the ion channeling result ( $2.8 \text{ \AA}$ ) [52] and the Sb-Sb covalent bond length but is shorter than the results of SEXAFS ( $2.88 \text{ \AA}$ ) [102] and calculations ( $2.93 \text{ \AA}$  [114],  $2.94 \text{ \AA}$  [135]). A preliminary (044) XSW study also indicates that the SEXAFS and theory proposed Sb dimer bond length are too long.

Finally, the RT Sb thermal vibration amplitude along [001] direction is obtained experimentally to be  $0.156 \pm 0.01 \text{ \AA}$  by employing [004] and [008] XSW measurements for the first time. The anharmonicity and isotropy of the Sb thermal vibration mode have also been speculated.

## Chapter V Bi/Si(001) Surface: (1x2) and (2x2) Phases

### 5.1 (1x2) Bi/Si(001) Saturated Surface and Low Coverage (2x2) Bi/Si(001) Surface

Bismuth (Bi) is the heaviest element in group V. In contrast to other group V elements As and Sb, relatively less attention had been focused on the Bi adsorption on Si(001) until two interesting features associated with Bi were discovered recently. First, Bi was recently found to be a better surfactant for the MBE growth of Ge/Si heterostructures [107]. Second, Bi adsorption on the Si(001) surface has recently been of great scientific interest since two distinct local structures ((1x2) phase for an annealed saturated surface and (2x2) phase for an "as-deposited" low-coverage surface) were observed at different conditions by STM [92]. The (2x2) phase has never been reported for any group V adsorption on Si(001) before.

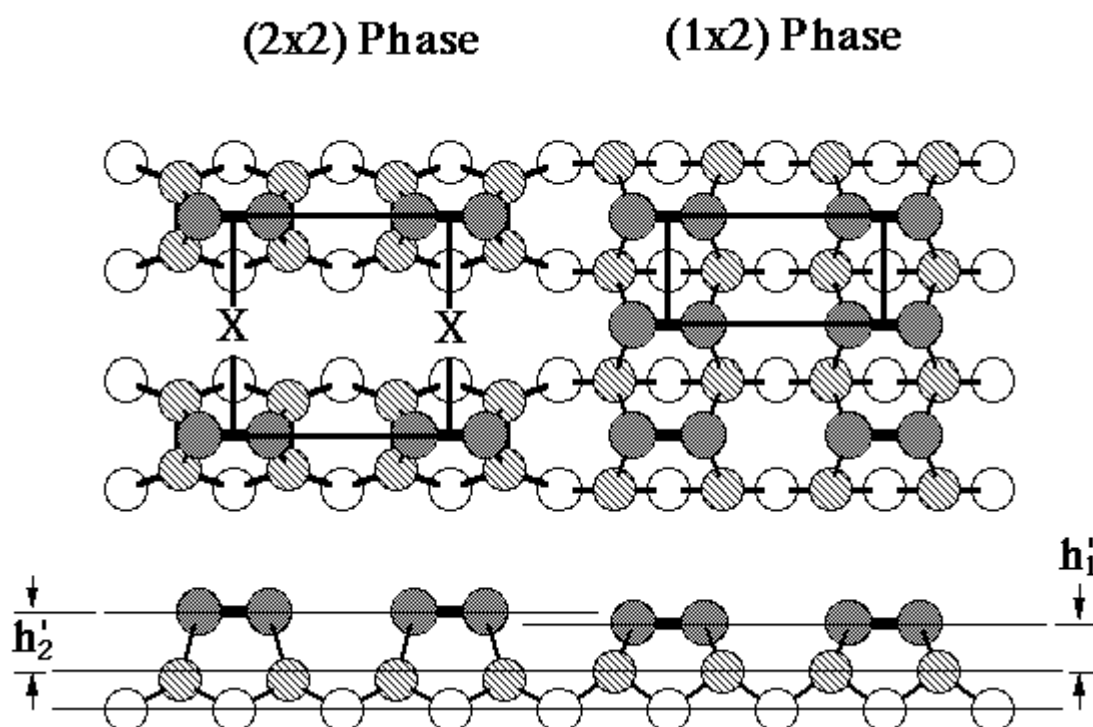
Early experiments using LEED, AES and RHEED [55, 46] observed ( $n \times 2$ ) patterns with  $n$  ranging from 5 to 13 for the Bi/Si(001) surface for Bi coverages below 1 ML at elevated temperatures (from 200°C to 500°C). To explain the observation, a missing row dimer model was proposed. The model assumed that Bi forms dimerized adlayers on the unreconstructed Si(001) surface. The Bi dimer rows are arranged in a way that for every  $n$  rows of dimer there is one Bi dimer row missing to relieve the surface strain due to the large size mismatch between Bi and Si. This results the final Bi coverage to be  $(1 - 1/n)$  ML. The local structure consists of Bi dimers

arranged with a (1×2)-like local geometry, similar to the Si(001) clean surface or other group V (As, Sb) adsorption on Si(001). This missing dimer row structure was later confirmed by Park *et al.*'s STM results [95]. The structure and stability of the Bi (1×2) phase has been calculated by Tang and Freeman using a first-principles cluster method [116]. They predicted that Bi forms a stable dimerized adlayer by removing the underlying Si (2×1) reconstruction at 1 ML coverage, similar to the case of As or Sb adsorption. In a previous XSW study by Franklin *et al.* [50], the structure for the (1×2) Bi phase was precisely measured and the Bi dimer height and bond length agreed with Tang and Freeman's predicted values.

The other local structure, the (2×2) Bi phase, was first observed for Bi adsorption on Si(001) at room temperature (RT) by a recent STM and LEED study [92]. STM images show a local Bi structure with a (2×2) periodicity for surfaces with Bi coverage below 1/2 ML. They speculated that the underlying Si (2×1) still remained upon Bi adsorption. In the same calculation mentioned above, Tang and Freeman also calculated the stable structure for the low coverage Bi/Si(001) surface [116]. As shown in Fig. 5.1 their calculation predicts that a (2×2) phase occurs as a stable phase at low coverage (below 0.5 ML) where Bi forms ad-dimers on top of the Si dimerized surface. The Bi dimers are centered on top of the pedestal site and aligned perpendicular to the underlying Si dimers. At higher coverages, the theory predicts that the Si (2×1) reconstruction is removed as mentioned previously. The calculation predicted heights for the (1×2) and (2×2) phase Bi dimers are 1.80 Å and 2.10 Å above the bulk-extrapolated Si(001) surface layer (Fig. 5.1). However, there is a lack of experimental quantitative information for the (2×2) phase to confirm the calculation and qualitative findings of STM.

Evidently, two different adsorption phases exist for the Bi/Si(001) surface. One would ask: Are these two phases both stable? Do they coexist? Under what surface

Figure 5.1 Top view and side view of the (2x2) (left side) and (1x2) (right side) Bi phases on the Si(001) surface proposed by Tang and Freeman [116]. The open circles are bulk Si atoms, the hatched circles are top layer Si atoms and the dark circles are Bi atoms.  $h_1$  and  $h_2$  are the height of the (1x2) and (2x2) phase Bi dimers above the Si(004) bulk-extrapolated lattice planes.



condition (substrate temperature, coverage, etc.) do they exist? Is there a phase transition between these two phases? If there is such a phase transition, what is the kinetics and mechanism of this phase transition? What can one learn from investigating these phases, phase transitions and surface kinetics?

Understanding the kinetics of adsorption on crystalline surfaces at the atomic scale is important for thin film growth, catalysis, and corrosion. The most common tool used to study surface kinetics and thermodynamics has been STM, since it is a very powerful versatile high-resolution real-space imaging technique [71]. Although STM can provide valuable real-space information that can be used as an initial guess for surface structural models, certain disadvantages of STM, such as tip-surface interactions, which can affect the kinetics of observed processes, along with STM's insensitivity to chemical composition and disordered phases, limit the conclusions one can draw from STM measurements. Furthermore, as a strictly local probe, STM must rely on accurate and comprehensive observation of the transformation to be able to correctly describe the statistics of (and thereby to infer the thermodynamics of) a transition. On the other hand, statistical averaging is inherent to diffraction-based techniques, such as LEED and surface XRD. However, these global probes require the presence of significant long-range order in (at least one of) the adsorbate phases under observation to characterize any transformations. This chapter will demonstrate how XSW can overcome the above limitations of STM and diffraction and complement these techniques in studying surface kinetics.

One of the goals of this thesis is to quantify the structure of the Bi/Si(001) (2x2) phase and the surface reaction kinetics for the thermally activated phase transition between the (2x2) and (1x2) phases. The current study tries to demonstrate the XSW method as a new experimental approach for investigating surface kinetics of adsorption

on crystalline surfaces. The XSW method is ideally suited for studying a surface reaction of this type since it is extremely sensitive in distinguishing between the two distinct heights for the Bi dimers ( $h_{\text{Bi}}^{\text{I}} - h_{\text{Bi}}^{\text{II}} = 0.3 \text{ \AA}$  predicted by theory) of the two phases illustrated in Fig. 5.1. In the current study, the structure and thermal vibration of the (1x2) phase saturated Bi/Si(001) surface was first characterized by XSW to confirm previous findings on this surface and to obtain information required to study the (2x2) phase and surface kinetics. Then low coverage Bi/Si(001) surfaces were prepared at RT. Further analysis shows that there were two ordered phases of Bi coexisting at the surface, as well as a certain fraction of "disordered" Bi. The surface was annealed at successively higher temperatures with an XSW measurement following each annealing. From this isochronal annealing measurement, compositions of each phase were estimated at each annealing temperature. The results clearly indicated that the (2x2) and disordered Bi phases are only metastable phases that undergo a thermally activated irreversible phase transition to the stable (1x2) Bi phase. The activation energy and exponential prefactor for the thermally activated, irreversible (2x2)-to-(1x2) phase transition is also determined experimentally.

## 5.2 *Experimental*

### 5.2.1 *Surface preparation*

#### (a) *Saturated surface*

A clean Si(001) sample was used as a substrate to grow a saturated Bi/Si(001) surface. With the sample held at 500° C, Bi was deposited from an effusion cell held at

500°C, resulting in a Bi flux of 0.2 ML / min at the sample surface according to the thickness monitor. The total evaporation time was over 10 minutes and a total amount of 2 ML of Bi was evaporated onto the sample. The sticking coefficient for Bi adsorption, like that of other group V elements on Si(001) [110], goes to zero at coverages greater than 1 ML for this temperature [55]. Therefore, approximately 1 ML Bi was adsorbed on the surface. The Bi-saturated surface was further annealed for 10 minutes at 500°C to desorb excess Bi and to arrive at the saturation coverage estimated to be about 0.8 ML [50, 95]. After cooling to RT, a two domain (1×2) LEED pattern with slightly diffused half-order spots was observed. No clear  $n$ th order spots were observed.

*(b) Low coverage surface*

Low coverage (< 0.5 ML) Bi/Si(001) surface was prepared by evaporating Bi onto the Si surface held at RT. In the vapor out of the Knudsen cell held at 500°C, Bi are monomers-dimers with the ratio of dimers to monomers of 30%:70% [65], therefore there are approximately equal amount of Bi as monomers and dimers. The Bi coverage is calibrated by the thickness monitor and by the Bi Auger peak ratio relative to the saturated coverage (~0.8 ML). The LEED pattern was still 2-domain (1×2) after deposition but fainter than that of the clean surface, similar to the saturated surface. The (2×2) LEED pattern reported by previous experiments [92] were not observed here.

*5.2.2 XSW measurements*

*(a) Saturated surface*

On the saturated (1x2) Bi/Si(001) surface the combination of (004) and (008) XSW measurements was undertaken to characterize the structure of the (1x2) phase and thermal vibration of Bi dimers. 15 keV x-rays was used for both the (004) and (008) measurements, produced by reflection by the (004) or (008) diffraction planes of the monochromator crystal, respectively. This incident photon energy is above the Bi L<sub>3</sub> edge but below the L<sub>2</sub> edge, and the resultant Bi L<sub>23</sub> fluorescence yield was detected by the Si(Li) detector. Figure 5.2(a) shows the Si reflectivity and Bi L<sub>23</sub> fluorescence yield (normalized to unity at off-Bragg angles) as a function of the Bragg reflection angle  $\theta$  for the (004) reflection (diffraction vector normal to the sample surface). A similar scan (Fig. 5.2 (b)) was acquired for the same surface using the (008) reflection.

*(b) Low coverage surface*

The "as-deposited" 0.2 ML Bi/Si(001) surface was transferred to the x-ray chamber after LEED and AES characterization and an XSW measurement using the Si(004) reflection was performed. The incident photon energy was tuned to be  $E_{\theta} = 13.7$  keV, above the Bi L<sub>3</sub> edge but below the L<sub>2</sub> edge, resulting in a Bi L<sub>23</sub> fluorescence yield. After the "as-deposited" XSW measurement at RT, the sample was annealed for 20 minutes at successively higher temperatures and then cooled down to RT for each subsequent XSW measurement. The temperature range of this isochronal annealing study was limited by Bi desorption, which started above 720 K. Figure 5.3 illustrates the angular dependence of the Si (004) reflectivity and the series of Bi L<sub>23</sub> fluorescence yield

Figure 5.2 The experimental and theoretical angular dependence for the x-ray reflectivity and Bi L fluorescence yield for (a) the (004) reflection at  $E_{\square} = 15$  keV. (b) the (008) reflection at  $E_{\square} = 15$  keV. This is for the 0.8 ML (1x2) Bi/Si(001) surface.

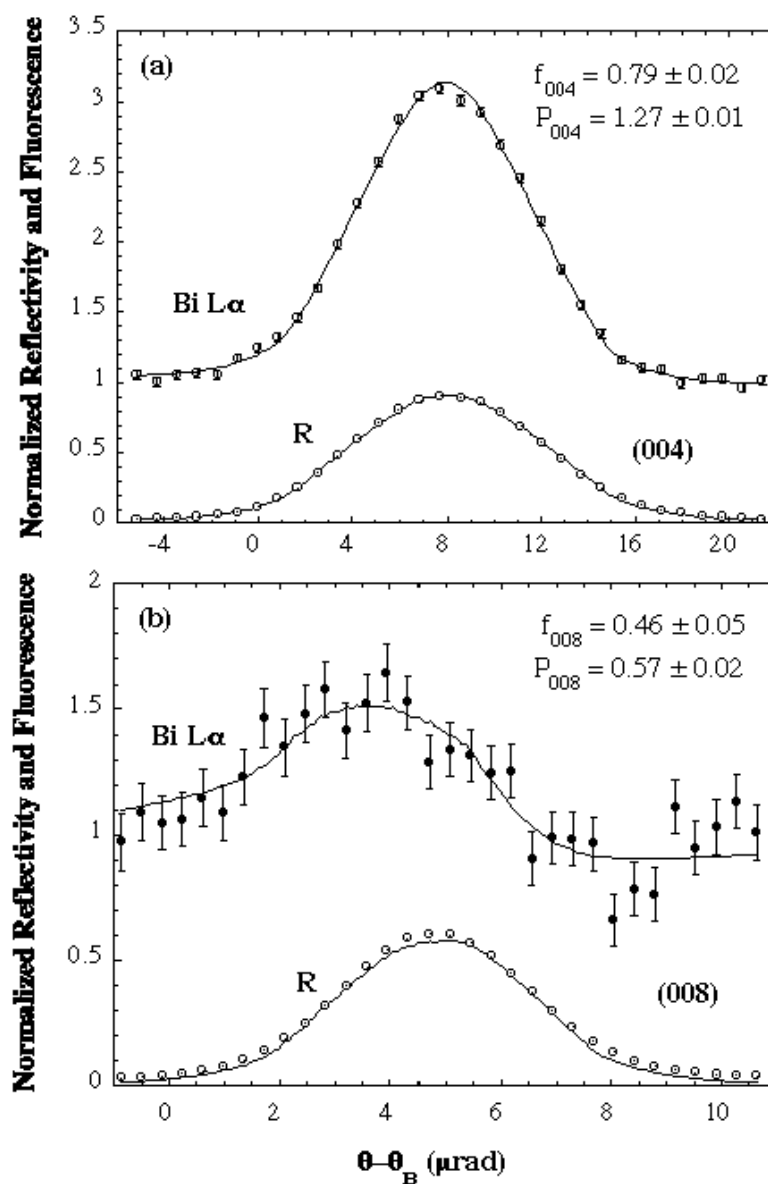
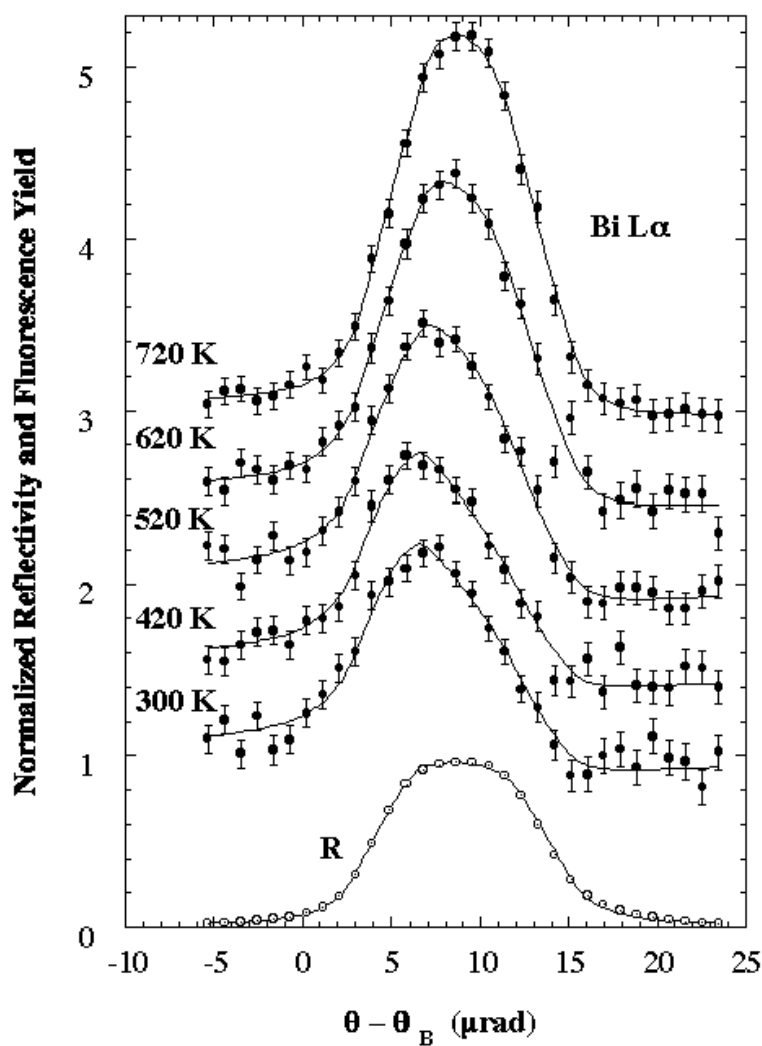


Figure 5.3 A series of experimental data and best fits to x-ray dynamical diffraction theory (solid lines) for the Si (004) reflectivity and normalized Bi L $\alpha$  fluorescence yield as a function of the incident angle  $\theta$  for RT (004) measurements after various annealing temperatures. The curves are offset for clarity. This isochronal annealing study started by depositing 0.2 ML of Bi on Si(001) at RT.



data (circles) and the best fit to the dynamical diffraction theory (Eq. 2.36) (smooth curves).

### 5.3 Results and Discussion

#### 5.3.1 (1x2) phase saturated surface: structure and thermal vibration

The coherent fractions ( $f_{004}$ ,  $f_{008}$ ) and coherent positions ( $P_{004}$ ,  $P_{008}$ ) shown in Fig. 5.2(a) and (b) are determined by  $\chi^2$  fits of Eq. 2.36 to the Bi L $\alpha$  fluorescence data. The measured value of  $P_{004} = 1.27 \pm 0.01$  indicates that the Bi ad-dimer height  $h' = P_{004} d_{004} = 1.72 \pm 0.02$  Å above the Si(004) bulk-like diffraction planes. This result agrees perfectly with the previous XSW measurement by Franklin *et al.* [50]. This height calculated by the DMol calculation [116] is 1.80 Å and agrees reasonably well with XSW measurements.

The coherent fractions can immediately be used in Eq. 2.50 to determine the degree of disorder present in the Bi atom population. Given the results of  $f_{004} = 0.79 \pm 0.02$  and  $f_{008} = 0.46 \pm 0.05$ , the ordered fraction  $C$  is found to be a reasonably high  $0.95 \pm 0.05$ . High ordered fractions have also been found for other group V adsorbates (As: 100% Ref. [49] and Sb: 95% [99]) on Si(001). This experimental determination of the Bi order is consistent with the calculated prediction [116] of high stability of the (1x2) phase. It also provides quantitative confirmation of STM reports of highly ordered Bi, with a small, but finite, defect concentration [95]. It should be kept in mind, however, that STM and XSW have different sensitivities to different types of disorder. XSW measurements report the fraction of Bi atoms residing in sites with a particular

registration. It is nearly insensitive to the presence of vacancies, which are evident in STM.

Using Eq. 2.48, the value for the RT root-mean-squared vibrational amplitude along the [001] direction  $\sqrt{\langle u_{001}^2 \rangle}$  is determined to be  $0.13 \pm 0.015 \text{ \AA}$ . The RT (004) Debye-Waller factor is 0.83. Chapter VII will compare and discuss the thermal vibration amplitude measured directly or indirectly by various techniques and calculated by different theories for various related surfaces. This directly determined value will be used in determining phase compositions during the investigation of the low coverage (2x2) phase.

The measured value of  $P_{008}$  is  $0.57 \pm 0.02$ . This value is approximately equal to twice the  $P_{004}$  value (0.54). The slight difference ( $0.02 \text{ \AA}$ ) between the (004) and (008) measured mean positions is within the uncertainty of the XSW measurements. According to Eq. 2.49, this indicates that the Bi time-averaged distribution in the [001] direction is not noticeably asymmetric (*i.e.* the [001] thermal vibration mode of Bi adatoms at RT appears to be harmonic at a  $0.02 \text{ \AA}$  resolution).

### 5.3.2 The low coverage (2x2) phase

Figure 5.3 illustrates a series of XSW scans following each isochronal annealing on the 0.2 ML Bi/Si(001) surface. For clarity, each fluorescence curve is offset by unity relative to the previous one. The modulations in the Bi fluorescence yields as a function of angle in Fig. 5.3 are due to the inward phase shift of the XSW relative to the (004) diffraction planes. Two important features are evident in the raw data by inspection. First, the Bi modulation amplitude (or coherent fraction) shows a definite increase with annealing temperature. This is consistent with the Bi atom population tending toward a

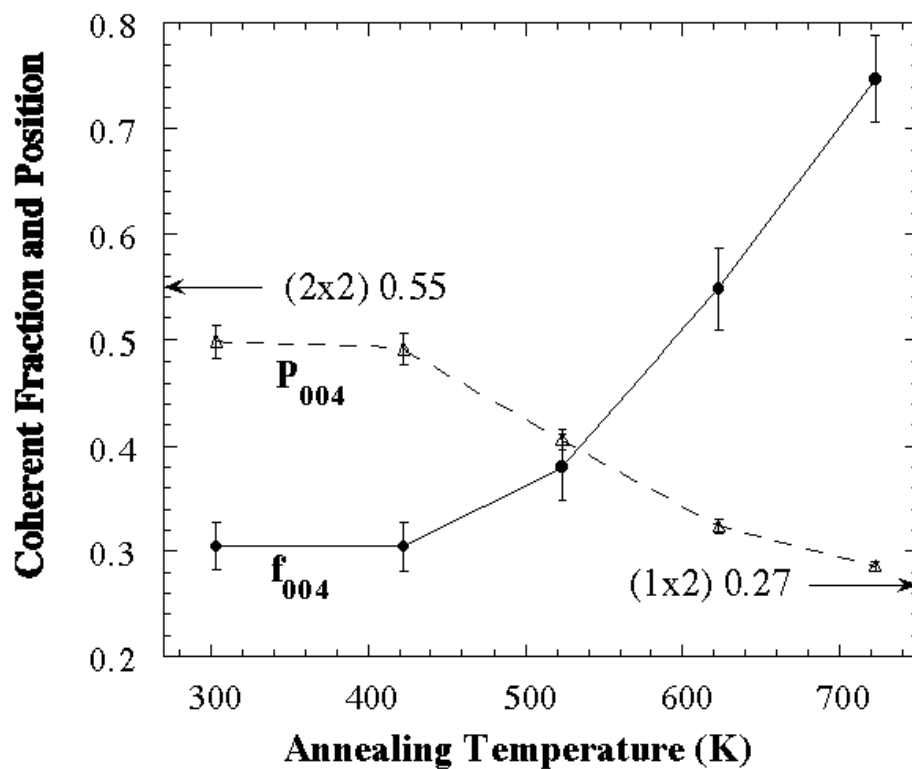
single adsorption height. Second, the position of the maximum in the Bi yield curve moves toward the high angle side as the surface is annealed to higher temperatures, indicating that the average Bi position is moving inward. Referring to Fig. 5.1, one can show that this is the signature for a phase transition from (2x2) to (1x2).

From the best fit to the data in Fig. 5.3, the coherent fraction  $f_{004}$ , the coherent position  $P_{004}$  and the off-Bragg fluorescence yield  $Y_{OB}$  are determined (listed in Table 5.1). Figure 5.4 illustrates the measured coherent fraction and position as a function of annealing temperatures. At the high temperature end, a high coherent fraction of 0.75 and a coherent position of 0.29 were measured. This shows that the surface is highly ordered after annealing to 720-770 K. The fact that the coherent position is approaching the value of 0.27 (or 1.27) found for the (1x2) phase by the previous XSW measurements (Ref. [50] and current study, section 5.3.1) indicates that the surface is approaching the stable (1x2) phase after annealing. At the low temperature end, the coherent fraction is rather low (0.3) and the coherent position (0.50) is quite different from the value of the (1x2) phase. This indicates the existence of another ordered phase, namely the (2x2) phase. The coexistence of the (2x2) phase with the (1x2) phase is evidenced by two observables. First, the measured value 0.50 of the coherent position does not quite reach the theory [116] predicted value of 0.55, but falls in between that value and that of the (1x2) phase. The second evidence is the rather low coherent fraction, which is partially attributable to the two occupied Bi heights causing a reduction in the geometrical factor  $a_{004}$ . The other cause for a lower coherent fraction at lower annealing temperatures is the presence of disordered Bi.

Table 5.1 XSW measured parameters and estimated phase compositions for various annealing temperatures (T).  $Y_{OB}$  is the off-Bragg Bi fluorescence yield,  $f_{c,004}$  and  $P_{004}$  are the measured coherent fraction and coherent position. Phase compositions,  $C_{disord}$  for the disordered phase,  $C_{1 \times 2}$  for the (1x2) phase, and  $C_{2 \times 2}$  for the (2x2) phase, are determined from Eq. 5.1.

T(K) ( $\pm 20$ )	300	420	520	620	720
$Y_{OB}$ (cps) ( $\pm 0.02$ )	1.52	1.48	1.46	1.50	1.54
$f_{c,004}$	$0.31 \pm 0.02$	$0.31 \pm 0.02$	$0.38 \pm 0.03$	$0.55 \pm 0.04$	$0.75 \pm 0.04$
$P_{004}$ ( $\pm 0.01$ )	0.50	0.49	0.41	0.32	0.29
$C_{1 \times 2}$	$0.11 \pm 0.03$	$0.13 \pm 0.03$	$0.36 \pm 0.03$	$0.66 \pm 0.05$	$0.91 \pm 0.06$
$C_{2 \times 2}$	$0.37 \pm 0.03$	$0.36 \pm 0.03$	$0.34 \pm 0.03$	$0.20 \pm 0.03$	$0.06 \pm 0.02$
$C_{disord}$	$0.52 \pm 0.04$	$0.51 \pm 0.04$	$0.30 \pm 0.05$	$0.14 \pm 0.05$	$0.03 \pm 0.02$

Figure 5.4 Measured XSW (004) coherent fraction and coherent position as a function of annealing temperatures. Indicated in the figure by arrows are the XSW measured coherent position (0.27) for the (1x2) phase and the theory (Ref. [116]) predicted coherent position (0.55) for the (2x2) phase.



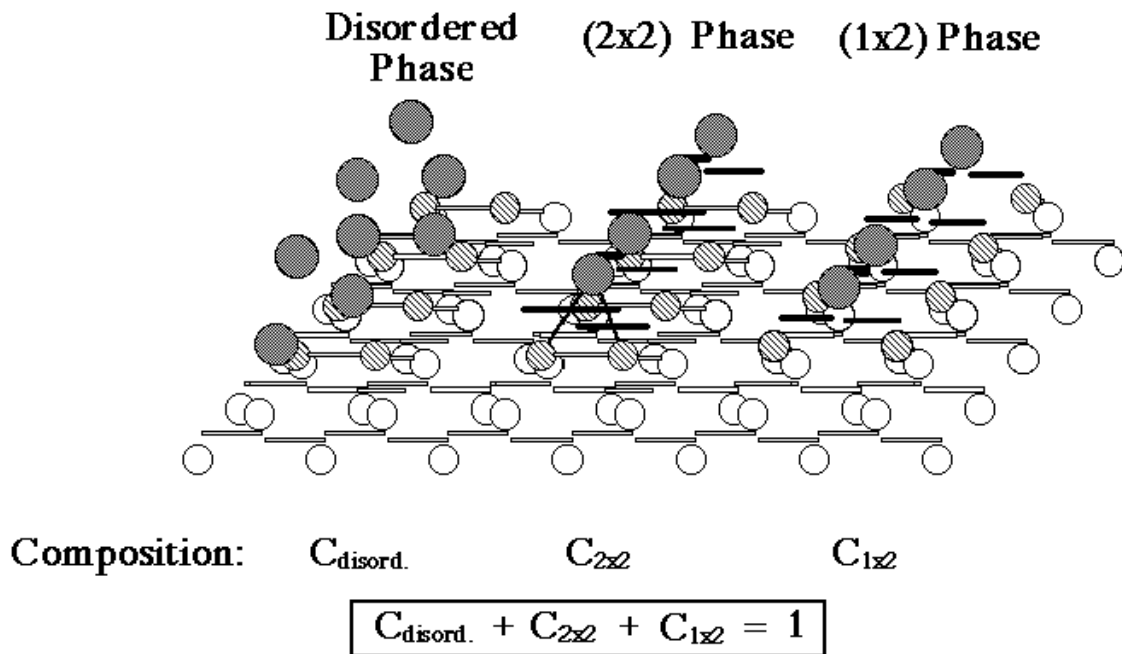
Based on the XSW experimental results of current study and on theoretical calculations [116] for the Bi/Si(001) surface, the compositions of the two ordered phases as well as the disordered phase can be determined by following. As shown in Figure 5.5, the Bi ad-atoms form symmetric dimers on the surface for the two ordered phases and the heights of the Bi ad-dimer relative to the Si(004) bulk-extrapolated surface are  $h_{\square}^1$  for the (1x2) phase and  $h_{\square}^2$  for the (2x2) phase. If the compositions of these two ordered Bi phases are denoted  $C_{1x2}$  and  $C_{2x2}$ , according to Eq. 2.34, the resultant (004) Fourier component for the Bi ad-atom's spatial distribution can be written as:

$$f_{004} \cdot \exp(2\pi i P_{004}) = D_{004} \cdot [C_{1x2} \cdot \exp(2\pi i P_1) + C_{2x2} \cdot \exp(2\pi i P_2)] \quad , \quad (5.1)$$

where  $P_1 = h_{\square}^1 / d_{004}$ , and  $P_2 = h_{\square}^2 / d_{004}$ , are the Bi fractional positions relative to the Si(004) diffraction planes, and  $f_{004}$  and  $P_{004}$  are the experimental observables. For the (1x2) phase, the value of  $P_1$  was determined to be 0.27 in current study (See section 5.3.1). For the (2x2) phase, the value of  $P_2$  is based on the theory [116] predicted value of 0.55 since there is no direct measurement for the Bi dimer height. As described in Section 5.3.1, the RT (004) Debye-Waller factor for the (1x2) phase was directly measured to be  $D_{004} = 0.83$ . We will assume that  $D_{004} = 0.83$  for the (2x2) phase as well. The determined compositions of the three phases by Eq. 5.1 are listed in Table 5.1 and plotted in Figure 5.6 as a function of the annealing temperature.

It is clear from Fig. 5.6 that on the "as-deposited" 0.2 ML Bi/Si(001) surface 50% (~0.1 ML) of Bi ad-atoms forms the disordered phase. It is interesting to note that the disordered fraction  $(1-C) = 0.5$  of the initially deposited Bi is roughly equivalent to the fraction of Bi monomers in vapor phase (~ 0.7). The structure of the disordered phase is unknown from XSW measurements. It may consist of both Bi monomers adsorbed

Figure 5.5 The structural model for deriving phase compositions ( $C_{\text{disord}}$  for the disordered phase,  $C_{1 \times 2}$  for the  $(1 \times 2)$  phase, and  $C_{2 \times 2}$  for the  $(2 \times 2)$  phase). The Bi dimers in the  $(1 \times 2)$  and  $(2 \times 2)$  phases have coherent positions of  $P_1 = h'_1 / d_{004}$ , and  $P_2 = h'_2 / d_{004}$ , respectively. The Bi in the disordered phase is randomly distributed and does not contribute to the Fourier component.

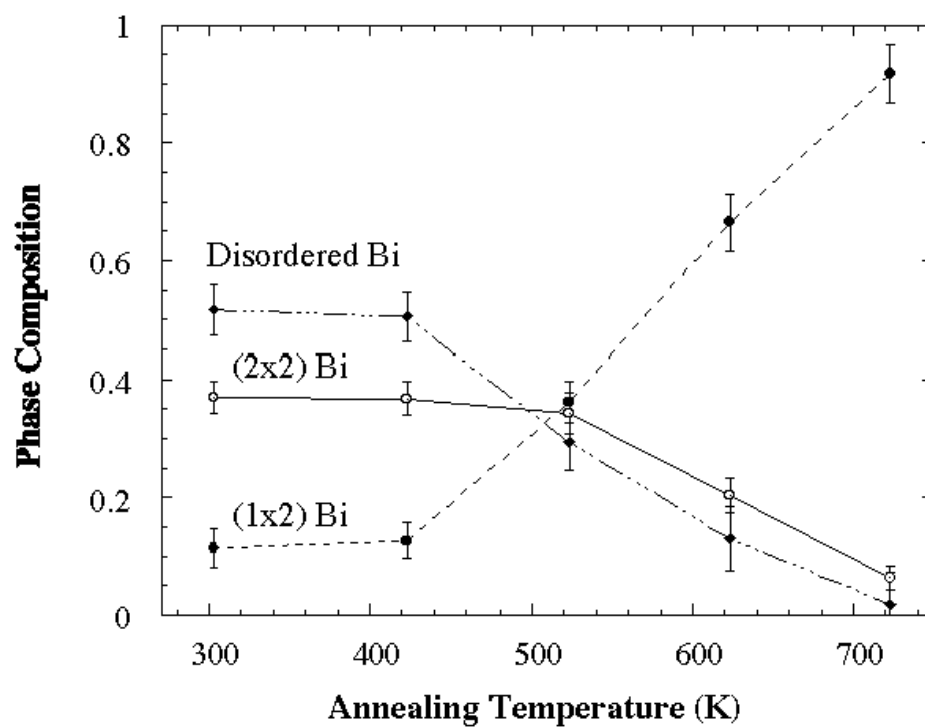


**(004) Fourier Component:**

$$\underline{f_{004} \cdot e^{2\pi i P_{004}} = [C_{2 \times 2} \cdot e^{2\pi i (h'_2 / d_{004})} + C_{1 \times 2} \cdot e^{2\pi i (h'_1 / d_{004})}] \cdot D_{004}}$$

Figure 5.6 Derived phase compositions of Bi as a function of annealing temperatures.

The lines are drawn to guide the eye.



(either chemisorbed or physisorbed) at various sites (such as step edges, surface defects, etc.) and 3-dimensional Bi clusters. The nature of the disordered phase should be further explored in the future investigations.

For the remaining Bi, 35% (~0.07 ML) forms the (2x2) phase and 15% (~0.03 ML) of Bi forms the (1x2) phase. Since there is only 0.07 ML of the (2x2) phase and these (2x2) phase dimers may not have long range ordering, this explains why the (2x2) LEED pattern was not observed from this surface.

Below 420 K, the population of the three phases remained unchanged. After annealing to 520 K, 50% of the disordered Bi and 10% of the (2x2) phase were converted into the (1x2) phase. The conversion of the disordered Bi started at a temperature between 420 K and 520 K while the conversion of the (2x2) phase started at about 520 K. It is clear that, even at this low coverage of 0.2 ML, the (2x2) phase is not stable as predicted [116], but is instead a metastable phase. The disordered Bi is also a metastable phase. For annealing temperatures up to 720 K, the off-Bragg Bi fluorescence yield  $Y_{OB}$  remained constant, indicating that the total Bi coverage did not change (*i.e.*, no Bi desorption occurred).

#### 5.4 Summary

In summary, the surface structure and kinetics of the Bi adsorption on Si(001) has been investigated by x-ray standing waves. On the (1x2) saturated surface, Bi is found to form a stable and well-ordered dimerized adlayer on the (1x1) unreconstructed Si(001) surface, similar to As and Sb. The Bi dimer is found to be located 1.72 Å above the ideal Si surface and this agrees very well with the previous experiment [50] and theory [116]. The current study also measures the RT [001] thermal vibration amplitude of Bi on

Si(001) to be 0.13 Å. On a 0.2 ML Bi/Si(001) surface, the surface structure and kinetics of the thermally activated irreversible phase transition as a function of annealing temperature has been investigated using XSW measurements. The current study confirms the existence of a Bi (2x2) phase that was originally proposed by an STM study [92] and predicted by a first-principles total-energy calculation [116]. Our study shows that this (2x2) phase along with the disordered phase is metastable. This high-precision, quantitative experiment demonstrates a new approach for investigating the surface kinetics of adatom adsorption on crystalline surfaces.

## Chapter VI The Ga/Si(001) Surface

### 6.1 The Ga/Si(001) surface: Orthogonal or parallel ad-dimer?

In comparison to group V, the adsorption of group III metals on (2x1) Si(001) induces different and more complicated surface reconstructions. For example, Al adsorption is reported to induce (2x2), (2x3), (4x5), (1x7) and c(4x12) reconstructions on the Si(001) surface [58, 90]. The adsorption of In on Si(001) forms (2x2), (3x4), (2x1) and (1x1) reconstructions [7, 66, 70]. These reconstructions are coverage dependent.

The Ga/Si(001) surface has drawn the most attention among the group III elements since its scientific importance as a prototype for group III metal adsorption on Si(001) and its implication on technologically important issues such as GaAs heteroepitaxial growth on Si(001). Early experiments using RHEED [106], LEED and AES [22, 23] reported five different phases for the submonolayer Ga/Si(001) surface. These five phases are: (2x3) phase at Ga coverage of 0.15-0.35 ML, (2x5) at 0.4 ML, (2x2) at 0.4-0.55 ML, (1x8) at 0.7-0.9 ML, and (1x2) at 1 ML. Based on their observations, Bourguignon *et al.* proposed an orthogonal ad-dimer model [22] for these phases except (1x8) (The (1x8) phase is considered as an incommensurate phase.). For the (2x3), (2x5) and (2x2) phases, the orthogonal ad-dimer model assumes the same local structure on the surface (Fig. 6.1). Ga grows as ad-dimers on top of the Si (2x1) reconstructed surface and Ga ad-dimers are centered at the valley bridge site with the orientation of the Ga dimer bond perpendicular to the underlying Si dimer bond. The

spacing of these Ga ad-dimer rows can be arranged to form (2x3), (2x5), and (2x2) phases at coverages of 1/3, 2/5 and 1/2 ML Ga, respectively (Fig. 6.1). Bourguignon *et al.* also proposed that the underlying Si reconstruction begins to be lifted when more than 0.5 ML of Ga is adsorbed on the surface, and, at Ga coverage of 1 ML, the Si (2x1) reconstruction is completely removed (Fig. 6.1).

The growth mode in the Ga/Si(001) system was also investigated by Bourguignon *et al.* in the same experiments [22, 23]. It was found that the growth mode is drastically affected by the substrate temperature. The Ga grows layer-by-layer at room temperature but islands start forming at different coverages depending on substrate temperature. For example, at 1 ML, islands start forming at 330°C.

In subsequent STM studies [6, 88, 89] the (2x3) and (2x2) Ga/Si(001) structures were observed for Ga coverages below 0.5 ML. These STM images show that the Ga ad-dimers are located between the Si dimer rows and that these Ga ad-dimers grow in rows which are perpendicular to the underlying Si dimer rows. The incommensurate phase, (1x8) (or (nx8)) was also observed by STM for Ga coverages above 0.5 ML [6]. However, there were no reported STM observations of the (2x5) and (1x2) phases.

The resolution of the above-mentioned STM measurements was not sufficient to distinguish either single Ga atoms within a Ga ad-dimer or the orientation of an ad-dimer. The Ga ad-dimers looked like rounded circles rather than elongated ellipsoids on these STM images. Therefore, besides the orthogonal ad-dimer model, the parallel ad-dimer model (Fig. 6.2) can also be considered consistent with the STM images and the LEED patterns. This was posed as an alternative solution for the (2x2) Al/Si(001) surface [90]. Although the two models differ in the relative orientations of the Ga and Si dimers, both

Figure 6.1 Top view of the structural model (orthogonal ad-dimer) for (2x2), (2x3), (2x5) and (1x2) phases on the Ga/Si(001) surface by Bourguignon *et al.* [22].

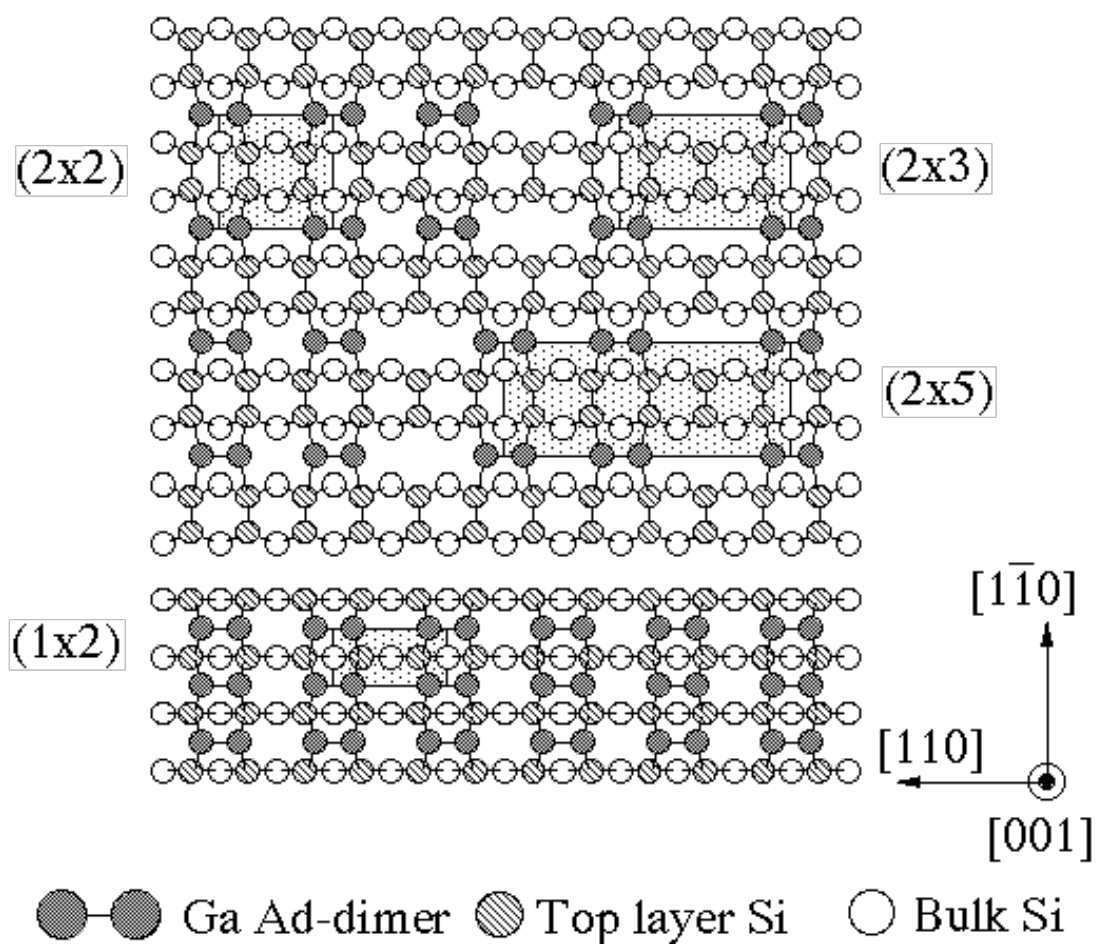
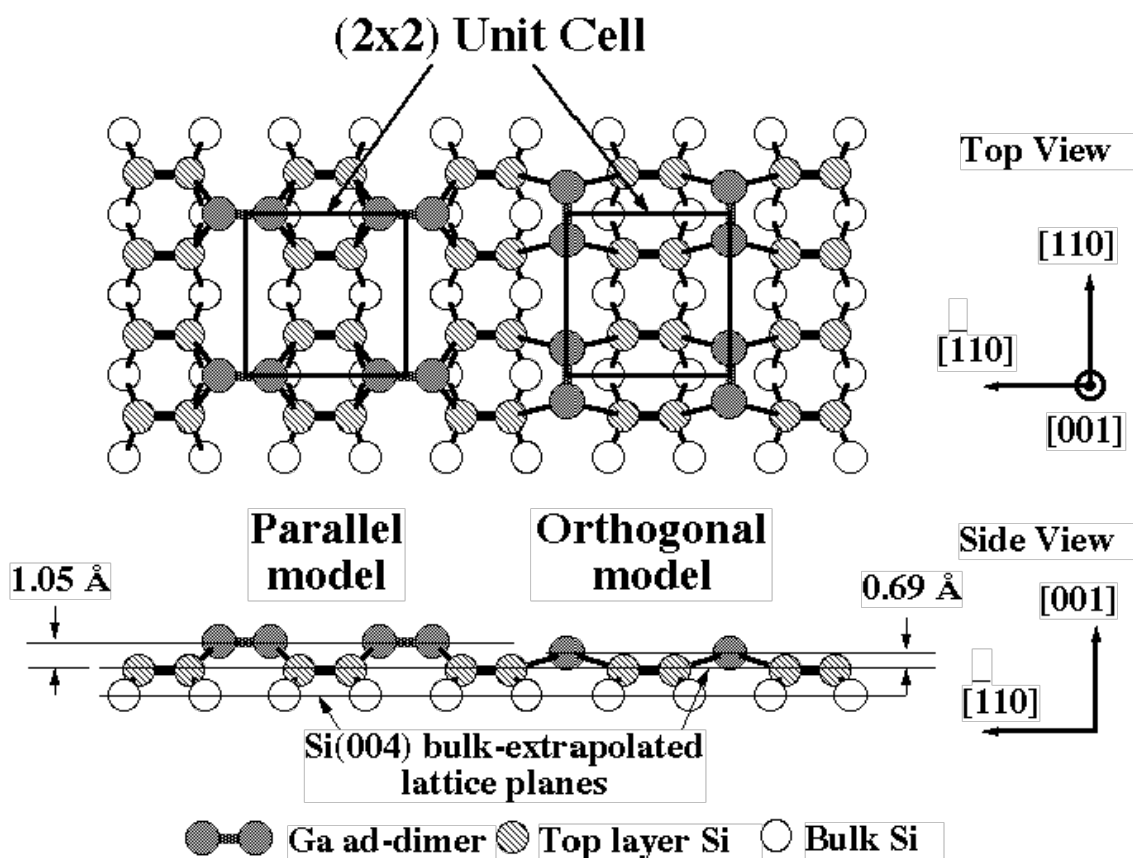


Figure 6.2 A top view and a side view of the parallel and orthogonal ad-dimer models for the (2x2) Ga/Si(001) surface structure. The ad-dimer heights above the Si(001) ideal surface shown in this figure are those predicted by the DMol cluster calculations [97, 117].



models have a local (2x2) symmetry and have the Ga ad-dimer located between Si dimer rows at the valley bridge site.

The orthogonal and parallel ad-dimer models were first tested by Northrup and co-workers [93] with first-principles total-energy pseudopotential calculations for Al, Ga, and In on Si(001). For coverages below 0.5 ML, their results strongly favor the parallel model over the orthogonal model. Recently a first-principles DMol calculation by our collaborators Tang and Freeman [97, 117] for the low coverage Ga/Si(001) surface further confirms this, showing that a parallel ad-dimer has much lower energy than an orthogonal ad-dimer. Parallel ad-dimers on Si(001) was never reported experimentally before the XSW measurements were performed in this thesis research [97, 117]. Therefore, there is a debate on whether the Ga ad-dimer is orthogonal or parallel on Si(001). While the orthogonal model is supported by LEED, STM measurements, the parallel model is favored by theory.

Two recent measurements favor the parallel model. An impact-collision ion-scattering spectrometry experiment showed strong (though indirect) evidence of parallel ad-dimers on a vicinal In/Si(001) surface [111]. An STM study of the related (2x2) Al/Si(001) system, Itoh *et al.*, obtained atomic resolution images, which showed that Al forms parallel ad-dimers on Si(001) at low coverage [60]. Prior to the current study, there was still a lack of direct experimental evidence of the parallel ad-dimer for Ga/Si(001) surface.

From DMol calculations [97, 117] the Ga ad-dimer height above the ideal Si(001) surface for the parallel model is 0.36 Å higher than the orthogonal dimer (Fig. 6.2). Although this slight difference may be beyond the resolution of most other techniques, the XSW method is ideally suited for this type of measurement since it is extremely sensitive to the ad-atom's height. In the current study, our main effort focuses on solving

the controversy of the Ga ad-dimer orientation on the Si(001) surface. Employing the XSW probe, the Ga ad-dimer height above the ideal Si(001) surface was measured with high precision. Combining the XSW results with theory predictions in a collaboration with Tang and Freeman at Northwestern University, the parallel model is experimentally confirmed and the orthogonal model is clearly ruled out. The surface structure and its coverage dependence, surface stability and thermal vibration are also investigated.

## *6.2 Experimental*

### *6.2.1 Surface Preparation*

To prepare a Ga/Si(001) surface, Ga was evaporated from a Knudsen cell held at 830°C with the LN<sub>2</sub> cryoshroud running to maintain a good vacuum. The Ga deposition rate was approximately 0.25 ML/min. The Si sample was held at room temperature during deposition. For  $\Gamma_{\text{Ga}} < 1 \text{ ML}$ , the Ga coverage was calibrated to be directly proportional to the exposure time, with a relative error of 10%. This calibration was made by using the ratio of the Ga to Si Auger peaks, and by comparison of the X-ray fluorescence yield to an ion-implanted standard Si sample with a Ga areal density calibrated by Rutherford backscattering (RBS). The Ga/Si(001) surfaces with various Ga coverages ( $\Gamma_{\text{Ga}}$ ) ranging from 0.3 to 1 ML were prepared. Only (2x2) LEED patterns were observed for all investigated surfaces. The brightest (2x2) pattern was observed at lower coverages (0.3 to 0.35 ML). The (2x2) pattern became fainter as the Ga coverage increased. The (2x3), (2x5) LEED patterns reported previously by other studies [22] were not observed in this study.

### 6.2.2 XSW measurements

To investigate the Ga dimer orientation and test existing theoretical models, we conducted a series of (004) XSW measurements on surfaces with various Ga coverages ranging from 0.35 ML to 0.55 ML. The incident photon energy was tuned to 13 keV for the (004) scans.

To study the surface stability and Ga growth mode, the (004) and (022) XSW measurements were undertaken on a 1 ML Ga/Si(001) surface before and after an annealing to 300°C for one hour. The incident photon energy was 17 keV for the (004) scans and 12 keV for (022) scans.

To measure the Ga dimer bond length and the thermal vibrational amplitude of the Ga ad-atom on Si(001) at RT, the Si (004), (022) and (008) XSW measurements were performed on the 0.3 ML Ga/Si(001) surface. For each above measurement, the incident photon energy was tuned to 12.0 keV, which is above the Ga K absorption edge. During the (008) measurement, a 150- $\mu$ m Al foil was placed in front of the monochromator to attenuate the coexisting 6.0 keV photons from the (004) reflection to 1%. To double check the stability of the surface, another (004) XSW measurement was taken immediately after the (008) measurement. The (004), (008) and (022) XSW results are shown in Fig. 6.3 (a), (b) and (c), respectively.

Figure 6.3 Experimental data (dots) and theoretical curves (solid lines) for the normalized Ga K $\alpha$  fluorescence yield and Si reflectivity (R) versus Bragg reflection angle  $\theta$  for: (a) the Si(004) reflection and (b) the Si(008) reflection on a 0.3 ML (2x2) Ga/Si(001) surface.

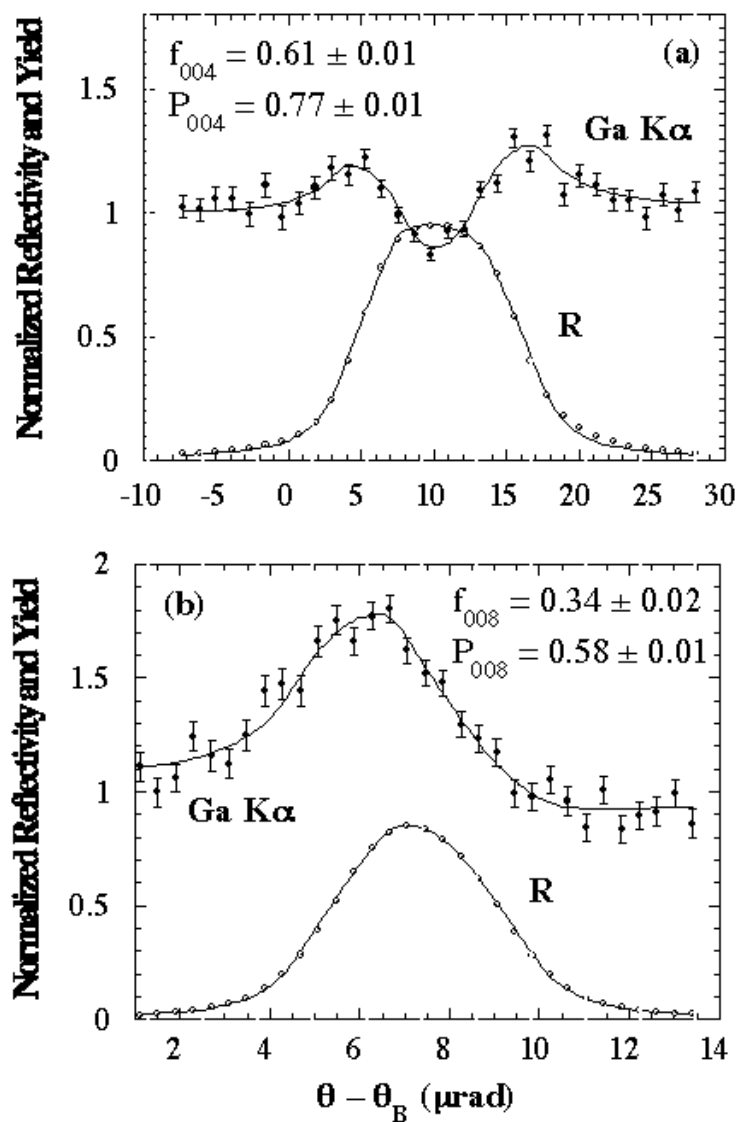
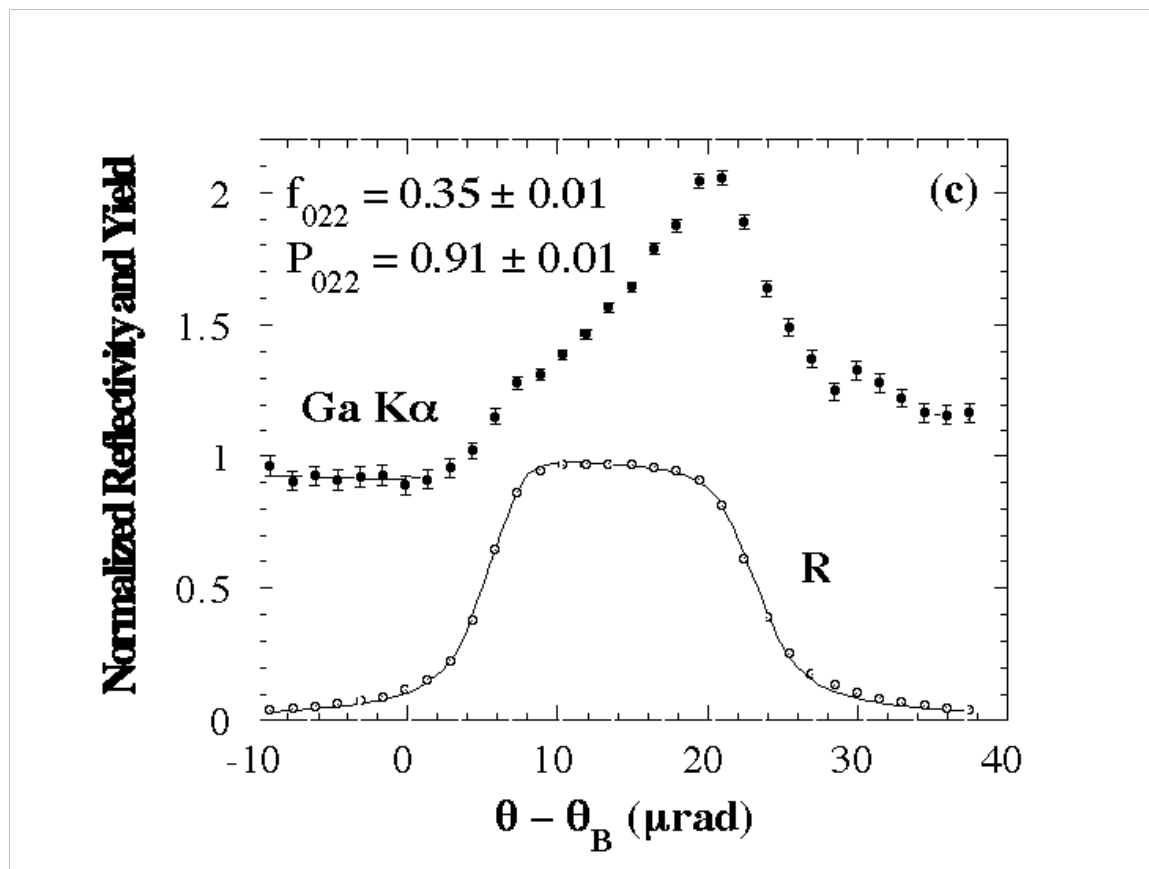


Figure 6.3 (c) Experimental data (dots) and theoretical curves (solid lines) for the normalized Ga K $\alpha$  fluorescence yield and Si reflectivity (R) versus Bragg reflection angle  $\theta$  for the Si(022) reflection on a 0.3 ML (2x2) Ga/Si(001) surface.



## 6.3 Results and discussion

### 6.3.1 Dimer orientation

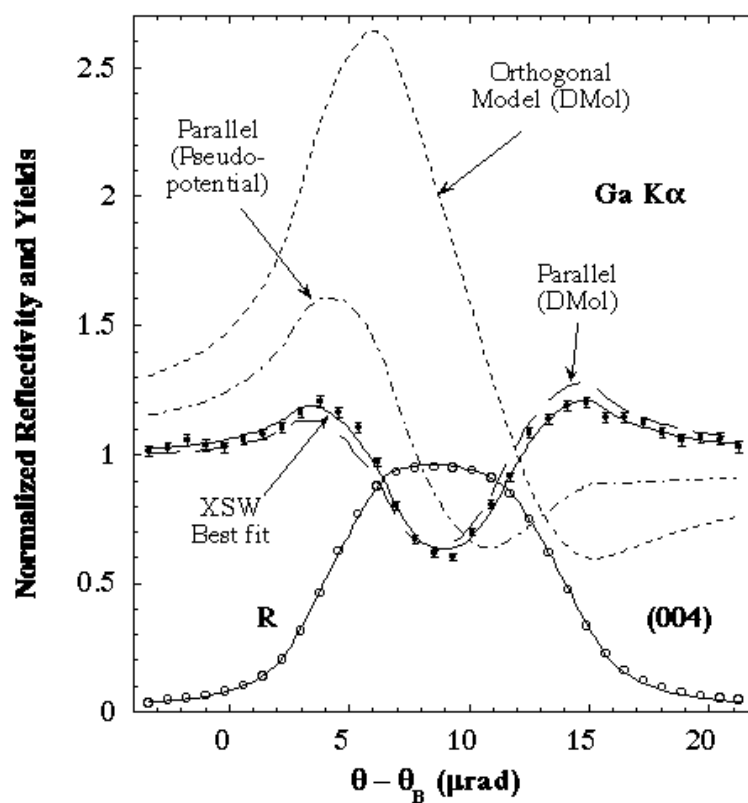
The derived coherent fractions and coherent positions determined from a series of (004) XSW measurements on surfaces with various Ga coverages are tabulated in Table 6.1. Independent of Ga coverage, the Ga ad-dimer height above the Si(004) bulk-like atom plane is consistently measured to be  $h'_{\text{Si(004)}} \cdot d_{004} = 1.03 \pm 0.02 \text{ \AA}$ . This height agrees with the value of 1.05 Å predicted for the parallel ad-dimer by the DMol calculation [97, 117] perfectly. It is also in reasonable agreement with the earlier theory prediction of 0.92 Å [93] for the parallel model. The height predicted for the orthogonal model (0.69 Å by Ref. [97, 117] and 0.60 Å by Ref. [93]) is significantly lower. Therefore, these XSW measurements provide direct proof for the parallel ad-dimer model on the low coverage Ga/Si(001) surface.

To demonstrate the sensitivity of the XSW measurement to the change in Ga height, Fig. 6.4 compares the (004) XSW experimental Ga K $\alpha$  fluorescence yield from the 0.35 ML surface and the best fit of Eq. 2.36 to data with the yield curves based on  $h'$  values predicted by the parallel and orthogonal model of DMol calculations [97, 117] as well as the parallel model of the pseudopotential calculation [93]. For this comparison, the ordered fraction was set at the value that was determined from the best fit ( $C = 0.89$ ). It can be easily seen in Fig. 6.4 that the XSW experimental curve is in excellent agreement with that based on the parallel model of DMol calculations, and in complete disagreement with the orthogonal model which only differs in height by 0.36 Å. Furthermore, although the predicted curve by the parallel model of Ref. [93] is in

Table 6.1 A series of (004) XSW measurements on Ga/Si(001) with various Ga coverages.  $\Gamma_{\text{Ga}}$ : Ga coverage;  $h'$ : Ga ad-dimer height relative to (004) bulk-extrapolated atom planes; C: ordered fraction. Note that the ordered coverage  $C \cdot \Gamma_{\text{Ga}}$  is relatively constant.

$\Gamma_{\text{Ga}}$ (ML)	$f_{004}$	$P_{004}$	$h'$ (Å)	C	$C \cdot \Gamma_{\text{Ga}}$
( $\pm 0.05$ )	( $\pm 0.01$ )	( $\pm 0.01$ )	( $\pm 0.02$ )	( $\pm 0.03$ )	(ML)
0.35	0.73	0.76	1.03	0.89	0.31
0.40	0.69	0.75	1.02	0.84	0.34
0.45	0.67	0.75	1.02	0.82	0.37
0.50	0.55	0.76	1.03	0.67	0.34
0.55	0.54	0.76	1.03	0.66	0.36

Figure 6.4 Experimental data and theoretical (DMol [97, 117] and Pseudo-potential [93]) curves for the normalized Ga K $\alpha$  fluorescence yield and Si reflectivity (R) versus Bragg reflection angle  $\theta$  for the Si(004) reflection for the 0.35 ML Ga/Si(001) surface.



rough agreement, the sensitivity of the XSW measurement can easily discriminate the two theoretical predictions. Therefore, the combined efforts of the high-resolution XSW measurements in current study and the DMol calculations by our collaborators Tang and Freeman clearly ruled out the orthogonal model and confirm that Ga ad-atoms form parallel dimers on the Si(001) surface.

### *6.3.2 Ga growth mode and coverage dependency of the local structure*

As shown in Table 6.1, the measured (004) coherent positions remain the same value independent to the Ga coverage. This implies that the local structure on the Ga/Si(001) surface is unchanged as coverage increases. From measured (004) coherent fractions, the ordered fraction  $C$  is determined based on the Debye-Waller factor for the RT Ga/Si(001) surface obtained from the high-order harmonic measurements (to be presented in section 6.3.3). It is interesting to note that as the Ga coverage is increased from 0.35 ML to 0.55 ML, the Ga ordered fraction  $C$  is reduced from 0.89 to 0.66. However, the resulting ordered coverage  $C \cdot \square_{\text{Ga}}$  remains constant at  $\approx 0.33$  ML. This feature, along with the constancy of the measured coherent positions, indicates that under the given growth conditions only one ordered structure is formed and that Ga in excess of  $\approx 1/3$  ML is disordered and presumably forms Ga clusters. The fact that the highest ordered coverage is below the ideal value of  $1/2$  ML is consistent with STM images [6, 88, 89] which show vacancies, defects, missing ad-dimer rows and antiphase domains. The highest ordered fraction ever obtained on the Ga/Si(001) surface is 0.89 at very low coverage (0.35 ML). In contrast to group V adsorbed Si(001) surfaces which in general is well-ordered (ordered fraction above 95%), the Ga/Si(001) surface demonstrates poor ordering.

The determined coherent fractions and coherent positions as well as the ordered fraction  $C$  from the XSW scans taken before and after the annealing to  $300^{\circ}\text{C}$  are listed in Table 6.2. After the annealing, the (004) coherent position remains unchanged and is identical to the value found for the low coverage (2x2) surfaces. This indicates that the local ordered structure along the surface normal direction (the height of (2x2) ad-dimers) remains unchanged after annealing. However, the (004) coherent fraction sees a considerable drop, corresponding to a decrease of the ordered fraction from  $\sim 50\%$  to  $\sim 30\%$ . In the meantime, the (022) coherent fraction has changed dramatically. These changes can probably be viewed as evidences for an incommensurate phase, which may be the (1x8) or (nx8) phases observed by LEED and STM [6, 22]. Since there is no sufficient detailed information about this phase, no further discussion will be made.

In their LEED and AES study, Bourguignon *et al.* observed a (1x2) pattern for a 1 ML Ga/Si(001) surface [22]. They suggested that this surface phase corresponds to the completion of a full monolayer of Ga ad-dimers upon removal of the (2x1) Si reconstruction, similar to the case of group V saturated Si(001) surface. However, based on the results of current study, this is very questionable. Referring to Fig. 6.1 and Fig. 6.2, the formation of this 1 ML saturated Ga/Si(001) surface requires two things to happen. First, the (2x1) Si reconstruction has to be lifted up and this would probably result a height change for the Ga ad-dimer. In the current study, there is no noticeable change in the (004) coherent fraction measured on the 1 ML surface in comparison to the low coverage (2x2) surfaces. Second, changing from the low coverage (2x2) phase to the (1x2) saturated surface requires a  $90^{\circ}$  rotation of the Ga ad-dimer (from parallel to orthogonal) based on the tetrahedral bonding geometry of Si. The rotation of the Ga ad-dimer requires extra energy on the surface and the way to supply extra energy is to anneal the surface. As shown previously, annealing destroys Ga ordered structure and causes

Table 6.2 The (004) and (022) XSW measurements on the 1 ML Ga/Si(001) surface before and after annealing to 300° C. h': Ga ad-dimer height relative to (004) bulk-extrapolated atom planes; C: ordered fraction.

	$f_{004}$ ( $\pm 0.01$ )	$P_{004}$ ( $\pm 0.01$ )	$f_{022}$ ( $\pm 0.01$ )	$P_{022}$ ( $\pm 0.01$ )	$h'$ (Å) ( $\pm 0.02$ )	C ( $\pm 0.03$ )
Before	0.45	0.76	0.25	0.88	1.03	0.54
After	0.38	0.76	0.14	0.85	1.03	0.29

island formation. Based on these arguments, it is quite possible that the (1x2) saturated Ga/Si(001) is not energetically favorable and does not exist in reality. As the Ga coverage exceeds 0.5 ML, the current study shows that Ga still forms the (2x2) local structure with an increasing amount of disordered Ga. The excess Ga is more likely to form islands or clusters rather than dimers to break the underlying Si(001) reconstruction. The (1x2) LEED pattern observed on 1 ML surface is probably due to the remaining Si(001) reconstruction. The Ga (2x2) local structure is probably mixed with disordered Ga clusters and does not have long range order to contribute to an observable (2x2) pattern.

### 6.3.3 *Thermal vibrational amplitudes*

As shown previously, the Debye-Waller factor can be determined from XSW coherent fractions  $f_{004}$  and  $f_{008}$ , if the ordered fraction  $C$  is constant. To double check this, the (004) XSW measurements were undertaken on the investigated surface before and after the (008) XSW measurement. The same  $f_{004}$  and  $P_{004}$  values within the range of error were obtained from these two measurements. This indicates that the surface structure and the ordering are very stable at RT over a long period of time (20-30 hours) required by the combined (004) and (008) measurements. With the measured coherent fractions  $f_{004} = 0.61 \pm 0.01$  and  $f_{008} = 0.34 \pm 0.02$  and using Eq. 2.48, the thermal vibration amplitude of the Ga ad-atom on the Si(001) surface along [001] at room temperature is found to be  $0.135 \pm 0.01 \text{ \AA}$ . From Eq. 2.50 the corresponding Ga ordered fraction was  $C = 0.74$  for this surface preparation.

As stated by Eq. 2.49, ideally, the (008) coherent position should be twice the (004) coherent position (up to modulo 1). In the current study, the measured value  $P_{008} =$

$0.58 \pm 0.02$  is slightly (0.04) larger than that predicted from the (004) value. The (008)-determined Ga ad-dimer height is  $0.03 \pm 0.02$  Å higher than the (004) value. Although this difference may not be appreciable for most structural techniques, it is near the limit of the XSW uncertainty range. From the present data, there is lack of sufficient information to fully interpret this reproducible feature in this XSW measurement. The most probable cause is the anharmonicity of the Ga adatom thermal vibration mode. Unlike atoms in bulk condensed matters which are surrounded by symmetric potential wells, surface atoms experience a different environment. For a Ga adatom on the Si(001) surface, the potential well is expected to asymmetric, especially along the surface normal direction, since the Ga adatom bonds only to one side (to Si) and is free of restriction on the side towards the vacuum. This asymmetry in the bonding potential well causes the Ga ad-atom time-averaged spatial distribution to be asymmetrical (*i.e.* non-Gaussian distribution) in the [001] direction. Therefore, Eq. 2.49 no longer strictly holds. Future experiments are needed to thoroughly explore the sensitivity of the higher-order harmonic coherent position to this anharmonicity effect.

#### 6.3.4 Dimer bond length

The Ga ad-dimer bond length  $L$  can be determined by combined (004) and (022) measurement using Eq. 2.45. This requires the Debye-Waller factor to be known along the [011] direction. Both experiment [49] and calculation [85] have shown that the anisotropy of the thermal vibration amplitude of metal ad-dimers on Si(001) is rather small at room temperature. Lacking an (044) XSW measurement, it is reasonable to assume that the Ga ad-atom has the same thermal vibration amplitude ( $0.135$  Å as measured for [001]) along both [001] and [022] directions. Therefore, the RT (022)

Debye-Waller factor is  $D_{022} = 0.91$ . With the measured coherent fractions of  $f_{004} = 0.61 \pm 0.01$  and  $f_{022} = 0.35 \pm 0.01$ , the Ga ad-dimer bond length  $L$  is determined to be  $2.58 \pm 0.04 \text{ \AA}$ . The value of  $L$  predicted by the cluster calculation ( $L = 2.65 \pm 0.05 \text{ \AA}$  [97, 117]) and by pseudo-potential calculation ( $2.63 \text{ \AA}$  [93]) are in good agreement with the XSW measurement.

Most recently, H. Sakama *et al.* [105] studied the Ga/Si(001)-(2x2) surface using the tensor LEED method. Their experiments measured the Ga dimer bond length to be  $2.62 \text{ \AA}$  and the dimer height above the ideal surface to be  $1.02 \text{ \AA}$ . This result is in excellent agreement with current study as well as theory predictions [93, 97, 117]. As a comparison, Table 6.3 tabulates structural parameters measured by the current study [98] and the tensor LEED [105] on the (2x2) Ga/Si(001) surface as well as values predicted by the pseudopotential [93] and DMol [97, 117] calculations for the orthogonal dimer model and the parallel dimer model.

Table 6.3 Theoretically calculated and experimentally measured structural parameters for the Ga ad-dimer on the (2x2) Ga/Si(001) surface: L is the bond lengths of the Ga ad-dimer, and h' is the height of the Ga dimer above the bulk-like Si(004) surface atom plane.

	Parallel Model		Orthogonal Model		Tensor LEED	XSW
	Ref. [97, Ref. [93]		Ref. [97, Ref. [93]		(Ref. [105])	Ref. [98]
	117]		117]			
L (Å)	2.65	2.63	2.64	2.50	2.62	2.58 ± 0.04
h' (Å)	1.05	0.92	0.69	0.60	1.02	1.05 ± 0.02

## 6.4 Summary

The surface structure, thermal vibration, growth mode and surface stability of Ga adsorption on Si(001) has been investigated by x-ray standing waves. The Ga/Si(001) surface is found to be less stable and less ordered than group V saturated Si(001) surfaces. The RT ordered local structure for Ga adsorption on Si(001) is found to be the (2x2) phase, occurring at coverages below 0.5 ML. In combination with a theoretical calculation [97, 117], for the first time, the current study provides direct evidence that Ga forms parallel ad-dimers on top of the Si dimerized surface. The structural parameters are precisely measured by XSW and are in excellent agreement with theory predictions and results from other measurements. In contrast to group V elements, the Ga coverage does not saturate at a full monolayer on Si(001). With increasing Ga coverage, the surface ordering is found to decrease and excess Ga presumably forms Ga islands on the surface rather than dimers to break the Si reconstruction. In general, Ga adsorption on Si(001) is found to have a completely different behavior and structure than that of group V elements.

## Chapter VII Summary and Outlook

### 7.1 Summary

The purpose of this thesis is to incorporate a systematic method of investigating surface structure, adsorption behavior, surface dynamics and kinetics of adsorbates on crystalline surfaces by the XSW technique. In the current studies, three surface systems have been studied: Sb/Si(001) [79, 99], Bi/Si(001) [80] and Ga/Si(001) [97, 98, 117]. The surface structural parameters, such as: ad-dimer height, ad-dimer bond length and substrate relaxation have been precisely measured and found to be in good agreement with results of previous measurements by other techniques and theory predictions. Using high-order harmonic reflection XSW measurements, the RT thermal vibration amplitudes of Sb, Bi and Ga adatoms on Si(001) were directly determined. The current study has also tried to explore the potential of using the XSW technique in new areas of investigating surface stability, growth mode, phase transition and surface kinetics on crystalline surfaces.

#### 7.1.1 Group V elements adsorption on Si(001)

In the current study, group V elements (Sb and Bi) are found to remove the Si(001) (2x1) reconstruction upon annealing and to form a (1x2) dimerized adlayer on top of the unreconstructed Si(001) surface. The Sb (Bi) adsorption on Si(001) saturates at a coverage slightly less than 1 ML and the saturated surface is highly ordered and very

stable. Another group V element studied by XSW, As, was found to have a similar behavior by Franklin *et al* [49]. XSW experiments found that these elements desorb at different temperatures. Bi starts desorbing at 500°C, Sb desorbs at temperatures above 550°C, and As stays on the surface until 600°C. This result suggests that As has the strongest bonding with Si among the three group V elements. This is consistent with the theory prediction that As has the highest chemisorption energy (3.68 eV) on Si(001) [115] in comparison to Sb (3.26 eV) [115] and Bi (3.00 eV) [116]. XSW experiments also find that the saturated As/Si(001) surface has a higher ordered fraction ( $\sim 100\%$ ) [49] than Sb/Si(001) ( $\sim 95\%$ ) and Bi/Si(001) ( $\sim 95\%$ ).

To summarize the structural results for the group V metals (As, Sb and Bi) adsorption on Si(001), Table 7.1 tabulates values of ad-dimer bond lengths (L) and ad-dimer heights (h') measured by XSW experiments of current study and Ref. [49, 50] and calculated by DMol calculations [115, 116], as well as covalent radii for As, Sb and Bi. As can be seen from Table 7.1, the XSW measured ad-dimer bond length of group V elements matches their covalent bond length (except for As). This suggests that As dimer is under significant tensile stress ( $L_{As} > 2r_{As}$  by 7%) while  $L_{Sb} \approx 2r_{Sb}$  and  $L_{Bi} \approx 2r_{Bi}$ . The height of the group V ad-dimer shows an increase with respect to the size of the element as well. The XSW measurements also have good agreement with theoretical predictions.

### 7.1.2 Group III adsorption on Si(001)

Ga was the only group III element investigated in the current study. In contrast to group V elements, Ga is found to form a weaker bond with Si. There is no experimental evidence that Ga removes the Si(001) (2x1) reconstruction upon adsorption. Depending on coverage, Ga forms various surface phases on Si(001), in contrast to the simple (1x2)

Table 7.1 The XSW measured and theoretically calculated dimer bond length  $L$  and height  $h'$  as well as the covalent radius  $r_{\text{cov}}$  for group V elements adsorbed on Si(001).

	$2r_{\text{cov}}$ (Å)	XSW $L$ (Å)	Theory $L$ (Å)	XSW $h'$ (Å)	Theory $h'$ (Å)
As	2.40	2.58 <sup>a</sup>	2.52 <sup>d</sup>	1.40 <sup>a</sup>	1.37 <sup>d</sup>
Sb	2.76	2.75 <sup>b</sup>	2.93 <sup>e</sup>	1.68 <sup>b</sup>	1.64 <sup>e</sup>
Bi	2.92	2.96 <sup>c</sup>	3.16 <sup>f</sup>	1.80 <sup>b,c</sup>	1.73 <sup>f</sup>

<sup>a</sup> Ref. [49].

<sup>b</sup> The current study. Ref. [79, 80, 99]

<sup>c</sup> Ref. [50].

<sup>d,e</sup> Ref. [114].

<sup>f</sup> Ref. [116].

phase formed by group V adsorption. On RT deposited low coverage ( $< 0.5$  ML) Ga/Si(001), Ga forms ad-dimers on top of the dimerized Si(001) surface with the orientation of Ga ad-dimers parallel to the underlying Si dimers. This parallel ad-dimer feature is also observed for other group III elements (Al and In) adsorption on Si(001) [60, 111]. This is a unique feature for group III elements.

These eminent differences in the adsorption behavior between group III and group V elements on Si(001) provide fundamental information for better understanding important technological issues such as surface passivation and III-V heteroepitaxy on Si(001). It is now understandable why group V elements passivate the Si(001) surface and group III elements do not [28]. It is also understandable why As always forms the first layer (As-terminated) when GaAs is grown on Si(001) under the As-rich condition [24]. This leads to the formation of antiphase domain defects of GaAs on the Si(001) surface with monoatomic steps [68]. This is a technical difficulty which may be solved by using substrates with double atomic steps (*e.g.* miscut Si(001) surfaces).

### *7.1.3 Ad-atom Thermal vibrations on Si(001)*

The current study directly measured the RT [001] adatom thermal vibration amplitude of Sb, Bi and Ga on Si(001) by using higher-order harmonics XSW measurements. These measurements represent the first direct measurement of the surface thermal vibration under a UHV environment. The use of higher-order harmonic XSW measurements to determine the surface thermal vibration was first demonstrated by Bedzyk and Materlik in a study of the Br/Ge(111) surface [13]. The experiment was performed in an inert gas environment rather than UHV. As a result, the Br coverage and

ordered fraction were not as well regulated as in the current study. This resulted in a much larger uncertainty in the ad-atom's vibrational amplitude.

Prior to this work, temperature dependencies of the coherent fraction ( $D_H$ ) of Ga/Si(111) [82] and As/Si(001) [49] have been measured by XSW methods, which did not employ higher-order harmonic reflections. These measurements did not directly determine the thermal vibration amplitude of the ad-atom. Their results are based on the assumption that the surface is perfectly ordered (*i.e.* ordered fraction  $C = 1$ ).

For comparison, Table 7.2 lists measured and calculated values of the adatom's thermal vibration amplitude for various Si surface systems. Sb is found to have the largest thermal vibration on Si(001) at RT (40% larger than the Si(001) clean surface estimated by theory [3]). As, Bi and Ga are found to have similar thermal vibration amplitudes on Si(001) at RT (20% larger than the Si(001) clean surface). The adatom thermal vibration amplitude measured by XSW is relative to the bulk lattice. The thermal vibration between nearest neighbor atoms can be measured by SEXAFS. By combining the XSW and SEXAFS measurements, the thermal vibration amplitude of top layer Si atoms, as well as the value between the adsorbate and top layer Si atoms, can be determined (in analogous to the determination of the surface relaxation).

Table 7.2 Measured and calculated thermal vibration amplitudes  $\sqrt{\langle u_H^2 \rangle}$  at room temperature.

$\sqrt{\langle u_H^2 \rangle}$ (Å)	Experiments	Theory
Bulk Si Ref. [78]	0.075	
Si on Si(111) Ref. [3]		0.12
Si on Si(001) Ref. [3]		0.11
As on Si(001) Ref. [49]	0.14	
Sb on Si(001) Ref. [99]	$0.156 \pm 0.01$	
Bi on Si(001) Ref. [80]	$0.13 \pm 0.02$	
Ga on Si(001) Ref. [98]	$0.135 \pm 0.01$	
Ga on Si(111) Ref. [82]	0.1	

## 7.2 Future work

Currently, the low incident photon flux at the NSLS X15A beamline poses the major restriction for many XSW applications. Third generation synchrotron radiation facilities can provide much brighter (by a few orders of magnitude) x-ray source. One of them, the 7 GeV Advanced Photon Source (APS), is currently under construction at Argonne National Laboratory and is expected to start operating in early 1996. With the advent of third generation synchrotron sources, more demanding experiments, such as *in situ* surface studies, studies of surface dynamics, low coverage studies, or kinetics of surface transformations will become feasible. There are several interesting and important issues that will be resolved by using brighter synchrotron radiation sources.

### 7.2.1 Adsorbate thermal vibrations

The direct measurement of thermal vibrations requires high-order harmonic XSW measurements. Due to reasons such as narrower bandwidth and lower reflectivity of high-order reflections, high-order harmonic XSW measurements suffer a much lower fluorescence count rate than fundamental measurements. For example, currently at beamline X15A, a 1 ML Sb/Si(001) XSW measurement using the Si (004) reflection takes 2 to 3 hours with the incident photon energy of 6.2 keV. However, an (008) measurement on the same surface requires at least 18 hours to collect sufficient fluorescence counts at 9.6 keV. By moving to the APS, these time-consuming high-order harmonic measurements can be finished within minutes. With this advantage, several important issues related to the surface thermal vibration can be fully investigated:

- (a) The temperature dependence of the adsorbate thermal vibration amplitude;
- (b) The anisotropy of the adsorbate thermal vibration amplitude;
- (c) The anharmonicity of the adsorbate thermal vibration amplitude.

### *7.2.2 Surface kinetics: in situ study*

Investigations of surface kinetics are often performed on low coverage surfaces to avoid adsorbate-adsorbate interactions. The complexity of surface phases often requires off-normal and high-order harmonic XSW measurements to fully solve the surface structure and compositions. All these require a high incident photon flux to get sufficiently high fluorescence count rates. Currently at beamline X15A, the low incident flux makes the time scale (in hours) of XSW measurements inappropriate for the time scale (in minutes or less) of surface phase transitions under investigation. At much brighter sources such as APS, the time scale of XSW measurements is expected to be in minutes. Therefore, surface kinetic processes can possibly be studied in "real time".

### *7.2.3 Quadrupole effect*

As discussed in Chapter II section 2.4, the current XSW analysis is based on the dipole approximation of the photoeffect. In most cases the dipole approximation is justified since the quadrupole cross section contribution is less than 1% of the dipole contribution. However, for certain cases (such as when the incident photon energy is close to the adsorbate's absorption edge or when high-order harmonic reflections are applied with high incident photon energy), the quadrupole term may have a noticeable

contribution and therefore the dipole approximation is no longer appropriate. The quadrupole contribution may reduce the coherent fraction and thus Eq. 2.38 would have a fourth factor that accounts for the quadrupole effect. To measure these slight changes in coherent fraction, highly precise XSW measurements are required. With a brighter source like APS, statistical precision of XSW measurements can be dramatically improved.

## **Appendix A Experimental Procedure and Instrumentation**

### *A.1 Sample cleaning and mounting*

The Si (001) samples used in this thesis work are specially cut, etched and polished from high-purity (undoped) float-zone Si boules. Each sample is 4 mm thick and has a 10 mm x 10 mm square surface and two wings for strain-free mounting. (Fig. A.1)

#### *A.1.1 Si Polishing*

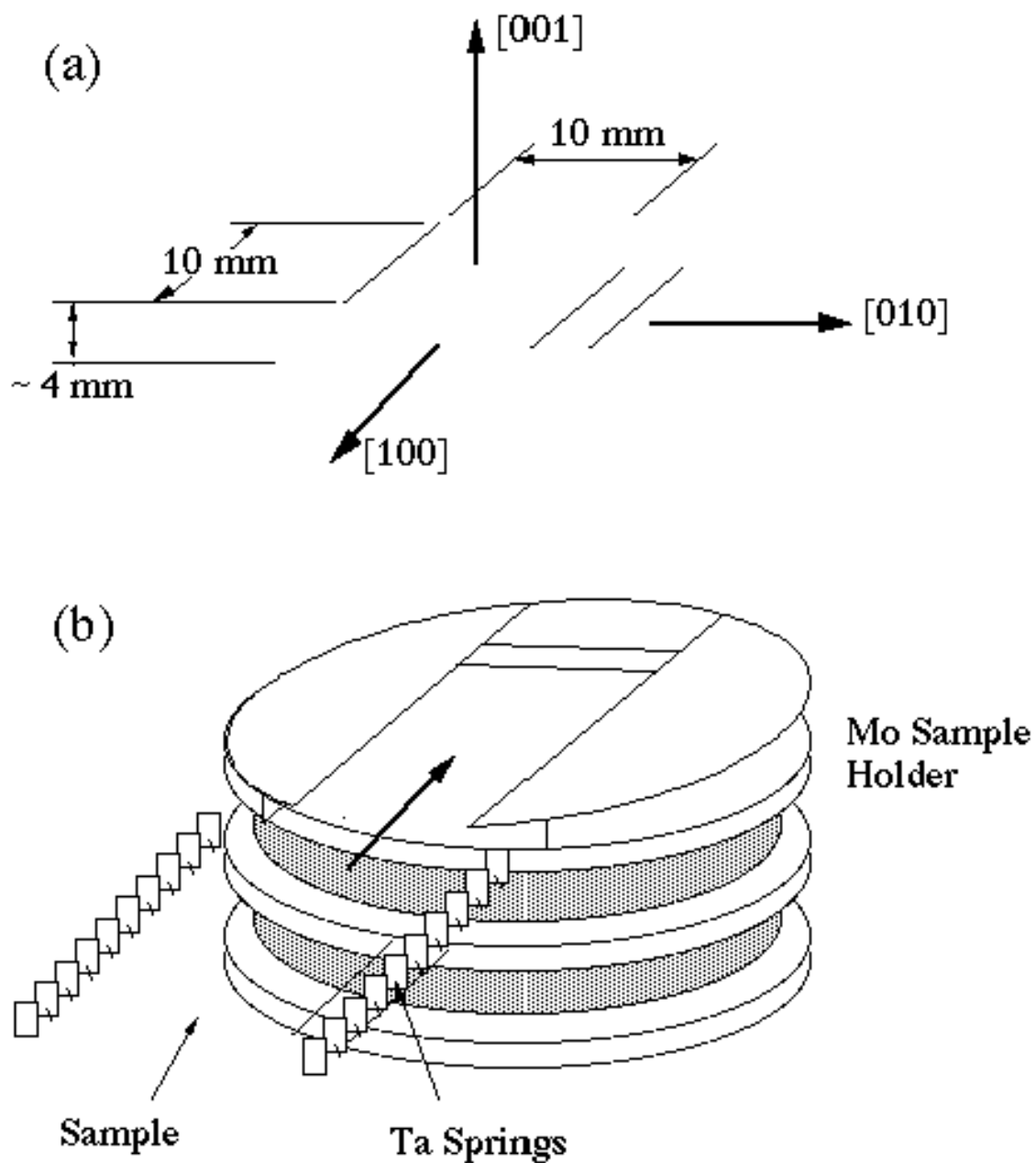
Before introduction into the UHV system, each Si(001) sample is first polished with Syton™ to obtain a mirror-like atomically smooth surface. This nonabrasive chemical polishing procedure is:

1. Wear LATEX gloves cleaned with methanol.
2. Soak Politex Supreme felt polishing pad with de ionized (DI) water.

Remove any dust particles visible on the pad.

3. Pour some Syton™ on the pad. Hold the sample face down and gently polish. Add more Syton™ when needed.
4. Polish 3 to 5 minutes until the sample surface looks mirror-like. Make sure there are no cracks or pits on the surface.
5. Rinse it with flowing water for 3 minutes. Make sure not to leave any Syton residue on the surface. Then blow dry it with dry nitrogen.

Figure A.1 (a) The Si(001) sample used in this thesis research. (b) The Mo sample holder used in X15A UHV system. The sample is held by Ta springs in a strain-free mode.



### *A.1.2 Si Etching*

To remove contaminants from the sample surface and to form a protective, carbon-free oxide layer, a chemical etching procedure similar to the Shiraki etch [59] is then performed. The procedure of the modified Shiraki etch is described as following:

1. React Si sample for 5 minutes in  $\text{H}_2\text{O} : \text{NH}_4\text{OH} : \text{H}_2\text{O}_2$  (4:1:1) at  $80^\circ\text{C}$  ( $\text{H}_2\text{O}$  means DI water).
2. Rinse with DI water three times.
3. Dip into  $\text{H}_2\text{O} : \text{HF}$  (1:1) at RT for 30 seconds.
4. Rinse with DI water three times.
5. React with  $\text{H}_2\text{O} : \text{HCl} : \text{H}_2\text{O}_2$  (5:1:1) at  $80^\circ\text{C}$  for 5 minutes.
6. Rinse with DI water three times.
7. Repeat step 3 to 6 twice.
8. Dip into  $\text{H}_2\text{O} : \text{HF}$  (1:1) at RT for 30 seconds.
9. Rinse with DI water three times.
10. React with  $\text{H}_2\text{O} : \text{HCl} : \text{H}_2\text{O}_2$  (1:3:1) at  $60^\circ\text{C}$  for 10 minutes.
11. Rinse with DI water three times.
12. Blow dry with nitrogen.

### *A.1.3 Mounting*

The sample holder used at X15A UHV system is custom designed based on the Perkin-Elmer Model 190 sample holder. It is made of molybdenum (Mo) and the outer diameter of the holder is 1" (Fig. A.1(b)). The sample is mounted on the holder and held

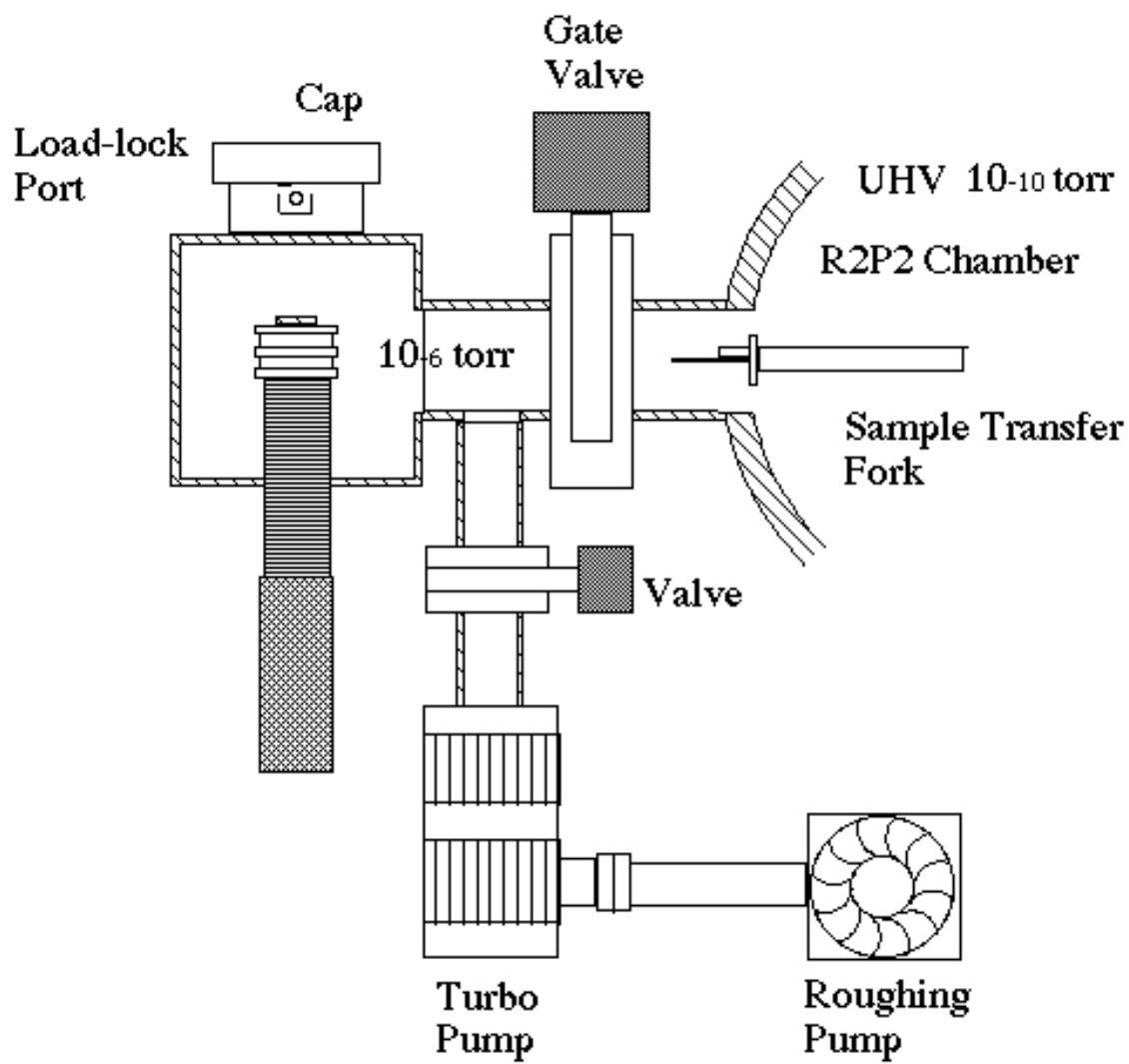
in place by tantalum (Ta) springs to avoid possible permanent strain induced during annealing. (Fig. A.1(b)) Make sure always to wear LATEX gloves and use clean tools when you handle the sample and the sample holder.

#### *A.1.4 Loading into the UHV system*

The sample is loaded into the UHV system through the load-lock port. Referring to Fig. 3.4 and Fig. A.2, the procedure of sample loading is described as following:

1. Close the gate valve between the load-lock port and R2P2 and the valve to the turbo pump. Open the cap of the load-lock port and load the sample holder in.
2. Close the cap. Start the roughing pump, then the turbo pump. Open the valve between the turbo pump and the load-lock port. Pump the port for 10 to 20 minutes.
3. Close the valve between the turbo pump and the load-lock port. Open the gate valve between the load-lock port and R2P2 chamber quickly. Watch the pressure drop in the R2P2 chamber (should be in  $10^{-8}$  torr). Insert the sample transfer fork into the load-lock chamber and grab the sample holder and move it into the R2P2 as quick as possible.
4. Close the gate valve between the load-lock port and the R2P2 chamber after the sample is safely transferred into R2P2. Wait about one hour for the pressure to return to normal ( $\sim 10^{-10}$  torr).

Figure A.2 The load-lock system for the UHV chamber at NSLS X15A.



## *A.2 Operation of the UHV system*

### *A.2.1 General information*

The multi-chamber UHV system at X15A is custom designed and made to perform sample introduction, sample preparation and characterization, and special requirements for XSW measurements. As shown schematically in Fig. 3.4, the UHV system consists of five parts: the load-lock chamber, the R2P2 chamber, the analysis chamber, the sample preparation chamber and the x-ray chamber. A detailed information about individual UHV equipment / component can be found in Table A.1. The base pressure of the system (except the load-lock chamber) is about  $9 \times 10^{-11}$  torr. The whole UHV system is bakable to 250°C.

Table A.1 Part list for the multi-chamber UHV system. (Referring to Fig. 3.4)

Parts	Vendor information	Description
R2P2 Chamber	Vacuum Generators LTD. Ref S-103-01-3	UHV multi-exit specimen transfer vessel (R2P2). Bakable to 250 °C.
Load-lock Chamber	Perkin-Elmer	
X-ray Chamber	Perkin-Elmer.	X-ray chamber custom designed by Perkin-Elmer.
Sample Manipulator in X-ray Chamber	Perkin-Elmer Precision Specimen Stage Model 15- 630 Mod.	Micro stepping motor driven precision x, z, $\phi$ , $\psi$ sample manipulator with resistive heater (up to 600°C). Range: x from -10 mm to 10 mm, z from -15 mm to 5 mm, $\phi$ , $\psi$ from -5° to 95°.
Photodiode	Hamamatsu Si Photodiode. S-3590 Series.	Si photodiode (from visible light to UV). 10 mm x 10 mm area. Good for UHV.
Photodiode Manipulator	Thermionics LMAB-1.04-2	2" travel axial motion manipulator. 2.75" O.D.
Photodiode Rotary Feedthrough	Thermionics FRM-275- 25/MSW.	Motorized rotary feedthrough, 2.75" O. D., worm gear drive with manual knob.
MBE Chamber	Perkin-Elmer.	Perkin-Elmer custom design.

Sample Manipulator in MBE Chamber	Perkin-Elmer 10-325.	X, y, z, and tilt sample manipulator with resistive heater (up to 1000°C).
Thickness Monitor		Quartz oscillator thickness monitor.
Knudsen Cell	Perkin-Elmer.	Perkin-Elmer Effusion cell.
Reverse-View LEED	PRI RVL 8-120.	Reverse-view LEED system.
LEED Electronics Control	PHI Model 11-020 LEED Electronics Control.	LEED electronics control module.
AES Analyzer	PHI 10-155.	Perkin-Elmer CMA.
AES Electron Gun Control	PHI 11-010.	Electron gun control module for AES system.
AES System Control	PHI 11-500A.	Auger system control module.
Lock-In Amplifier		
Ion Pump	Perkin-Elmer Model 2070420	400 l/s ion pump with TSP (Titanium Sublimation Pump, Model 2140411) / Cryo-shroud.
Cryopump	CVI Model TM150	CVI TorrMaster cryopump. N <sub>2</sub> : 1700 l/s; H <sub>2</sub> : 2500 l/s; H <sub>2</sub> O: 4500 l/s; Ar: 1400 l/s.

### A.2.2 AES and LEED: Operation

#### (a) Auger Electron Spectroscopy

The UHV system at X15A is equipped with a cylindrical-mirror-analyzer (CMA) from Perkin-Elmer for Auger electron spectroscopy (Fig. 3.4). The AES system is controlled by Perkin-Elmer control modules illustrated in Fig. A.3. The operation procedure of the AES system at X15A is described as following:

1. Bring the sample into the LEED and AES port from R2P2 chamber. Face the sample to the AES and make sure the electron beam is hitting the sample. Ground the sample correctly.
2. Mount graph paper on the X-Y plotter. Set the pen to ready.
3. Electron Gun Control module:
  - (a) Turn on power. Push the "green" button, then the "red" button.
  - (b) Set the Filament Current at  $\sim 1$  mA (after 8 full turns).
  - (c) Set to dN/dE mode.
  - (d) Set the Beam Voltage to 3 kV.
4. Electron Multiplier Supply module:
  - (a) Turn on power.
  - (b) Push the "HV" button. Set HV to 1.5 kV.
5. Auger System Control module:
  - (a) Turn on power.
  - (b) Set X-Axis Scale (200 eV/division) and Sweep Rate (2 eV/sec).
  - (c) Set the Lower and Upper Limits of the scan energy (depending on peaks interested).

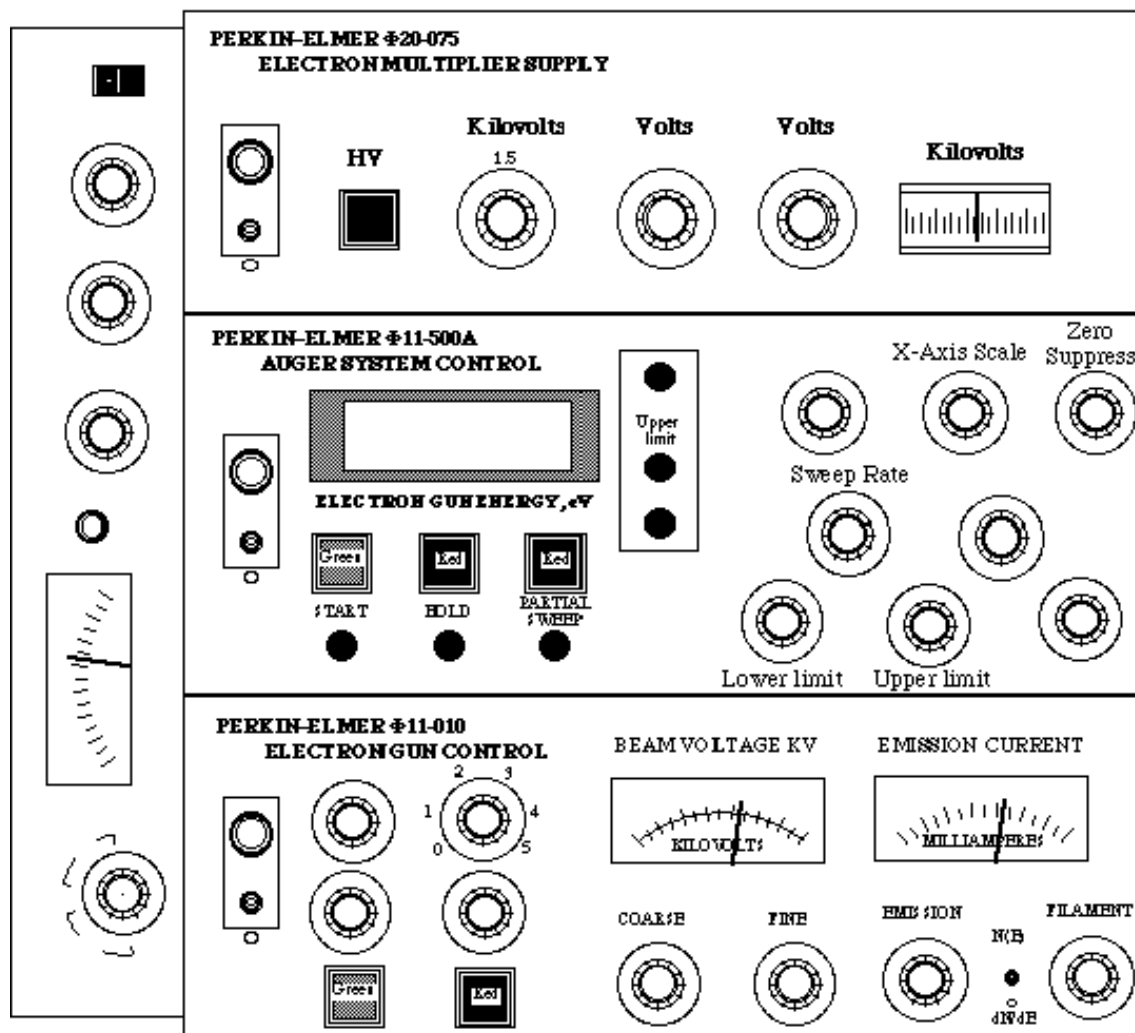
6. Amplifier module:

(a) Adjust Signal Sensitivity knob and check peak-to-peak range on the plotter.

(b) Change Signal Sensitivity to different scale at different regions to maximize the output and to fit into the graph paper.

7. After everything is ready, push the "Start" button on the Auger System Control module to start the scan. After scan is finished, push the "Start" button again to stop.

Figure A.3 A schematic drawing of the front panel of the AES electronic control modules.



(b) Reverse-view LEED

The operation procedure of the LEED system at X15A is described as following (referring to Fig. 3.4 and A.4):

1. Bring the sample into the LEED and AES port from R2P2 chamber. Face the sample to the LEED and move the sample as close as possible to the LEED electron gun.

Ground the sample correctly.

2. LEED Control module:

(a) Turn on power. Set Screen Voltage to 4 kV.

(b) Set Filament Current to 1 mA (after 5 full turns).

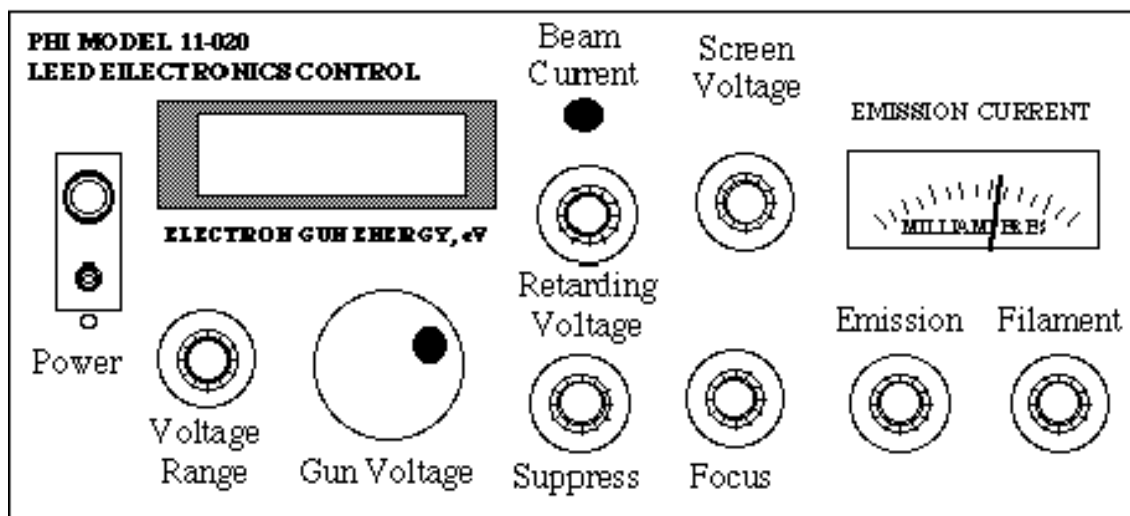
(c) While pushing the Beam Current button in, adjust the Emission knob to get a maximum beam current.

(d) Adjust Gun Voltage around 50 to 80 eV until an image is obtained on the screen.

(e) Keep adjusting Focus, Gun Voltage, Suppression and Emission knobs until a sharp image with low background is obtained.

3. LEED images can be recorded by a Polaroid camera at the beamline.

Figure A.4 A schematic drawing of the front panel of the LEED electronic control modules.

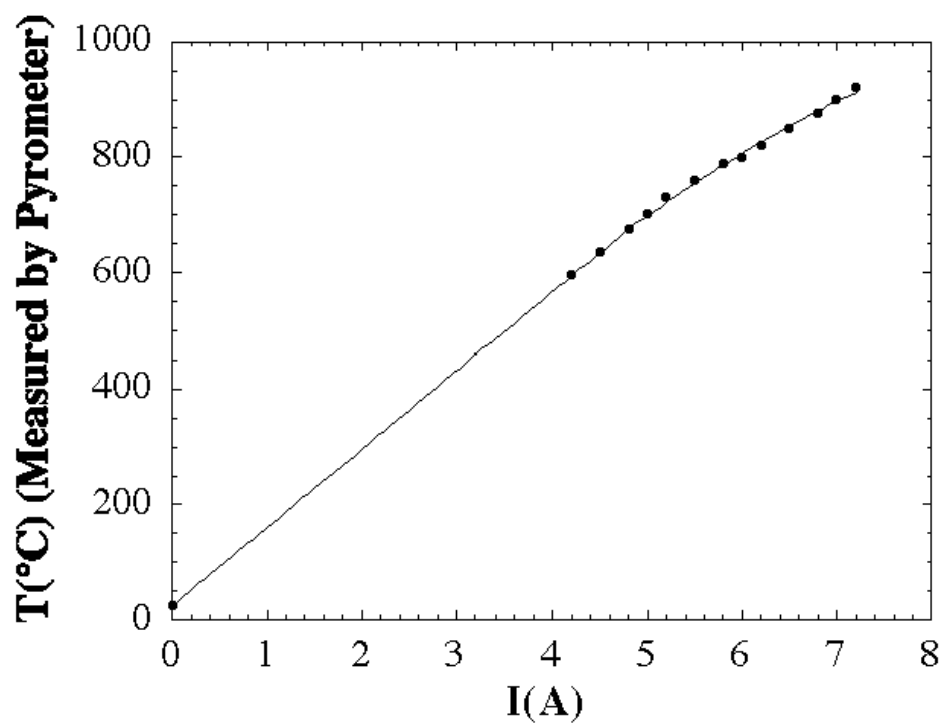


### *A.2.3 Heating stage*

#### (a) The heating stage in MBE chamber

Referring to Fig. 3.4, the sample preparation (MBE) chamber has a sample manipulator with x, y, z and tilt adjustments. Depending on different sample surfaces, sample can be treated with either ion sputtering or annealing. For the Si(001) surface, we always clean the surface by annealing. By applying currents to the tungsten-filament heating stage on the sample manipulator, the sample can be annealed to various temperatures up to 950°C. The temperature of the sample can be directly measured by an optical pyrometer when it is above 500°C. When the temperature is below 500°C, where pyrometers are not reliable, it can be indirectly measured by an Al-Cr thermo-couple attached to the heating stage or estimated by the current applied to the heating stage. Fig. A.5 plots the sample temperature (measured by an optical pyrometer) as a function of the heat current.

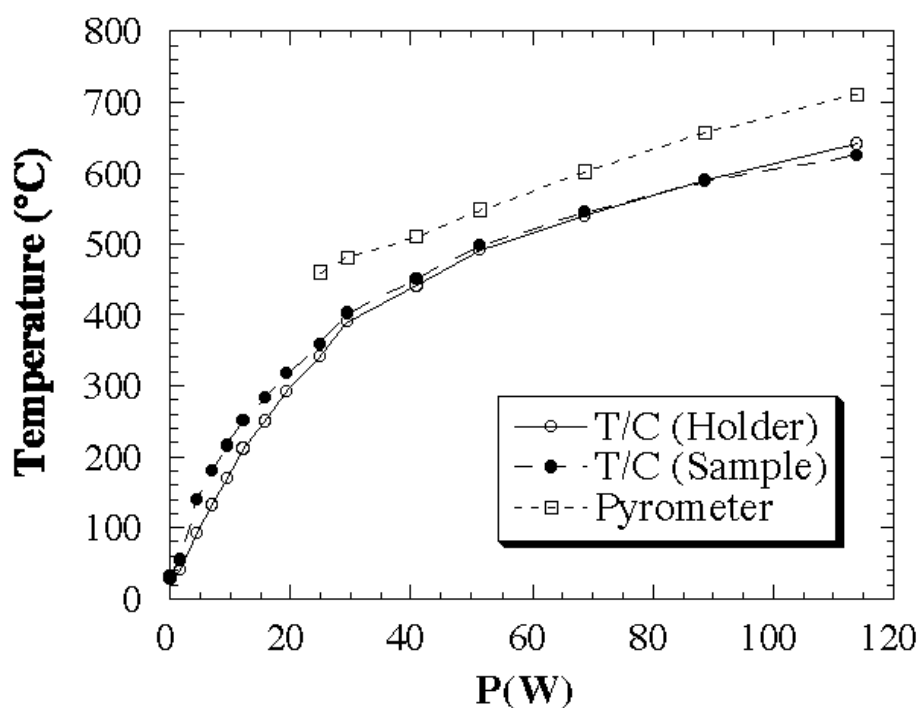
Figure A.5 The calibrated sample temperature (measured by an infrared pyrometer) vs. heating current curve for the heating stage in the deposition chamber. The equilibrium time for each point is 10 minutes.



(b) The heating stage in the x-ray chamber

In the x-ray chamber of the UHV system at X15A, the sample is mounted on a custom designed sample manipulator with x, z,  $\phi$  and  $\psi$  motions (Fig. 3.4). The sample manipulator contains a tungsten filament heating stage which can anneal the sample up to 600°C. The sample temperature can be indirectly measured by an Al-Cr thermo-couple attached to the heating stage. The temperature reading by this thermo-couple was calibrated by a special thermo-couple directly touching the sample surface and an optical pyrometer at various heating powers. Calibration curves are plotted in Fig. A.6.

Figure A.6 The calibrated curve of sample temperature vs. heating power for the heating stage in the x-ray chamber. T/C (Holder) curve represents temperatures measured by the thermal couple attached to the sample holder. T/C (Sample) curve represents temperatures measured by a special thermal couple buried in the dummy sample. The pyrometer curve represents temperatures measured by the infrared pyrometer looking at an angle of 45° to the sample. Equilibrium time at each point is 15 minutes.

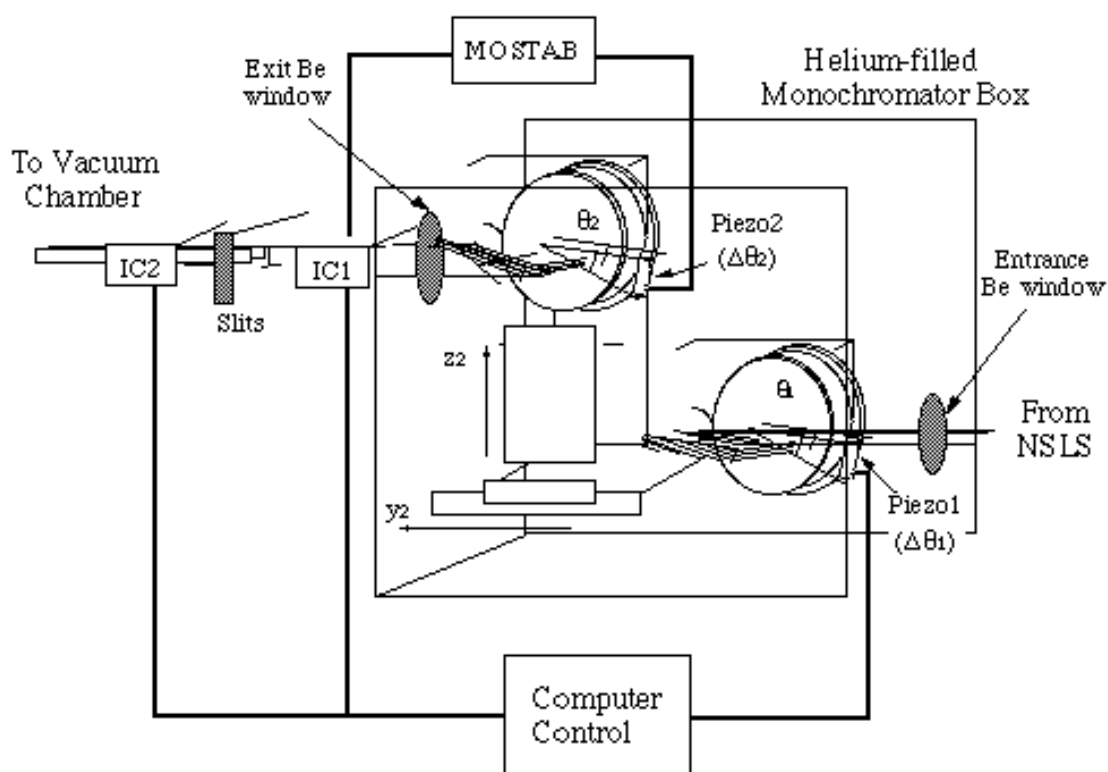


### *A.3 Monochromator*

#### *A.3.1 Double-crystal monochromator at X15A*

The double-crystal monochromator at X15A beamline consists of two single crystals independently controlled by two separate goniometers. (Fig. A.7) With the two stepping motor driven goniometers mounted on stepping motor driven translation stages, Bragg angles from  $0^\circ$  to  $\sim 85^\circ$  are accessible by the monochromator and thus a large energy tuning range is achieved. Each goniometer is equipped with a piezo-driven torsion bearing stage for ultra-fine  $\Delta\theta$  angle adjustment. The  $\Delta\theta$  drive has an angular range of  $350^\circ$  rad with an angular resolution better than  $0.3^\circ$  rad. The whole monochromator arrangement is contained within a stainless steel box which can be pumped down to  $10^{-2}$  torr and back filled with helium gas to reduce x-ray absorption by air and to eliminate ozone production. The monochromatic beam from the monochromator exits the helium box through a thin ( $\sim 10$  mil) beryllium (Be) window and passes through two ionized chambers (IC1 and IC2) and a rotatable motorized slit assembly before being introduced into the UHV chamber. (Fig. 3.4) The signal of the first ion chamber IC1 is used as a feedback to stabilize the output monochromatic x-ray beam. The IC2 signal is used to normalize the reflected x-ray intensity and the fluorescence yield. The slit size is precisely controlled by stepping motors with the minimum step of  $5^\circ$  m. The slit system itself is held on a vertical jack and a translation stage and it can scan the x-ray beam across the sample surface.

Figure A.7 Mechanical and electronic control system of the double-crystal monochromator at NSLS X15A.



The use of two independently mounted crystals requires precise angular and positional adjustability of both. The diffraction planes of the crystals are aligned to be parallel to each other but the reflection angle  $\theta$  of the crystals are slightly detuned in order to suppress harmonics efficiently [69, 84]. The angular fine tuning is performed by piezo torsion bearing stages. The piezo of the second crystal (or  $\Delta\theta_2$ ) is controlled by an analog feedback system called MOSTAB [69]. With the output signal of the ion chamber 1(IC1), the MOSTAB unit can "lock in" a rocking curve by controlling the angular alignment of the second crystal relative to the first crystal to keep IC1 at a constant percentage of its maximum output. With the MOSTAB unit, one can choose to lock in a rocking curve at its right side to suppress harmonics (*e.g.* (008) reflection) or at its left side to enhance harmonics (Fig. A.8).

Table A.2 contains detailed information about individual components of the double-crystal monochromator used at X15A.

Figure A.8 5 keV photons via the fundamental Si (004) reflection and 10 keV photons via the second-order harmonic (008) reflection can pass through the monochromator at the same time at synchrotron radiation. For a symmetric monochromator (plot (a)), these two reflections are centered with each other. With an asymmetric monochromator (plot (b)), the slight difference in absolute angular scale and width of the (004) and (008) reflections makes them separable from each other via detuning the double-crystal monochromator using the MOSTAB unit. As shown in plot (b), by locking to the right side of the rocking curve one eliminates the 10 keV high-order harmonic reflection. By locking to the left side, one enhances the (008) reflection over the fundamental (004) reflection.

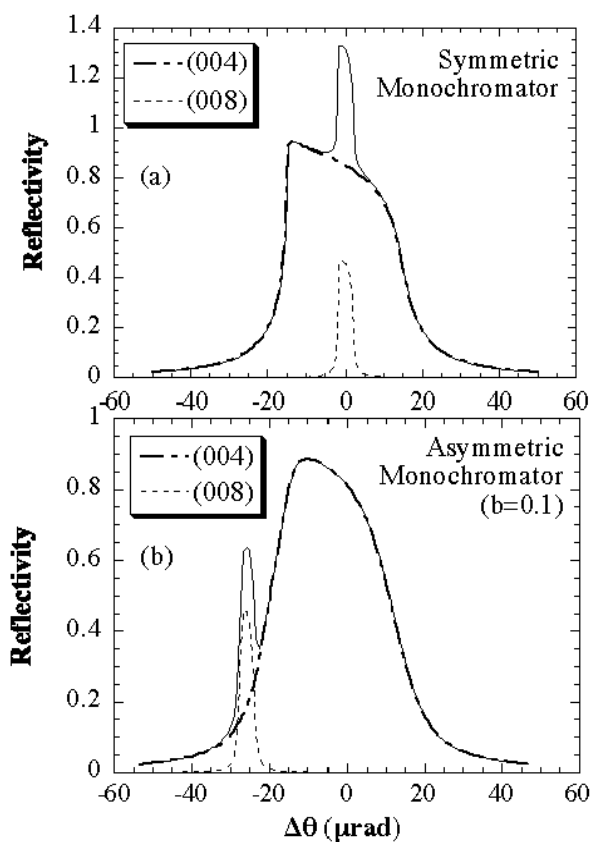


Table A.2 Part list for the electronic and mechanical control of the XSW experimental setup. (Referring to Fig. 3.5 and Fig. A.7)

Parts	Vendor information	Description
$\square_1$ ( $\square_b$ ) Turn Table	Huber 410 Goniometer.	Stepping motor (microstepper, 4000 steps / degree) driven Huber 410.
z2 Translation Stage	Huber.	Linear Stage.
y2 Translation Stage	Huber	Linear Stage.
Piezo Torsion Bearing Stage	Custom Design.	Custom designed torsion bearing stage to achieve fine angular adjustment. Level arm: 43 mm.
$\square_1$ ( $\square_2$ ) Crystal Tilt	Huber 1003 Goniometer head.	DC motor driven Huber head for tilt adjustment.
Piezo Translator	Physik Instrument P-840.20.	Low voltage piezo translator with strain gauge. Range: 15 microns.
Piezo Driver and Controller	Physik Instrument P-864.10 Driver/Amplifier and E-808 Controller.	Low voltage piezo driver and controller. Input: -2 V ~ 12 V. Output: -20 V ~ 120 V.
MOSTAB Unit	Custom Design. [69, 84]	Feedback controller for monochromator.
Ionization Chamber	Custom Design.	N <sub>2</sub> , He or air.

High Voltage Power Supply	EG&G Ortec Model 556.	High voltage supply for ion chambers.
Amplifier	Keithley Model 427.	Current amplifier for ion chambers and photodiodes. Gain: from $10^{-4}$ A/V to $10^{-11}$ A/V.
Amplifier	Graseby Optronics Model 101C (TRAMP).	Low noise AC (DC) current amplifier.
Si(Li) Detector	PGT Model LS 33175 Special Designed Fluorescence Detector.	Special designed Si(Li) detector. with 0.3 mil (8 microns) thick Be window. Detector crystal area 30 mm <sup>2</sup> . Energy resolution: 200 eV at 5.9 keV.
High Voltage Power Supply and LN <sub>2</sub> Monitor	PGT Model 315.	0-5keV HV bias supply and LN <sub>2</sub> monitor for Si(Li) detector.
Spectroscopy Amplifier	Tennelec/Nucleus TC244	Spectroscopy amplifier with pileup rejecter for Si(Li) detector.
Single Channel Analyzer	Tennelec/Nucleus TC452.	NIM Quad single channel analyzer.
Random Pulse Generator	Berkeley Nucleonics Corp. Model DB-2.	Random pulse generator to generate pulses for dead-time counting.

PCA-II Interface Card	Oxford Instrument / Nucleus PCA-II-8000.	Nucleus AT MCA (multi channel) interface card to store fluorescence spectra into computer. 8000 channels.
CAMAC Crate	KineticSystems Model 1502-P2H.	25-slot 52A powered CAMAC crate.
CAMAC Interface Card	DSP 6002 Interface and DSP PC004 Board.	With 6002 on CAMAC crate and PC004 on PC. Connected together by a ribbon cable.
Clock	Joerger Enterprises Model CG.	Clock generator.
Real Time Clock	DSP Technology Model RTC-018T	Real time clock, output 262,144 Hz.
Counter	KineticSystems 3610-L2A Hex Scaler.	6-channel, 50 MHz counter.
D/A Converter	KineticSystems 3112-M1A DAC.	8-channel, 12-bit D/A Converter.
Stepping Motor Interface Panel	DSP Technology Model E450 and E455.	4-channel optical isolator. Used with E500.
Stepping Motor Controller	DSP Technology Model E500.	8-channel stepping motor controller.
STEP PAK Stepping Motor Driver	Advanced Control Systems MDU-8.	8 axis stepping motor driver.

---

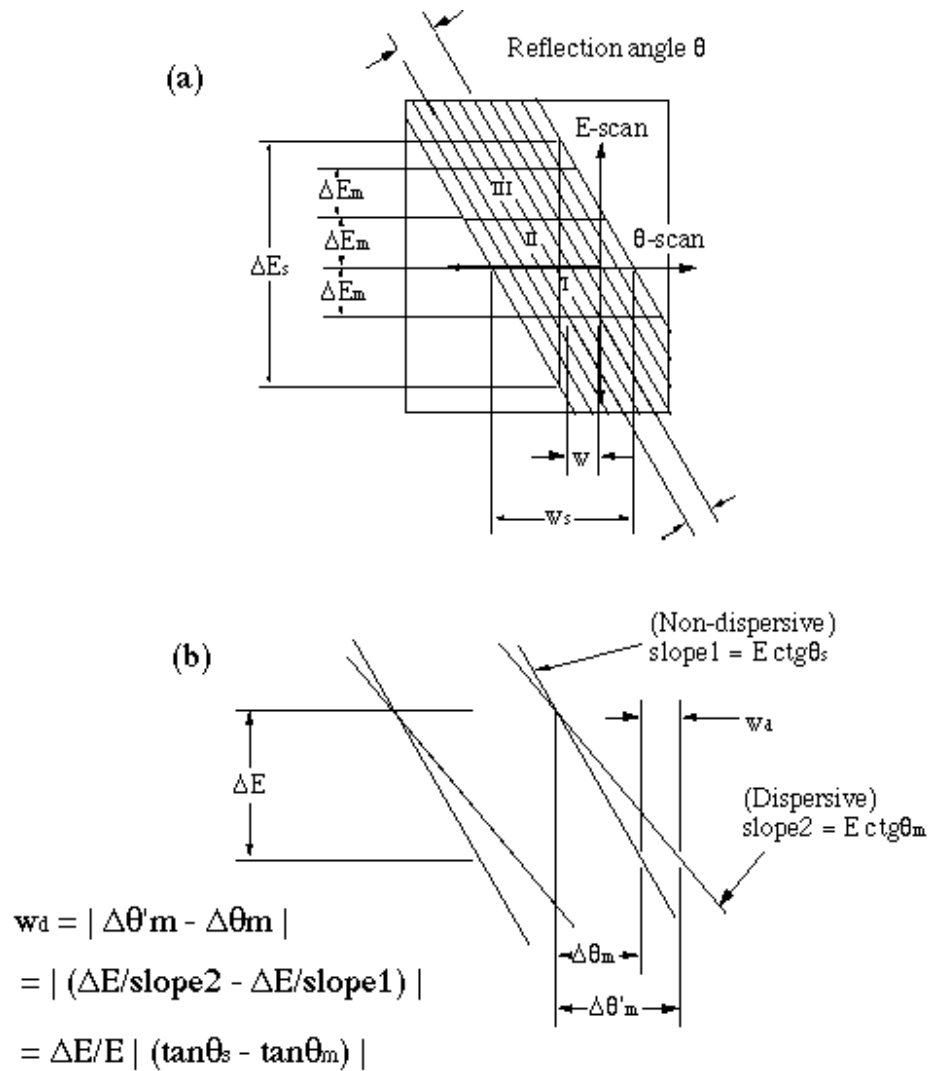
Stepping Motor	Advanced Control Systems	Power supply.
Power Supply	PSU-8.	
486 PC	Gateway 2000 DX2	Gateway 2000 486DX2-33MHz PC to run LINUX.

---

### A.3.2 Instrumental Resolution

High precision XSW measurements require a high resolution in phase contrast (or the fringe visibility  $V$ , defined by Eq. 3.1) of XSW E-field intensity.  $V$  ranges from zero to unity. Unity corresponds to the highest visibility and zero means no visibility. For an ideal  $\delta$ -function monochromator  $V = 1$ . Any actual monochromator has a certain angular resolution  $\Delta\theta$  associated with its intrinsic rocking curve width  $\theta$ . Any slight angular misalignment due to diffraction plane d-spacing mismatch between the sample and monochromator crystals will also contribute to  $\Delta\theta$  as dispersion. All these factors can reduce the fringe visibility of an XSW measurement and can make it less precise. It is convenient to discuss this with a DuMond diagram, which is an  $E$  vs.  $\theta$  plot for Bragg diffraction. As an example, Fig. A.9(a) illustrates a DuMond diagram for an XSW monochromator/sample arrangement. The sample is represented by a stripe with its angular width equal to the sample intrinsic rocking curve width  $\theta_s$ . The stripe contains a series of parallel lines with their slope equal to  $(-E \cot \theta_s)$  from the derivative of Bragg's law. Along each line within the stripe the XSW phase  $v(\theta, E)$  is constant. The shaded parallelogram I represents a non-dispersive (*i.e.* no d-spacing mismatch with the sample,  $\theta_m = \theta_s$ ) monochromator crystal with an intrinsic rocking curve width  $\theta$ . Each particular line with a constant value  $v(\theta, E)$  defines a particular location of XSW nodes and antinodes with respect to the diffraction planes. Scanning through all the equal-phase lines within the sample stripe is equivalent to a scan through the sample rocking curve or a sweep of the XSW antinodal planes by one half of a d-spacing. As can be seen clearly in the figure, this scan can be achieved by either scanning the monochromator  $\theta_m$  relative to the sample, which causes vertical movement in energy (E-scan), or scanning the sample  $\theta_s$  relative to the monochromator, which causes a horizontal angular movement of

Figure A.9 (a) A DuMond diagram illustrating the monochromator/sample arrangement for XSW measurement. The broad stripe represents the sample crystal reflection band and the thin lines within the stripe are the constant phase  $v(\theta, E)$  lines. The shaded parallelograms I, II and III represent the emittance from a nondispersive and two dispersive monochromators, respectively. (b) A DuMond diagram illustrating the angular width broadening due to the dispersion of the monochromator.



the sample ( $\omega$ -scan). A small  $\Delta v$  (the range of  $v$  values covered by the monochromator parallelogram) means good resolution in  $v(\omega, E)$  and high fringe visibility which improves spatial resolution. It is obvious that for a non-dispersive monochromator the phase resolution improves as  $\omega$  decreases relative to  $\omega_s$ . Also in the figure, two dispersive monochromators are represented by shaded parallelogram II (having a larger d-spacing or  $\omega_m < \omega_s$ ) and III (having a smaller d-spacing or  $\omega_m > \omega_s$ ). Obviously, both of these cases have a worse phase resolution ( $\Delta v < \Delta v'$ ) than the non-dispersive monochromator with the same intrinsic rocking curve width.

Based on the above discussion, a nondispersive monochromator should always be chosen over a dispersive one, if possible. For a perfect or near-perfect nondispersive single crystal, its phase resolution is based on its angular range  $\Delta\omega_m$ , which is primarily equal to the angular emittance width of the rocking curve. An asymmetrically cut crystal can provide a narrower emittance width. For grazing incidence  $|b| < 1$ , by Eq. 2.17b, the angular emittance width is reduced by a factor of  $\sqrt{|b|}$  relative to its symmetrical width. Usually, a  $|b|$  factor of about 25 is a typical value to choose for XSW experiments.

When a nondispersive monochromator arrangement is not available, a dispersive monochromator should be chosen with as small d-spacing mismatch as possible. The effective angular width  $\omega_d$  broadening (or effective b-factor) due to the dispersion can be estimated as following (see Fig. A.9(b)). For the nondispersive monochromator, the angular broadening of  $\Delta\omega_m$  corresponding to an energy range of  $\Delta E$  is equal to  $\Delta\omega_m = -\tan\omega_s \Delta E / E$ . For the dispersive one with the same rocking curve width, the angular range  $\Delta\omega_m$  corresponding to the same energy range is  $\Delta\omega_m = -\tan\omega_m \Delta E / E$ . The difference  $|\Delta\omega_m - \Delta\omega_m'|$  is the angular broadening due to the dispersion. :

$$\omega_d = |\Delta\omega_m - \Delta\omega_m'| = \frac{\Delta E}{E} |\tan\omega_s - \tan\omega_m|. \quad (\text{A.1})$$

$\Delta E$  is the energy band width of the x-ray source. At a rotating anode, it is equal to the natural width of the target x-ray line (*e.g.* Cu K $\alpha$ ). At a synchrotron radiation bending magnet beamline without any premonochromator or mirror (*e.g.* beamline X15A), the emittance x-ray energy width of the monochromator followed by a vertical slits is determined by

$$(\Delta E/E)_{\text{out}} = -\cot\theta_m \Delta\theta. \quad (\text{A.2})$$

As illustrated by the DuMond diagram in Fig. A.10,  $\Delta\theta = \sqrt{\theta_{\text{out}}^2 + \Delta\theta_s^2}$ , where  $\theta_{\text{out}}$  is the emittance width (Eq. 2.17(c)) of the asymmetric monochromator crystal and  $\Delta\theta_s$  is the source angular divergence due the vertical slits. We will assume that there are vertical slits smaller than the  $1/\theta$  ( $\sim 0.2$  mrad) opening angle of the bend magnet source. In this case, the source vertical angular divergence  $\Delta\theta_s$  is:

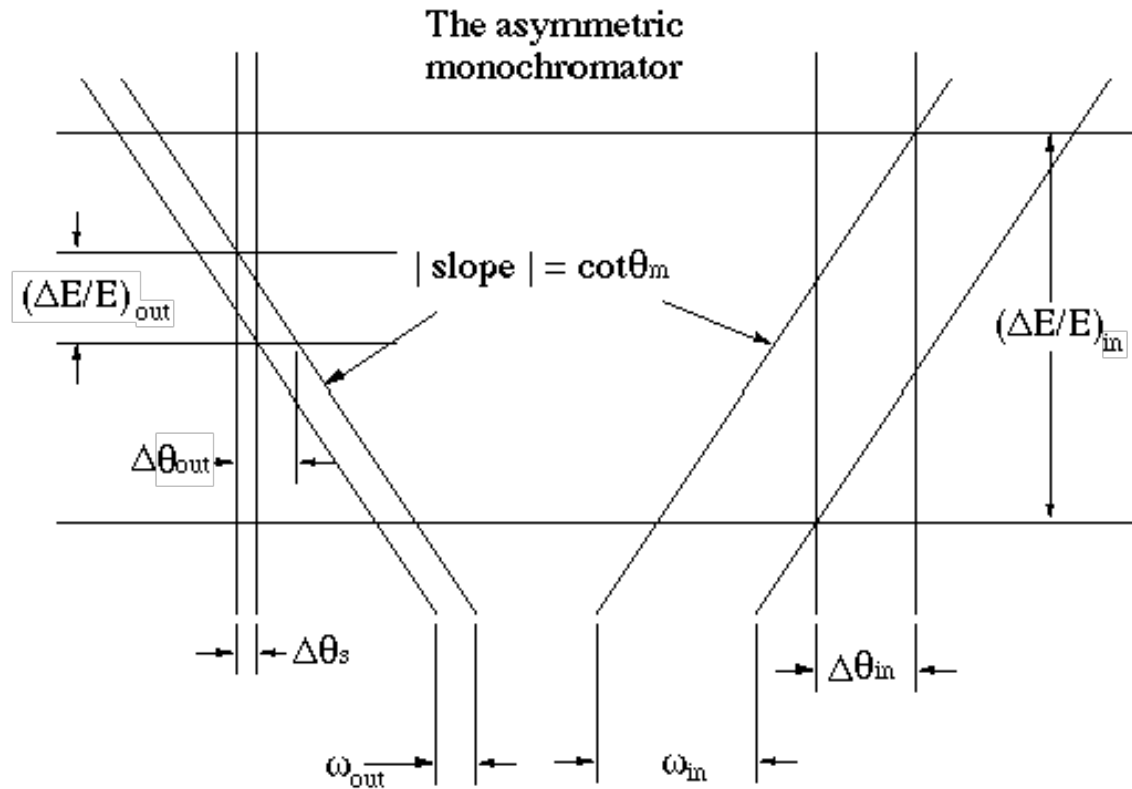
$$\Delta\theta_s = \frac{2\theta_{\text{source}} s_{\text{slit}}}{d_{\text{vs}}}, \quad (\text{A.3})$$

where  $2\theta_{\text{source}}$  is the source size,  $s_{\text{slit}}$  is the slit size,  $d_{\text{vs}}$  is the virtual source distance. At beamline X15A,  $d_{\text{vs}} \approx |b|^{-1} d_{\text{source}}$ , where  $d_{\text{source}}$  is the distance between the synchrotron source and the asymmetric monochromator crystal, and  $b$  is the asymmetry factor defined in Chapter II (Eq. 2.9).

At X15A, the typical source size is  $2\theta_{\text{source}} = 0.2$  mm, and the source distance is  $d_{\text{source}} = 17$  m. With a vertical slit size of 2 mm and a monochromator asymmetry of  $|b| = 0.025$ , the source divergence is then  $\Delta\theta_s \approx 6$   $\mu$ rad. At 12 keV, a Si(004) monochromator

with a b-factor of 0.025 has an emittance width of  $\sigma_{\text{out}} = 2 \text{ } \mu\text{rad}$ . Therefore, the energy resolution of this monochromator at 12 keV is 0.2 eV.

Figure A.10 A DuMond diagram illustrates the energy resolution of a monochromator followed by a slit at synchrotron radiation. The incoming source angular divergence  $\Delta\theta_{in}$  is normally limited by the incident aperture (which is determined by the length of the asymmetric monochromator crystal and the glancing incidence angle  $(\theta_B - \theta)$ ) and is usually smaller than the source divergence  $1/\lambda$ . The emittance energy width  $(\Delta E/E)_{out}$  is determined by the emittance angular width  $\Delta\theta_{out}$ , which is the sum of  $\Delta\theta_s$  and  $\theta_{out}$  (by adding quadratically).



## A.4 Procedure of XSW measurement

### A.4.1 Monochromator setup

Referring to Fig. A.7 and Table A.2, the monochromator setup procedure is described as following:

1. Close the He inlet and outlet gas valves to the monochromator box. Open the box to change the monochromator crystals.
2. Choose the appropriate monochromator crystals (*i.e.* matching d-spacing to sample crystal and choosing desired asymmetry for the first monochromator crystal).
3. Align the first monochromator crystal with the white x-ray beam.
4. Align the second monochromator by adjusting  $y_2$  and  $\chi_2$  to find reflection (by looking at the ion chamber reading or the reflection on a fluorescence screen). Adjust the tilt (DC motor driven Huber goniometer head) of the second crystal to make it parallel to the first crystal. Maximize the reflection intensity by adjusting  $y_2$ .
5. Close the monochromator box. Pump out the air in the box with the roughing pump and the turbo pump until the pressure is below 30 millitorr. Close the pumping valve and open the He inlet valve to backfill with He to reduce x-ray absorption by air and ozone pollution.. When the He is filled (the inside pressure is back to one atmosphere), open the outlet valve. Adjust He pressure to keep a smooth flow of He within the box.
6. Find the reflection by adjusting second crystal. Tune the MOSTAB unit to lock the second crystal at 80% of the maximum reflectivity on the left side of the rocking curve for fundamental reflections (see Appendix A.3.1 for more details).

7. Calibrate the energy of the monochromator by using a transmission foil with an absorption edge near the energy desired to tune to.

#### *A.4.2 Sample alignment*

Referring to Fig. 3.1 and Table A.1, the sample alignment procedure is described as following:

1. After obtaining the desired surface, transfer the sample on its holder into x-ray chamber through R2P2 chamber. Place the sample holder onto the sample manipulator stage. Make sure the sample holder is held tightly by the manipulator.

2. Turn off the cryopump. Close the valve between the x-ray chamber and R2P2 chamber. Turn off the ion gauge in the x-ray chamber and lights in the hutch. This gives the photodiode lowest dark current reading.

3. Align the sample with the incident x-ray beam from monochromator with the Si photodiode. With  $\theta$  at zero, adjust the z drive to center the sample surface with the incident beam. Then, scan the  $\theta$  drive to calibrate the zero angle. The photodiode reading should indicate that the beam is cut in half by the sample surface.

4. Move  $\theta$  and the photodiode  $2\theta$  to the desired angles. Adjust  $\theta$  to find the reflection.

5. Close down the entrance slits. Make sure that the incident beam only hits the sample.

6. Adjust the sample tilt ( $\chi$ ) to make the sample diffraction planes parallel to that of the monochromator crystals.

7. Do a rocking curve scan of the sample crystal by scanning the piezo of the first monochromator crystal with the second monochromator crystal locked at 80% tune

by the MOSTAB. Compare the FWHM and the maximum reflectivity to theory (see Chapter II) and make sure the rocking curve is good.

### *A.4.3 XSW measurement*

Referring to Fig. 3.1, 3.5, 3.6 and Table A.1:

1. Lower the Si(Li) detector snout to bring it as close to the sample as possible.
2. Slowly turn up the voltage of the high voltage power supply for the Si(Li) detector to -600 V. Make sure the detector is working properly.
3. Set appropriate gain and shaping time (4  $\mu$ sec) for the spectroscopy amplifier. Make sure that all fluorescence peaks of interest are included in the MCA spectrum. Set the LLD of the MCA card just above the noise threshold ( $\sim 0.1$  V).
4. Turn on the random pulse generator. Set and record the count rate (frequency, typically 1000 cps).
5. Set up parameters for XSW.MAC macro. Then start the XSW scan.
6. When the scan finishes, calibrate the absolute reflectivity of the sample by measuring the straight through incident intensity with the photodiode.

## *A.5 Coverage Calibration*

### *A.5.1 By AES*

The way to calibrate the adsorbate coverage by Auger electron spectroscopy is to compare the Auger peak-to-peak amplitude of the unknown coverage surface to a

standard surface (coverage known). If the Auger peak-to-peak amplitude of the adsorbate A (coverage  $C_A$  unknown) is  $I_A$ , the Auger peak-to-peak amplitude of the adsorbate B from a standard surface with a known coverage  $C_B$  is  $I_B$ , the coverage  $C_A$  can then be calibrated by:

$$C_A = \frac{I_A S_B}{I_B S_A} C_B . \quad (\text{A.4})$$

$S_A$  and  $S_B$  are the relative Auger sensitivity for element A and B.

#### A.5.2 *By x-ray fluorescence yield*

Another way to calibrate coverage is to compare the off-Bragg x-ray fluorescence yield from the adsorbate with an unknown coverage to the fluorescence yield from a standard sample (implanted species with a well calibrated coverage). The off-Bragg x-ray fluorescence yield from a surface (or near surface) adsorbate with the Si(Li) detector solid angle of  $\Delta\Omega$  can be described as:

$$Y = I_0 \sigma \Gamma r_f \Delta\Omega , \quad (\text{A.5})$$

where absorption is ignored.  $I_0$  is the incident photon intensity.  $\Gamma$  is the adsorbate coverage.  $\sigma$  is the photoelectric effect cross-section and can be calculated by CROMER (see Appendix B).  $\Gamma$  is the fluorescence yield. For K or L shells fluorescence yield, see Ref. [67].  $r_f$  is the relative x-ray emission rate [108]. Therefore, the adsorbate coverage can be calibrated by:

$$\eta = \frac{Y}{Y_S} \frac{(I_0 \mu_{\text{eff}})_S}{\mu_{\text{eff}}} \eta_S \quad . \quad (\text{A.6})$$

The subscript S stands for the standard sample. Eq. A.6 is based on the assumption that the fluorescence detector has the same solid angle  $\Delta\Omega$  for fluorescence signals from both sample surfaces. This requires a careful alignment of samples and the Si(Li) detector.

## Appendix B XSW Data Analysis Software Package

Before describing the XSW data analysis software packages (namely, SUGO and DARE), a few other software packages which are generally very useful for x-ray optics, scattering and absorption deserve a brief introduction.

PHOTON: Photon is a FORTRAN program developed by Chapman *et al.* [34]. It calculates synchrotron spectra of photon radiation generated by bending magnet and wiggler beamlines through a definable set of apertures and windows.

URGENT: Urgent [127] is a FORTRAN program that calculates the basic properties (angular, spectral, polarization, and power density) of the radiation generated in ideal plane, helical or elliptical undulators.

CROMER: Cromer is a FORTRAN program that calculates anomalous dispersion corrections  $\Delta f'$ ,  $\Delta f''$  and absorption coefficient  $\mu$  for any element at any photon energy between 1 and 100 keV.

SPEC: SPEC [32] is a UNIX-based software package develop in C. It is specially designed for instrumental control (stepping motors, piezo through D/A converter) and data acquisition (interfacing with SCA, MCA) for x-ray diffraction experiments. SPEC supplies a programmable macro language allowing users to develop

their own macros running under the SPEC shell. The experimental control routine for XSW measurements in this thesis was developed using the SPEC macro language.

### *B.1 Raw data file*

The raw data file generated by the XSW.MAC macro contains a fileheader and one or more savesets of data. The fileheader stores important information such as the time when the XSW measurement starts, a brief description of the measurement, and starting position of stepping motors.

Depending on how long the XSW measurement takes, the data can be stored in several savesets. Usually, one saveset contains data of every 50 (or 100) scans. By having more than one saveset, one can avoid the risk of losing all of the data if something goes wrong during the measurement. Data stored in each saveset has the same format: a 2-dimensional array. Columns represent angular steps of XSW scans. Typically, each scan has 32 steps. Each row of the 2-D data array corresponds to a channel of a multi-channel spectrum (or MCA data). For a 32-step XSW scan, the total number of channels is 512 (from 0 to 511).

The first 8 channels (rows) of the MCA data are dedicated to single-channel data from the counters (see Fig. 3.5). Channel 0 is reserved for Real Time Clock. Channel 1 is reserved for the ion chamber IC2. Channel 2 stores the reflectivity data collected by the *in vacuo* photodiode. Channel 3 and 4 are reserved for single-channel analyzer (SCA) data. Channel 5 stores the NSLS ring current. Channel 6 and 7 are user definable. The rest 504 channels (from 8 to 511) store MCA data recorded by the energy-dispersive Si(Li) detector.

## *B.2 Data reduction: SUGO*

### *B.2.1 Input of raw data*

SUGO is a data reduction program that reads in the XSW raw data file and extracts the necessary data files that will be used for creating the experimental x-ray reflectivity and fluorescence yield (described in next section). SUGO was originally developed in FORTRAN on MicroVAX. Versions of SUGO running on UNIX and Macintosh are currently under development.

To read in the XSW raw data file, run SUGO under the directory where the raw data file is stored by typing "sugo". You are asked to give the name of the raw data file:

```
      ** S U G O **          VERS. 15-Jun-93
(XSW.DAT) Enter MCA File name ==>
```

Then the number of steps and the number of channels per step will be asked by the program:

```
( 32) Total number of steps? ==>
( 512) Number of channels per step? ==>
```

Default answers (by hitting return) are "32" and "512". Otherwise, give actual numbers used in your XSW scan. Then you will be prompted by the program:

```
Save Set #1  Fri Nov 4 12:29:02 1994
() Read in this set? (Y/N/A/E(sc)) ==>
```

Type "Y" if you want to read in this saveset. Type "N" if you do not want this saveset. When you type "A", the program will automatically read in ALL savesets within the data file. Type "E" if you do not want this data file at all.

If you want to add another data file to the file that you just read in, type "AF" (uppercase is necessary when you type commands in SUGO). If you do not like the data file that you just read in, you can type "NF" to start reading in a new data file.

### *B.2.2 Data reduction*

SUGO has different functions allowing you to extract total counts, to add peak areas with or without background corrections and to fit Gaussian to multiple peaks with background corrections. Type "/", and you can get an on-line help screen to summarize all commands used by SUGO:

#### INPUT:

SG : OUTPUT CHANNEL CONTENTS  
TO : TOTAL counts in WINDOW OF UP TO 0 SGS  
NF : READ IN A NEW DATA FILE  
AF : ADD IN A NEW DATA FILE  
// : EXIT  
G1 : 1 GAUSS PEAK + QUADR. BG  
G2 : 2-4 GAUSS PEAKS + QUADR. BG  
AD : ADD SUBGROUPS  
AR : SIMPLE AREA CALCULATION

The output file from SUGO is a specially-formatted 3-column file with an extension ".DA3". The three columns are "X", "Y" and " $\Delta Y$ ". Usually, the "X" column contains the angular step number (typically 1 to 32). The "Y" column contains the net counts (reflectivity, fluorescence, clock, etc.) and " $\Delta Y$ " is the statistical error of "Y".

For the analysis in DARE, the following information and ".DA3" files are needed from SUGO: real time, ion chamber IC2 counts, reflectivity counts, pulser counts, and fluorescence counts from peaks of interest.

(a) Real time

The real time is stored in channel 0 of the raw data file. To extract this information, use the "TO" command. The real time is used to normalize the single channel data such as the ion chamber and the reflectivity. Usually, real time is the same for every step. You can simply write down the number. The ".DA3" output file is not necessary.

(b) Ion chamber counts

The total counts from the ion chamber IC2 is stored in channel 1. Use the "TO" command to extract the ".DA3" output file for IC2. This file is used to normalize the reflectivity and fluorescence counts to compensate the incident x-ray intensity drop due to the decrease of the synchrotron ring current.

(c) Reflectivity

The reflectivity is stored in channel 2. Use the "TO" command to extract the ".DA3" output file for reflectivity. This is used for DARE to fit the rocking curve.

(d) Pulser

The pulser is an artificial peak in the fluorescence spectrum. It is generated by a random pulse generator and input into Si(Li) detector through its preamplifier. It is used to count the electronic "dead time" of the detector system (when the input count rate is high, the electronic system is not 100% efficient). Use the "TO" or the "AR" command to extract the total or net counts of pulser and output to a ".DA3" file.

(e) Fluorescence

For a perfect detector, fluorescence signals should appear as separated lines with a width of a few eV. Due to the finite energy resolution of the Si(Li) detector (typically 200 eV), these lines are broadened into peaks. Statistically, these peaks can be assumed to have a Gaussian distribution. Therefore, the net counts of each peak can be extracted by fitting a Gaussian to each peak. SUGO can do a single (one peak) Gaussian fit ("G1") and multiple (up to four peaks) Gaussian fit ("G2"). The following standard procedure is recommended when performing "G1" or "G2":

1. Use the "AD" command to add the spectra of the 32 steps together to get a sum spectrum. Then use "G1" (or "G2") to fit the region containing the peak(s) of interest. Let all fitting parameters be free. Get a best fit of the AD spectrum.

2. Use the value for peak position(s) and peak width(s) obtained from the fit in step 1 and fix these parameters. (Physically, peak positions and widths should be constants since they represent fluorescence photon energy and detector resolution.) Then perform the "G1" (or "G2") fit to each step and output this set of 32 Gaussian areas to a ".DA3" file.

3. For a "G2" fit of a set of lines from the same element you can further reduce the number of free parameters by fixing the relative areas for the peaks.

Quit SUGO by typing "/" when you finish.

### *B.3 Data analysis: DARE*

DARE is the program that fits convoluted dynamical diffraction theory curves (see Chapter II) to the experimental rocking curve and fluorescence yield curve data (".DA3" files output from SUGO). DARE was originally developed in FORTRAN on MicroVAX. Versions of DARE running on UNIX and Macintosh are currently under development.

Type "DARE" under the directory where you stored all the ".DA3" files generated by SUGO. You should see:

```
V: 24-Nov-86
***** D A R E *****
5-SEP-95
I AM
```

```
**READY
```

To see the on-line help screen, hit return:

ANSWER:

RO - ROCKINGCURVE-FIT  
 FO - FLUORESCENCE-FIT(FAST)(FO-1:EXP. ROCKINGC.)  
 F1 - FLUORESCENCE-FIT

(SPECIAL) OPTIONS:

--  
 RP - FIT-ROUTINES PARAMETER ARE SHOWN AND MAY BE  
 ALTERED  
 FP - YOU MAY ENTER FIT-PARAMETER <---SP  
 CR - CALCULATION OF CHI-VAL., REFLECTIONCURVES  
 RF - RUN FUMILI(PAR.&DATA?) <---SP  
 EC - THE PROGRAM ASKS FOR EXPERIMENTAL PARAMETER <---SP  
 FF - YOU MAY RUN A FLUORESCENCE-FIT <---SP  
 AB - LEAVE FLUORESCENCE-FIT MODE <---SP  
 RD - READ DATA FOR A FIT FROM FLOPPY <---SP  
 RO - ROCK.-CURVE AND CONSTANTS FOR A FLUORESCENCE-FIT  
 <---SP ARE TAKEN FROM A .ROC-FILE  
 MA - MANIPULATE A .DA3 FILE  
 DD - DISPLAY A .DA3-FILE (DD-3 FOR 2nd plot)  
 (VERSION: JAN 84)

The command "CR" is the one to use to calculate all of the pertinent parameters for a user defined crystal reflection.

### *B.3.1 Data Manipulation*

The reflectivity and fluorescence yield ".DA3" files need to be normalized and (live-time) corrected before being fit to the dynamical theory. Type "MA", you will be prompted by a screen like this:

**COMMANDS:**

\*\*\*\*\*

```
1 : FILE 1 * X
2 : FILE 1 + X
3 : FILE 1 / X
4 : FILE 1 - X
5 : FILE 1 * FILE 2
6 : FILE 1 + FILE 2
7 : FILE 1 / FILE 2
8 : FILE 1 - FILE 2
-1 : FILE 1 ERRORS * X
-2 : file 1 errors = sqrt(y)
9 : INVERT X-SCALE
```

These commands manipulate ".DA3" files. For example, typing "1" multiplies "FILE1.DA3" by a number "X".

(a) Incident flux normalization

The incident photon flux from the monochromator decreases due to the decrease of the NSLS current (dropping from 250 mA to 110 mA in 16 hours) over the time of experiments. This can be normalized by the ion chamber IC2 readings as following:

1. The IC2 total count ".DA3" file generated by SUGO needs to be divided (command "3") by "real time".
2. The output file of step 1 is divided by (command "3") the IC2 counts per second at 200 mA current recorded during the experiment.

This generates a normalized IC2 ".DA3" file (to 200 mA NSLS current and to a certain slit setting).

(b) "Dead time" correction

As mentioned above, at high count rate the electronic system is not 100% efficient. There is a certain amount of time ("dead time") when the detector system is inhibited from counting. To correct this effect, an artificial signal called "Pulser" with a known frequency (or count rate) is included in the MCA spectrum. The total counts of "Pulser" is extracted by SUGO and output into a ".DA3" file. To correct the "dead time" effect and to normalized fluorescence yields correctly, the actual counting time ("live time") of the detector system is calculated by dividing (command "3") the "Pulser" total count ".DA3" file with the Pulser input frequency. This generates a "live time" ".DA3" file.

(c) Reflectivity normalization

The reflectivity ".DA3" file generated by SUGO is normalized by the following steps:

1. Divide (command "3") the reflectivity ".DA3" file by "real time" first.
2. Then divide (command "7") the output of step 1 by the normalized IC2 ".DA3" file obtained in procedure (a).
3. Divide the result of step 2 by the straight through counts per second at 200 mA.

This generates the normalized reflectivity ".DA3" file used to fit the rocking curve.

(d) Fluorescence yield normalization

The fluorescence yield is normalized by the following steps:

1. The "dead time" correction: Divide (command "7") the fluorescence ".DA3" file by "live time" ".DA3" file first.
2. Then divide (command "7") the output file of step 1 by the normalized IC2 ".DA3" file.

This generates the normalized ".DA3" file used to fit fluorescence yield.

*B.3.2 Rocking curve fit*

Part of the DARE program calculates the theoretical rocking curve according to dynamical diffraction theory (see Chapter II) and performs a non-linear  $\chi^2$  fit to the normalized reflectivity data. The fitting parameters are: the absolute reflectivity, the angle scale offset and the angular range of the rocking curve scan. In order to calculate the rocking curve for different crystals, DARE reads in the necessary information such as the atomic form factors from "ELT\*\*".SCT" files. Different "ELT\*\*".SCT" files correspond to different materials. "ELT01.SCT" is for Si substrate, "ELT02.SCT" is for Ge substrate. Make sure to have the correct "ELT\*\*".SCT" file in the same directory with the raw data and SUGO generated ".DA3" files.

(a) "RP" --- Fit routine parameter setup

Type "RP" to set up fitting parameters for the non-linear  $\chi^2$  fit routine. Most of parameters can be set as the default. There are some parameters that require to be set up accordingly. They are:

N3: number of iterations. It tells DARE how many iterations to perform before stopping. Usually, it is set to be 20. Note, if return is hit without any number specified, N3 will be set as 0.

ISSE: type of error assumed during the fitting. 0 stands for statistical error and 1 stands for systematic error. Typically, systematic error is assumed for rocking curve fit and statistical error is assumed for fluorescence fit.

YFIN: angular range in terms of rocking curve width used in convolution. It is typically set to be 2.5.

IRF: points for convolution (from 1 to 128). Typically, it is set to be 40. (*i.e.* the emittance curve from the asymmetric monochromator is calculated for 40 points over the range of  $-2.5 < \theta < 2.5$ .)

NDSP: number of points for dispersion spread. Choose 0 for the non-dispersive case. Calculate the corresponding value for dispersive cases by the formula:

$$NDSP = \frac{X(IRF \cdot \Delta\theta)}{\Delta\theta \cdot YFIN \cdot \Delta\theta} \quad , \quad (B.1)$$

where

$$X = \frac{(1 - \tan^2 \theta_s / \tan^2 \theta_m) SS}{SD \theta_m}, \quad (\text{B.2})$$

SS and SD are the source size and source distance (see section A.3.1).

(b) "R0" --- Rocking curve fit

Type "R0" to start fitting the rocking curve. First you will be asked for the name of the input data file (the normalized ".DA3" file generated in subsection B.3.1(c)):

/DATA/

??FILE (EXT=.DA3)

After typing the file name (without the ".DA3" extension), the type of monochromator will be asked:

/DATA MONOCHROMATOR(SILICON=1, GERMANIUM=2)/

Currently, two types of monochromator (Si and Ge) are supported by DARE. Then you need to specify the (hkl) and b-factor for the monochromator. For an ideal non-dispersive monochromator, the b-factor is estimated by Eq. 2.9, only accounting for the asymmetric reflection. For the dispersive case, the effective b-factor accounts for both asymmetry and dispersion:

$$b_{\text{eff}} = [ \sqrt{b} + \theta_d / \theta_m(\text{sym}) ]^2 . \quad (\text{B.3})$$

$\Delta_d$  is defined by Eq. A.1 in Appendix A.

For a real monochromator, thermal strains, defects in the crystal, and mechanical vibrations can contribute the angular broadening of the emittance. This can result in a slight broadening of the sample rocking curve. In order to compensate for these effects, the real b-factor obtained for the best fit of rocking curve is typically slightly larger than the value based on asymmetry and dispersion.

After the b-factor input, you need to input the crystal choice for the sample. It can be either elements (*e.g.* "1" for Si) or compounds (*e.g.* "4,5" for GaAs). You then need to specify the incident photon energy, the (hkl), and the angular sweep range of the piezo drive (in microrad). Then DARE starts the non-linear  $\chi^2$  fit.

Keep adjusting the b-factor until the best fit is obtained. The best fit has two criteria: the smallest  $\chi^2$  value and best match between experimental and calculated values for absolute reflectivity and angular width. Once the best fit is achieved, two output files need to be generated: the best fit ".DA3" file and a ".RCF" file which is used in the fluorescence fit described in next subsection.

### *B.3.3 Fluorescence fit*

To fit the fluorescence yield, type "RP" to change the fitting parameters. Normally, only one parameter needs to be changed: ISSE. Change ISSE from 1 to 0 to use statistical errors for the fluorescence yield fitting.

To start the fluorescence fit, type "F1". You will be asked for the name of the normalized fluorescence yield data file (the ".DA3" file generated by SUGO and normalized in subsection B.3.1(d)) and the rocking curve file (the ".RCF" file generated

by rocking curve fit in DARE). Then you will make initial guesses for the two fitting parameters --- coherent fraction and coherent position.

Answer "N" (No) to the question "FIT OFFSET(Y/N)". For the case of fluorescent species at surface (*e.g.* Ga in the case of Ga/Si(001)), choose "0" for no attenuation correction. For the case of fluorescent species uniformly distributed through bulk (*e.g.* Si in the case of Ga/Si(001)), choose "1" for attenuation correction. In this case you also need to tell DARE the energy and take-off angle (see Fig. 3.6) of the outgoing fluorescence.

From the best fit of the fluorescence yield, three fitting parameters are obtained as the final results. They are the coherent fraction  $f_H$ , the coherent position  $P_H$  and the off-Bragg normalized fluorescence yield  $Y_{OB}$ .

## References

- [1] S. Aduru and J. W. Rabalais, *Surf. Sci.* **205**, 269 (1988).
- [2] O. L. Alerhand and E. J. Mele, *Phys. Rev. B* **35**, 5533 (1987).
- [3] O. L. Alerhand, J. D. Joannopoulos and E. J. Mele, *Phys. Rev. B* **39**, 12622 (1989).
- [4] T. W. Barbee and W. K. Warburton, *Mater. Lett.* **3**, 17 (1984).
- [5] S. A. Barnett, H. F. Winters and J. E. Greene, *Surf. Sci.* **165**, 303 (1986).
- [6] A. A. Baski, J. Nogami and C. F. Quate, *J. Vac. Sci. Technol. A* **8**, 245 (1990).
- [7] A. A. Baski, J. Nogami and C. F. Quate, *J. Vac. Sci. Technol. A* **9**, 1946 (1991).
- [8] I. P. Batra, *Phys. Rev. B* **41**, 5048 (1990).
- [9] B.W. Batterman and H. Cole, *Rev. Mod. Phys.* **36**, 681 (1964).
- [10] B. W. Batterman, *Phys. Rev.* **133**, A759 (1964).
- [11] B. W. Batterman, *Phys. Rev. Lett.* **22**, 703 (1969).
- [12] M. J. Bedzyk, G. Materlik and M. V. Kovalchuk, *Phys. Rev. B* **30**, 2453 (1984).
- [13] M. J. Bedzyk and G. Materlik, *Phys. Rev. B* **31**, 4110 (1985).
- [14] M. J. Bedzyk and G. Materlik, *Phys. Rev. B* **32**, 6456 (1985).
- [15] M. J. Bedzyk, D. H. Bilderback, G. M. Bommarito, M. Caffrey and J. S. Schildkraut, *Science* **241**, 1788 (1988).
- [16] M. J. Bedzyk, G. M. Bommarito and J. S. Schildkraut, *Phys. Rev. Lett.* **62**, 1376 (1989).
- [17] D. K. Biegelsen, F. A. Ponce, A. J. Smith and J. C. Tramontana, *J. Appl. Phys.* **61**, 1856 (1987).

- [18] D. K. Biegelsen, R. D. Bringans, J. E. Northrup and L. E. Swartz, *Appl. Phys. Lett.* **57**, 2419 (1990).
- [19] G. Binnig and H. Rohrer, *Surf. Sci.* **126**, 236 (1993).
- [20] M. Born and E. Wolf, *Principles of Optics, 2nd Ed.*, Macmillan, New York (1964).
- [21] G. Borrmann, *Phys. Z.* **42**, 157 (1941).
- [22] B. Bourguignon, K. L. Carleton and S. R. Leone, *Surf. Sci.* **204**, 455 (1988).
- [23] B. Bourguignon, R. V. Smilgys and S. R. Leone, *Surf. Sci.* **204**, 473 (1988).
- [24] R. D. Bringans, M. A. Olmstead, R. I. G. Uhrberg and R. Z. Bachrach, *Appl. Phys. Lett.* **51**, 523 (1987).
- [25] R. D. Bringans, M. A. Olmstead, R. I. G. Uhrberg and R. Z. Bachrach, *Phys. Rev. B* **36**, 9569 (1987).
- [26] R. D. Bringans, M. A. Olmstead, F. A. Ponce, D. K. Biegelsen, B. S. Krusor and R. D. Yingling, *J. Appl. Phys.* **64**, 3472 (1988).
- [27] R. D. Bringans, D. K. Biegelsen and L.-E. Swartz, *Phys. Rev. B* **44**, 3054 (1991).
- [28] R. D. Bringans, D. K. Biegelsen, J. E. Northrup and L.-E. Swartz, *Jpn. J. Appl. Phys.* **32**, 1484 (1993).
- [29] R. Cao, X. Yang, J. Terry and P. Pianetta, *Appl. Phys. Lett.* **61**, 2347 (1992).
- [30] M. J. Cardillo and G. E. Becker, *Phys. Rev. B* **21**, 1497 (1980).
- [31] M. J. Cardillo and W. R. Lambert, *Surf. Sci.* **168**, 724 (1986).
- [32] Certified Scientific Software, *SPEC, X-Ray Diffraction Software*, Certified Scientific Software (1990).
- [33] D. J. Chadi, *Phys. Rev. Lett.* **43**, 43 (1979).
- [34] D. Chapman, N. Gmur, N. Lazarz and W. Thomlinson, *Nucl. Instr. and Meth. Phys. Res. A* **266**, 191 (1988).

- [35] P. H. Citrin, *J. Phys.* **47**, 437 (1986).
- [36] M. Copel, M. C. Reuter, E. Kaxiras and R. M. Tromp, *Phys. Rev. Lett.* **63**, 632 (1989).
- [37] M. Copel, M. C. Reuter, M. Horn von Hoegen and R. M. Tromp, *Phys. Rev. B* **42**, 11682 (1990).
- [38] P. L. Cowan, J. A. Golovchenko and M. F. Robbins, *Phys. Rev. Lett.* **44**, 1680 (1980).
- [39] J. Dabrowski and M. Scheffler, *Appl. Surf. Sci.* **56-58**, 15 (1992).
- [40] R. S. Daley and R. S. Williams, *Nucl. Instrum. Meth. Phys. Res. B* **45**, 380 (1990).
- [41] C. G. Darwin, *Phil. Mag.* **27**, 315, 675 (1914).
- [42] D. J. Eaglesham and M. Cerullo, *Phys. Rev. Lett.* **64**, 1943 (1990).
- [43] D.J. Eaglesham, F.C. Unterwald and D.C. Jacobson, *Phys. Rev. Lett.* **70**, 966 (1993).
- [44] Y. Enta, S. Suzuki and S. Kono, *Phys. Rev. Lett.* **65**, 2704 (1990).
- [45] P. D. Ewald, *Ann. Phys.* **54**, 519 (1917).
- [46] W. C. Fan, N. J. Wu and A. Ignatiev, *Phys. Rev. B* **45**, 14167 (1992).
- [47] H. H. Farrell, F. Stucki, J. Anderson, D. J. Frankel, G. J. Lapeyre and M. Levinson, *Phys. Rev. B* **30**, 721 (1984).
- [48] L. C. Feldman, J. W. Mayer and S. T. Picraux, *Materials Analysis by Ion Channeling*, Academic Press, New York, (1982).
- [49] G. E. Franklin, E. Fontes, Y. Qian, M. J. Bedzyk, J. A. Golovchenko and J. R. Patel, *Phys. Rev. B* **50**, 7483 (1994).
- [50] G. E. Franklin, S. Tang, J. C. Woicik, M. J. Bedzyk, A. J. Freeman and J. A. Golovchenko, *Phys. Rev. B* **52**, R5515 (1995) .

- [51] J. A. Golovchenko, J. R. Patel, D. R. Kaplan, P. L. Cowan and M. J. Bedzyk, *Phys. Rev. Lett.* **49**, 560 (1982).
- [52] M. W. Grant, P. F. Lyman, J. H. Hoogenraad and L. E. Seiberling, *Surf. Sci.* **279**, L180 (1992); private communication.
- [53] R. J. Hamers, R. M. Tromp and J. E. Demuth, *Phys. Rev. B* **34**, 5343 (1986).
- [54] R. J. Hamers, R. M. Tromp and J. E. Demuth, *Surf. Sci.* **181**, 346 (1987).
- [55] T. Hanada and M. Kawai, *Surf. Sci.* **242**, 137 (1991).
- [56] M. A. Herman and H. Sitter, *Molecular Beam Epitaxy, Fundamentals and Current Status*, Springer-Verlag, Berlin (1989).
- [57] M. Horn-von Hoegen, A. Al Falou, B. H. Muller, U. Kohler, L. Andersohn, B. Dahlheimer and M. Henzler, *Phys. Rev. B* **49**, 2637 (1994).
- [58] T. Ide, T. Nishimori and T. Ichinokawa, *Surf. Sci.* **209**, 335 (1989).
- [59] A. Ishizaka and Y. Shiraki, *J. Electrochem. Soc.* **133**, 666 (1986).
- [60] H. Itoh, J. Itoh, A. Schmid and T. Ichinokawa, *Phys. Rev. B* **48**, 14663 (1993).
- [61] G. Jayaram, P. Xu and L. D. Marks, *Phys. Rev. Lett.* **71**, 3489 (1993).
- [62] N. Jedrecy, M. Sauvage-Simkin, R. Pinchaux, J. Massies, N. Greiser and V. H. Etgens, *Surf. Sci.* **230**, 197 (1990).
- [63] JEOL, *Application Data*, JEOL, Japan (1995).
- [64] B. A. Joyce, *Rep. Prog. Phys.* **48**, 1637 (1985).
- [65] A. Kawazu, T. Otsuki and G. Tominaga, *Jpn. J. Appl. Phys.* **20**, 553 (1981).
- [66] J. Knall, J.-E. Sundgren and J. E. Greene, *Appl. Phys. Lett.* **45**, 689 (1984).
- [67] M. O. Krause, *J. Phys. Chem. Ref. Data* **8**, 307 (1979).
- [68] H. Kroemer, *J. Cryst. Growth* **81**, 193 (1987).
- [69] A. Krolzig, G. Materlik, M. Swars and J. Zegenhagen, *Nucl. Instr. Meth.* **219**, 430 (1984).

- [70] N. Kuwata, T. Asai, K. Kimura and M. Mannami, *Surf. Sci.* **143**, L393 (1984).
- [71] M. G. Lagally, *Jpn. J. Appl. Phys.* **32**, 1493 (1993).
- [72] E. Landemark, C. J. Karlsson, Y.-C. Chao and R. I. G. Uhrberg, *Phys. Rev. Lett.* **69**, 1588 (1992).
- [73] M. von Laue, *Exakt. Naturwiss.* **10**, 133 (1931).
- [74] F. K. LeGoues, M. Copel and R. Tromp, *Phys. Rev. Lett.* **63**, 1826 (1989).
- [75] F. K. LeGoues, M. Copel and R. Tromp, *Phys. Rev. B* **42**, 11690 (1990).
- [76] V. G. Lifshits, A. A. Saranin and A. V. Zotov, *Surface Phases on Silicon*, John Wiley & Sons, Chichester (1994).
- [77] M. Lohmeier, H. A. van der Vegt, R. G. van Silfhout, E. Vlieg, J. M. C. Thornton, J. E. Macdonald and P. M. L. O. Scholte, *Surf. Sci.* **275**, 190 (1992).
- [78] K. Lonsdale, Ed., *International Tables for x-ray Crystallography III*, Kynoch, Birmingham (1968).
- [79] P. F. Lyman, Y. Qian and M. J. Bedzyk, *Surf. Sci.* **325**, L385 (1995).
- [80] P. F. Lyman, Y. Qian, T. L. Lee and M. J. Bedzyk, *Physica B*, in press.
- [81] L. D. Marks, *Rep. Prog. Phys.* **57**, 603 (1994).
- [82] R. E. Martinez, E. Fontes, J. A. Golovchenko and J. R. Patel, *Phys. Rev. Lett.* **69**, 1061 (1992).
- [83] G. Materlik and V. O. Kostroun, *Rev. Sci. Instrum.* **51**, 86 (1980).
- [84] G. Materlik and J. Zegenhagen, *Phys. Lett. A* **104**, 47 (1984).
- [85] A. Mazur and J. Pollmann, *Surf. Sci.* **225**, 72 (1990).
- [86] R. A. Metzger and F. G. Allen, *J. Appl. Phys.* **22**, 423 (1983).
- [87] Y. W. Mo, *Phys. Rev. Lett.* **69**, 3643 (1992).
- [88] J. Nogami, S. Park and C. F. Quate, *Appl. Phys. Lett.* **53**, 2086 (1988).
- [89] J. Nogami, A. A. Baski and C. F. Quate, *J. Vac. Sci. Technol. A* **8**, 3520 (1990).

- [90] J. Nogami, A. A. Baski and C. F. Quate, *Phys. Rev. B* **44**, 1415 (1991).
- [91] J. Nogami, A. A. Baski and C. F. Quate, *Appl. Phys. Lett.* **58**, 475 (1991).
- [92] H. P. Noh, C. Park, D. Jeon, K. Cho, T. Hashizume, Y. Kuk and T. Sakurai, *J. Vac. Sci. Technol. B* **12**, 2097 (1994).
- [93] J. E. Northrup, M. C. Schabel, C. J. Karlsson and R. I. G. Uhrberg, *Phys. Rev. B* **44**, 13799 (1991); private communication.
- [94] Y. Ohta, *J. Electrochem. Soc.* **126**, 1761 (1979).
- [95] C. Park, R. Z. Bakhtizin, T. Hashizume and T. Sakurai, *Jpn. J. Appl. Phys.* **32**, L528 (1993).
- [96] J. R. Patel and J. A. Golovchenko, *Phys. Rev. Lett.* **50**, 1858 (1983).
- [97] Y. Qian, M. J. Bedzyk, S. Tang, A. J. Freeman and G. E. Franklin, *Phys. Rev. Lett.* **73**, 1521 (1994).
- [98] Y. Qian and M. J. Bedzyk, *J. Vac. Sci. Technol. A* **13**, 1613 (1995).
- [99] Y. Qian, P. F. Lyman, T. L. Lee and M. J. Bedzyk, *Physica B*, in press.
- [100] D. H. Rich, T. Miller, G. E. Franklin and T. C. Chiang, *Phys. Rev. B* **39**, 1438 (1989).
- [101] D. H. Rich, F. M. Leibsle, A. Samsavar, E. S. Hirschorn, T. Miller and T. C. Chiang, *Phys. Rev. B* **39**, 12758 (1989).
- [102] M. Richter, J. C. Woicik, J. Nogami, P. Pianetta, K. E. Miyano, A. A. Baski, T. Kendelewicz, C. E. Bouldin, W. E. Spicer, C. F. Quate and I. Lindau, *Phys. Rev. Lett.* **65**, 3417 (1990).
- [103] N. Roberts and R. J. Needs, *Surf. Sci.* **236**, 112 (1990).
- [104] I. K. Robinson and D. J. Tweet, *Rep. Prog. Phys.* **55**, 599 (1992).
- [105] H. Sakama, K. Murakami, K. Nishikata and A. Kawazu, *Phys. Rev. B* **50**, 14977 (1994).

- [106] T. Sakamoto and H. Kawanami, *Surf. Sci.* **111**, 177 (1981).
- [107] K. Sakamoto, K. Kyoya, K. Miki, H. Matsuhata and T. Sakamoto, *Jpn. J. Appl. Phys.* **32**, L204 (1993).
- [108] S. I. Salem, S. L. Panossian and R. A. Krause, *Atomic Data and Nuclear Data Tables* **14**, 91 (1974).
- [109] R. E. Schlier and H. E. Farnsworth, *J. Chem. Phys.* **30**, 917 (1959).
- [110] W. F. J. Slijkerman, P. M. Zagwijn, J. F. van der Veen, D. J. Gravesteijn and G. F. A. van de Walle, *Surf. Sci.* **262**, 25 (1992).
- [111] B. E. Steel, L. Li, J. L. Stevens and I. S. T. Tsong, *Phys. Rev. B* **47**, 9925 (1993).
- [112] K. Takayanagi, Y. Tanishiro, S. Takahashi and M. Takahashi, *Surf. Sci.* **164**, 367 (1985).
- [113] S. Tang, A. J. Freeman and B. Delley, *Phys. Rev B* **45**, 1776 (1992).
- [114] S. Tang and A. J. Freeman, *Phys. Rev. B* **47**, 1460 (1993).
- [115] S. Tang and A. J. Freeman, *Phys. Rev. B* **48**, 8068 (1993).
- [116] S. Tang and A. J. Freeman, *Phys. Rev. B* **50**, 1701 (1994); private communication.
- [117] S. Tang, A. J. Freeman, Y. Qian, G. E. Franklin and M. J. Bedzyk, *Phys. Rev. B* **51**, 1593 (1995).
- [118] S. Y. Tong and A. L. Maldonado, *Surf. Sci.* **78**, 459 (1978).
- [119] R. M. Tromp, R. G. Smeenk, F. W. Saris and D. J. Chadi, *Surf. Sci.* **133**, 137 (1983).
- [120] R. M. Tromp, R. J. Hamers and J. E. Demuth, *Phys. Rev. Lett.* **55**, 1303 (1985).
- [121] R. I. G. Uhrberg, R. D. Bringans, R. Z. Bachrach and J. E. Northrup, *Phys. Rev. Lett.* **56**, 520 (1986).
- [122] L. E. C. van de Leemput and H. van Kempen, *Rep. Prog. Phys.* **55**, 1165 (1992).
- [123] A. A. van Gorkum, K. Nakagawa and Y. Shiraki, *J. Appl. Phys.* **65**, 2485 (1989).

- [124] M. A. van Hove, W. H. Wienberg and C. M. Chan, *Low-energy Electron Diffraction: Experiment, Theory and Surface Structure Determination*, Springer, West Berlin (1986).
- [125] J. A. Venables, G. D. T. Spiller and M. Hanbucken, *Rep. Prog. Phys.* **47**, 399 (1984).
- [126] H. Wagenfeld, *Phys. Rev.* **144**, 216 (1966).
- [127] R. P. Walker and B. Diviacco, *Rev. Sci. Instrum.* **63**, 392 (1992).
- [128] J. Wang, M. J. Bedzyk, T. L. Penner and M. Caffrey, *Nature* **354**, 377 (1991).
- [129] P. C. Weakliem, G. W. Smith and E. A. Carter, *Surf. Sci.* **232**, L219 (1990).
- [130] R. A. Wolkow, *Phys. Rev. Lett.* **68**, 2638 (1992).
- [131] E. A. Wood, *J. Appl. Phys.* **35**, 1306 (1964).
- [132] D. P. Woodruff and T. A. Delchar, *Modern Techniques of Surface Science*, Cambridge University Press, Cambridge (1986).
- [133] W. S. Yang, F. Jona and P. M. Marcus, *Phys. Rev. B* **28**, 2049 (1983).
- [134] M. T. Yin and M. L. Cohen, *Phys. Rev. B* **24**, 2303 (1981).
- [135] B. D. Yu and A. Oshiyama, *Phys. Rev. B* **50**, 8942 (1994).
- [136] J. Zegenhagen, *Surf. Sci. Rep.* **18**, 199 (1993).